Deciphering the mechanisms of 1D and 2D self-assembly of biopolymers

Jiajun Chen

A dissertation

submitted in partial fulfillment of the

requirements for the degree of

Doctor of Philosophy

University of Washington

2020

Reading Committee:

James J. De Yoreo, Chair

Chunlong Chen

Lucien N. Brush

Program Authorized to Offer Degree:

Materials Science and Engineering

University of Washington

Abstract

Deciphering the mechanisms of 1D and 2D self-assembly of biopolymers

Jiajun Chen

Chair of the Supervisory Committee:
Professor James J. De Yoreo
Department of Materials Science and Engineering

Self-assembled biomolecular architectures have exhibited various properties, including electronic, optical, chemical, and mechanical. Due to their diverse structures and unique functions, hierarchical biomolecular assemblies have found a wide range of potential applications in materials science, biomedical engineering, tissue engineering, or nanotechnology. These appealing properties have intensified interest in understanding their design and structural control, and great advances have been achieved. However, little attention has been given to the mechanism by which they nucleate and grow. Understanding the dominant pathways and parameters determining their pathway selection, as well as the formation kinetics, would enable precise control over phase and morphology during the synthesis of these biomolecular nanostructures.

Here, we first introduce recent studies of biomolecular self-assembly and key factors controlling their assemblies, followed by a brief discussion about the functionalization of these materials and their applications. Then we present our study on a two-dimensional (2D) peptide assembly system. Using a peptide selected for its binding affinity to MoS_2 surfaces, we directly observed nucleation and growth of 2D arrays by molecularly resolved in situ atomic force microscopy (AFM) and compared the results to molecular dynamics (MD) simulations. We find the peptide arrays exhibit an epitaxial relationship to the underlying lattice but assemble one row at a time from dimeric structural units. The nuclei are ordered from the earliest stages and form without a nucleation free energy barrier, a result predicted by classical nucleation theory for one-dimensional (1D) crystals. Moreover, aspect ratios of the arrays can be tuned simply via peptide concentration. We also reveal the effects of peptide sequences and substrates on the assembly pathway. Furthermore, we demonstrate several peptoid designs to mimic the behaviors of the original peptide sequence and seek for potential applications.Based on the developed approaches, the assembly and disassembly of 1D and 2D computationally designed proteins were also investigated. In the case of the helical filament system where protein monomers were designed to assemble into 1D fibers, growth kinetics were carefully studied, and the growth rate was found to have a linear dependency on monomer concentration. Accessory capping units triggered the dissolution of fibers and showed an asymmetric disassembly behavior from two different ends. In the last part, we show the co-assembly of two designed proteins into 2D honeycomb lattices. We studied their edge structures and verified the rate-determining step.

The self-assembling systems studied here share similar features with many other reported self-assembling systems. Our study on their nucleation and growth may provide a guide for interpreting and controlling their assembly and provide new strategies for their future design.

TABLE OF CONTENTS

LIST OF FIGURES

LIST OF TABLES

ACKNOWLEDGEMENTS

I want to express my sincere appreciation to my advisor, Prof. James J. De Yoreo, a tremendous mentor and friend, for his expert guidance and encouragement throughout my study and research. His passion for science, immense knowledge, patience, and inspiring insights have been directing and lighting me during my science journey. I want to thank all the group members and collaborators. It is an incredible experience to work with you all. I also want to thank Prof. François Baneyx, Prof. Peter Pauzauskie, Prof. Lucien Brush, and Prof. Chunlong Chen for serving on my committee and their insightful comments and encouragement. Finally, I would like to thank my family for their support and understanding.

Chapter 1. INTRODUCTION

Molecular self-assembly is a process in which molecular components organize to form ordered structures spontaneously and reversibly as a consequence of local interactions among the components themselves. Such a process has been proven to be a simple but effective way to prepare functional materials across scales with ordered structures and attractive properties [1–3]. Apart from nanoparticle assemblies [4–7] and self-assembled metal-organic frameworks [8–12], biomolecular self-assemblies are also widely used to achieve hierarchically ordered structures. Over the past few years, significant processes have been made in the field of the assembly of biomolecules, including DNAs [13,14], peptides [1,15–17], peptoids [18], proteins [19], viruses [20] and enzymes [21]. Due to the unique properties of these biomolecules, controllable assembled structures, and tunable functions, these self-assembled bionanomaterials have found extensive applications in materials science, biomedical engineering, tissue engineering, biosensing, and nanotechnology [22–29].

In order to achieve these functional bionanomaterials, one of the main challenges is the controllable self-assembly of the building units into desired structures. Previous studies have shown that the assembled structures can be manipulated by carefully controlling internal interactions and external stimulations [1,22,24]. The interactions that drive the assembly of biomolecules are usually non-covalent interactions, including hydrogen bonds [30,31], hydrophobic interactions [32,33], and electrostatic interactions [34,35]. In some cases, weak covalent bonds like di-sulfide bonds can also be utilized to stabilize the assemblies [36]. External stimulations, including temperature, pH, ionic strength or introducing organics and enzymes to the system, also have dramatic influences on controlling the assembled structures [1,24].

These assembled bionanomaterials already possess distinct properties; moreover, they can serve as platforms and can combine with other functional components such as nanoparticles [37–39], carbon nanotubes [40], graphene [41,42], and polymers [43,44], to develop hybrid materials.

In this chapter, we will first introduce and summarize various assembly systems and recent advances in their design and fabrication. Then we will discuss the crucial factors controlling these assembly processes and final architectures, followed by the discussion about the functionalizations of these biomolecular self-assembling materials and their applications.

1.1 Self-assembly of Different Biomolecules

1.1.1 *Self-assembly of DNAs*

Inspired by nature, scientists have long been developing and fabricating artificial nanostructures that can mimic the hierarchical functional materials in biological systems. To achieve this, researchers have investigated a wide range of material systems, including inorganic materials, organic materials, and biomaterials. Among all the remarkable achievements that have been made, the self-assembly of DNA is the most successful one and has huge potentials for building novel functional nanomaterials [13,45]. There are several advantages of using DNA as the building blocks for self-assembling materials [13]. First, the Watson-Crick base pairing is well understood, which makes the hybridization between DNA strands highly predictable. Second, the structure of the DNA double helix has been fully explored, which promotes the computational modeling and the design of complicated DNA nanoarchitectures. Third, DNA-based material possesses suitable structural stiffness and flexibility at the same time, which enables us to create stable motifs with desired morphology. Fourth, with the development of organic chemistry and molecular biology, DNA strands are now relatively easy to synthesize, modify, and replicate. Finally, DNA is biocompatible and can be used for the design of hybrid materials with broad applications.

In 1982, Seeman first envisioned the possibility of combing branched DNA molecules with complementary sticky ends to construct 2D arrays [46]. This proposal is considered to be the very first steppingstone in the development of DNA nanotechnology. In the past decades, a large variety of DNA tiles with different geometries and topologies have been made [13,14,45,47–50].

In Mao et al.'s work, researchers reported parallelogram DNA junctions, which was closely related to Seeman's previous proposal, by covalently linking four Holliday junctions together [51]. These DNA tiles can then self-assemble into ordered 2D arrays with controllable rhombic cavities (Figure 1.1, A and B). These unoccupied cavities could be further modified to host molecular guest covalently or noncovalently. It was also possible to extend the strategy used in their study to construct three-dimensional (3D) arrays. Liu et al. constructed nanotriangles with DNA using a tensegrity strategy (Figure 1.1, C and D) and these different tile structures expanded the availability of DNA in nanofabrication [52]. Their results showed a nonplanar structure with the three DNA components extend in three directions. These three-component duplexes served as the axes of a 3D coordinate system and could be used to guide DNA array growth in discrete directions, thereby enabling assemblies in three dimensions.

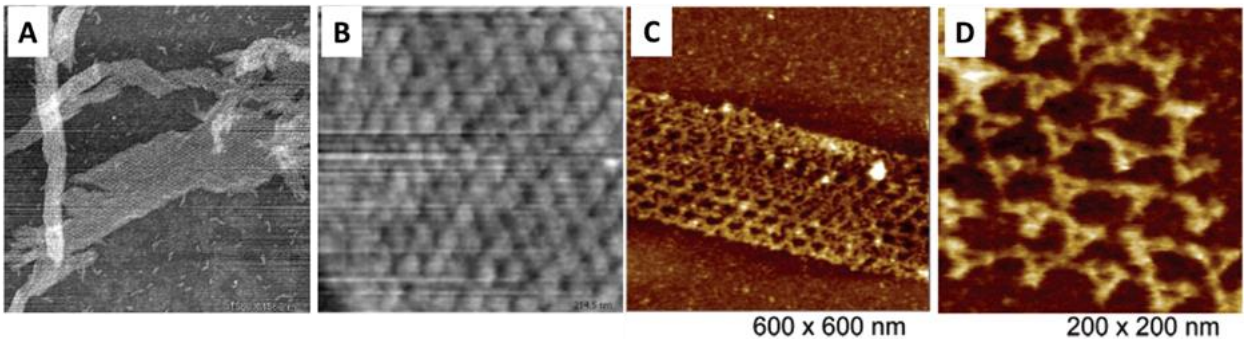

Figure 1.1. AFM images of the assembled DNA arrays. (A) AFM image of dimensions 1568 nm × 1568 nm. (B) High-resolution AFM image showing the rhombus-shaped DNA array. (C and D) AFM images of DNA triangle arrays. Reprinted with permission from [51,52]. Copyright 1999 and 2004, American Chemical Society.

In Yan et al.'s work, a cross-shaped DNA tile was designed and constructed [53]. Programmable self-assembly of 4 × 4 tiles resulted in nanoribbons with uniform-width or two-dimensional nanogrids, which both display periodic square cavities (Figure 1.2 A). Ordered protein arrays were further achieved by assembling streptavidin onto the DNA nanogrids with biotinylated oligonucleotides (Figure 1.2 B). These assembled DNA nanoribbons could also serve as an excellent scaffold for the formation of highly conductive silver nanowires with uniform width.

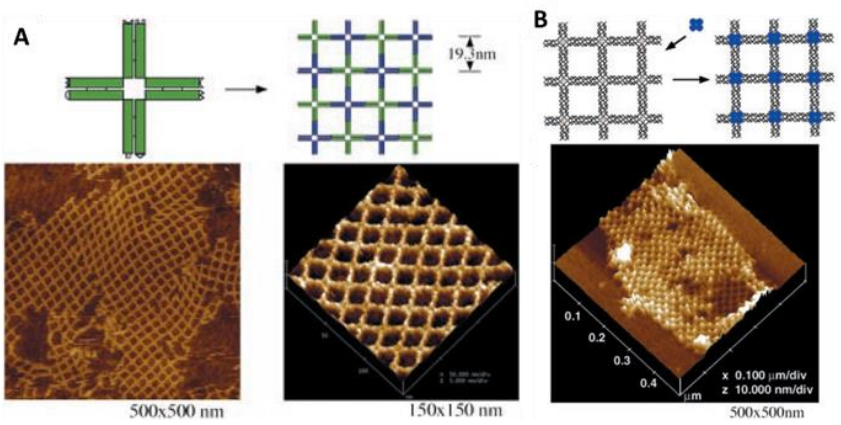

Figure 1.2. AFM Self-assembly of DNA nanogrids using 4 × 4 DNA tiles and the self-assembly of protein arrays templated by 4 × 4 DNA nanogrids. (A) Schematic drawing and AFM images of the self-assembly of 2D nanogrids with corrugated design. The right panel is a surface plot of a magnified region from the left panel. (B) Schematic drawing and AFM images of the DNA nanogrids templated assembly of streptavidin molecules. Reprinted with permission from [53]. Copyright 2003, AAAS.

A significant breakthrough was made in 2006. Rothemund reported a simple method for folding long, single-stranded DNA molecules into arbitrary two-dimensional shapes, which was called "scaffolded DNA origami" [54]. The desired shape was achieved by raster-filling the shape with a 7-kilobase single-stranded scaffold DNA with the help of over 200 short oligonucleotide "staple strands" to hold the scaffold in place. The scaffold strands and staple strands can self-assemble into designed structures in a single-step process, and the outcome structures are around

100 nm in size with desired shapes such as rectangles, five-pointed stars, disks, and triangles (Figure 1.3). The spatial resolution of the structure was 6 nm because each oligonucleotide served as a 6-nm pixel. The nanostructures could be programmed to bear intricate patterns such as words or images on surfaces using this protocol. Such "scaffolded origami" assembly can be a powerful tool to fabricate addressable nanostructures in both two dimensions and three dimensions [55,56].

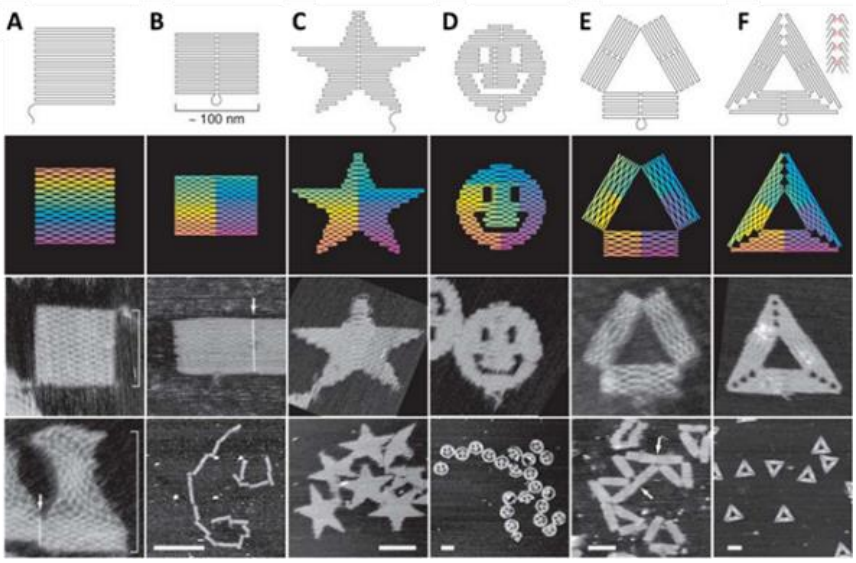

Figure 1.3. Different DNA origami shape designs. All AFM images without scale bars are 165nm × 165 nm. Scale bars for lower AFM images: B, 1 mm; C to F, 100 nm. Reprinted with permission from [54]. Copyright 2006, Springer Nature.

These studies demonstrate the power of DNA as a molecular building block. With specific design, it can be guided to assembled or folded into well-defined nanostructures with tunable parameters. These unique properties enable a wide range of applications, such as molecular electronics, biosensing, determination of molecular structures, and DNA-based computing.

1.1.2 *Self-assembly of Peptides*

Another growing field is peptide self-assembly. Peptides can self-assemble into various kinds of nanostructures, and their assemblies play an essential role in building hierarchically functional

structures with excellent biocompatibility, which may find wide applications in materials science, biomedical engineering, and biotechnology [15,57,58]. In the past decades, great efforts have been made to understand the designs and structural controls of peptide self-assemblies [24,59–61]. The short peptide sequences, compared to proteins, reduce the complexity in their design and synthesis, and simplify the study of the relationship between sequences, secondary structures, and their functionalities.

The amyloid-like structure is an important field in peptide self-assembly. Numerous proteins and peptides have been found to assemble into amyloid fibers under certain conditions [62]. They are associated with numerous diseases including Alzheimer's and Parkinson's diseases [63] and are also found to be related to many biological processes such as hormone storage, signal transduction, and cell surface adhesion [64–66].

These assemblies all share a common cross-β structure, and the self-assembly process is a consequence of backbone hydrogen bonding for the single β-sheet layer formation and side chain interaction (such as hydrophobic interaction and π-π stacking) for combining β-sheet layers together [67]. Besides amyloid fibers, two-dimensional amyloid-based structures have also been reported. In Dai et al.'s study, they proposed a structural model for the nanosheet that was formed by stacking amyloid fiber spines perpendicular to the fiber axis [68]. They further designed several peptide sequences based on their structural model to achieve nanosheets with different functionalities (Figure 1.4). Their study enriches the architectures of amyloid materials and may aid researchers in designing and investigating novel functional amyloid materials.

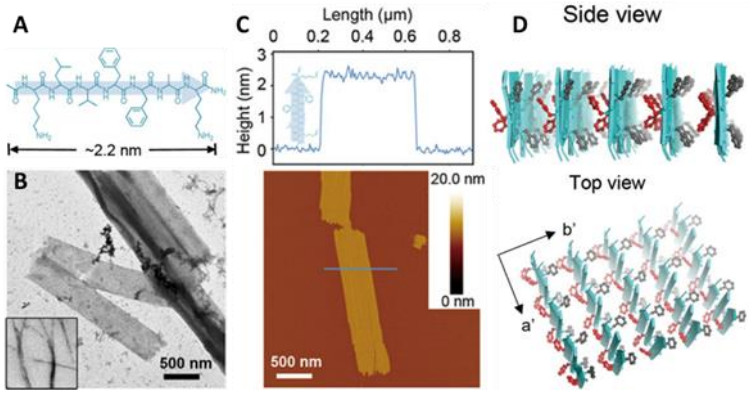

Figure 1.4. Self-assembly of amyloid-forming peptides into nanosheets. (A) Molecular structure of the peptide KLVFFAK. (B) TEM images of the KLVFFAK nanosheets and typical amyloid fibrils of peptide VQIVYK (Inset). (C) AFM image and height profile of the KLVFFAK nanosheet on mica. (D) Structural model of the KLVFFAK nanosheet. Reprinted with permission from [68]. Copyright 2015, National Academy of Sciences.

Another popular assembly system is collagen and collagen-like molecules. Collagens are the most prevalent extracellular matrices and structural proteins in vertebrates. They can assemble into hierarchical structures ranging from molecular scale to macroscopic scale [69]. In Jiang et al.'s work, researchers designed two collagen-mimetic peptide sequences, NSI and NSII, that could self-assemble into 2D nanosheets [70]. These nanosheets consist of collagen triple helices packing in two dimensions, and their assemblies represent a novel morphology for collagen-based materials (Figure 1.5). They further functionalized the nanosheets with gold nanoparticles (Figure 1.5 C) and their results showed that these peptide assemblies could also serve as a platform for creating hybrid nanostructures through noncovalent interactions. In a similar study, Merg et al. reported the structural control over a class of ordered 2D nanosheets assembled from collagen triple helices [71]. Additionally, precise control on the size of the nanosheet was achieved by lengthening the triple helix unit. The internal structure was directly observed by cryo-TEM, and individual triple

helices comprising the lattice could be clearly discerned. These studies provide guidelines for fabricating 2D structures from rigid, helical building blocks and present instructions for controlling their assembly parameters across scales.

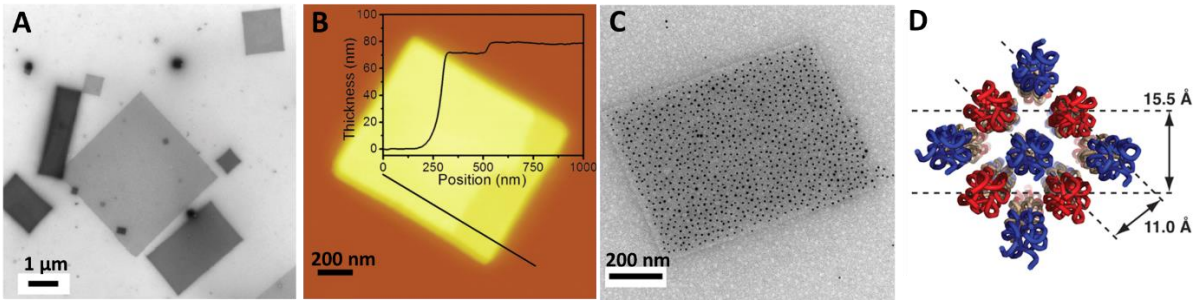

Figure 1.5. Self-assemblies of NSI and NSII nanosheets. (A) TEM image of NSI polydisperse nanosheets. (B) AFM image and height profile of a multilayer NSI nanosheets. (C) TEM image of NSII nanosheet modified with gold nanoparticles. (D) Schematic image showing the structural model of NSI nanosheets with antiparallel triple helices. Reprinted with permission from [70]. Copyright 2014, American Chemical Society.

Other morphologies have also been achieved by using different types of peptide building blocks. Linear peptides often lead to nanofibers, nanoribbons, or nanotubes [72]; cyclic peptides can assemble into nanotubes [73], and branched peptides typically form micelles or vesicles [74].

Besides the assembled structures formed in bulk solution or at the air-water interface, peptides can also self-assemble epitaxially at the solid-liquid interfaces and pattern the substrates [75]. In So et al.'s study, a short sequence with 12 amino acid residues (GrBP5, IMVTESSDYSSY) was selected for its binding affinity to the graphite surface [75]. Interestingly, these peptide molecules not only attached to graphite surface but also assembled into organized patterns with long-range ordering along three equivalent lattice directions, templated by the symmetry of graphite lattice (Figure 1.6). Two distinct phases were observed at the same time, an amorphous (disordered) state and an ordered state. The phase transformation was observed when the surface coverage rate

exceeded ~60%. The influence of aromatic groups on the assembly was also examined through rational mutations at specific sites. The tyrosine residues (Y) were replaced with either tryptophan (W) or phenylalanine (F), two other natural amino acids containing aromatic groups. Tryptophan, containing an extra indole ring, provides a more conformal and stable π- π interaction with graphite lattices, leading to a higher affinity over tyrosine. The mutation M2 containing tryptophan failed to assemble into ordered structures due to the stronger binding to the surface and the reduced mobility on the surface. On the other hand, phenylalanine, lacking an -OH group, has the weakest affinity toward graphite. The M3 mutation with phenylalanine residues also failed to assemble because of the weakened binding strength, and only small clusters were observed on the graphite surfaces.

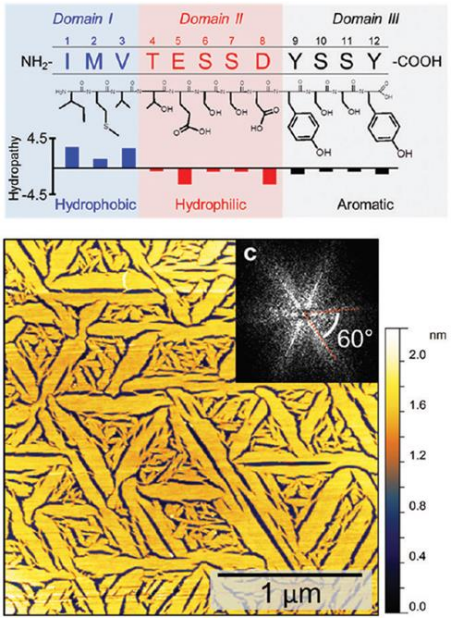

Figure 1.6. Chemical structure of GrBP5 peptide and the self-assembled patterns on graphite surfaces. Reprinted with permission from [75]. Copyright 2012, American Chemical Society.

Computational simulations were also used to understand the interactions between GrBP5 and the graphite surface [76]. It has also been reported that the surface chemistry and the electronic

property can be altered with the surface-directed assembly of these rationally designed peptides [77,78]. These peptides can also self-assemble into similar patterns on transition metal dichalcogenides (TMDCs) surfaces such as molybdenum disulfide (MoS_2), molybdenum diselenide ($MoSe_2$), tungsten disulfide (WS_2), and tungsten diselenide (WSe_2) [78]. Surface patterning with these peptides may introduce novel functionalities to the underlying semiconductor substrates and these hybrid materials may find vast applications in electronic devices, biosensors, or nanotechnology.

1.1.3 *Self-assembly of Proteins*

The self-assembly of proteins has long been the focus of the research community; however, the sophisticated hierarchical structures of proteins raise the complexity and make it challenging to study and understand their self-assembly behaviors. In nature, proteins possess tertiary structures controlled by coiling and folding polypeptide chains into diverse secondary structures. Further folding and interaction of polypeptide chains lead to tertiary and quaternary structures with tremendous diversity in morphology. At the same time, the complex amino acid sequences and folded architectures provide the possibility to construct a wide range of hierarchical assemblies through the precise arrangement of these protein building units. In the past years, numerous studies have been done to better understand the design and formation of protein assembly systems [79]. Moreover, self-assembling proteins have been widely used in exploring novel biological nanomaterials, which may have various potential applications in materials science, biomedical engineering and bio-nanotechnology[79].

Many types of protein assemblies have been synthesized and investigated, such as cages [80,81], capsids [82], vesicles [83], nanorings [84], linear strings [85], nanowires [86,87], nanotubes [88], fibrils [89,90], membranes [91], 2D arrays [36,92], and 3D crystals [93,94].

Inspired by the virus capsids, Bale et al. designed de novo a series of two-component, co-assembling protein nanostructures [81]. These nano-cages contain 120 subunits and have molecular weights (1.8 to 2.8 megadaltons) and dimensions (24 to 40 nanometers in diameter) comparable to those of small viral capsids. Based on electron microscopy, small-angle x-ray scattering, and x-ray crystallography, they proved that ten designs formed assembled structures closely matching the computational design models (Figure 1.7, A and B). The assembly of the two different components into icosahedral complexes is rapid, comparable to those of viral capsids. Moreover, molecular cargoes such as charged GFPs can be loaded into the cages through charge complementarity (Figure 1.7 C). With the precise structural control and the capability to encapsulate a wide range of molecular cargoes including small molecules, nucleic acids, polymers, and other proteins, their attractive designs may find promising future applications in targeted drug delivery, vaccine design, and bioenergy.

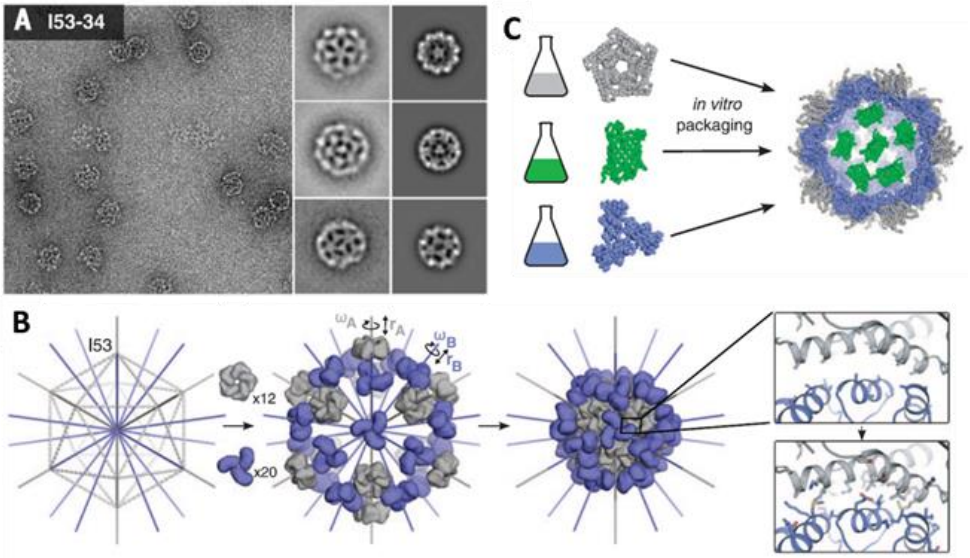

Figure 1.7. De novo design and characterization of protein assembly. (A) TEM images of the assembled cages. (B) Overview of the design method and target architectures. (C) Schematic model for the encapsulation of supercharged GFP in a positively charged I53-50 variant. Reprinted with permission from [81]. Copyright 2016, AAAS.

Zhang et al. reported that Ni^{2+} could trigger the assembly of His-tag-attached C2-symmetric Glutathione transferase (GST) dimers into nanowires [95]. Taking advantage of the metal-coordination interactions and non-covalent protein-protein interactions, Bai et al. achieved accurate control of the orientation of proteins and their self-assembly into protein nanorings (Figure 1.8) [96]. Furthermore, the diameters of the assembled nanorings can be tuned by controlling the ionic strength of the solution.

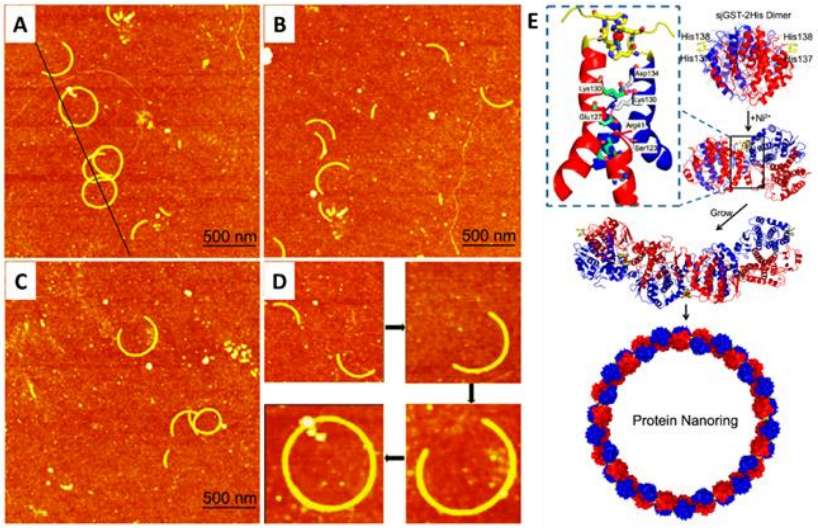

Figure 1.8. Self-assembly of protein nanorings. (A to C) AFM images of protein nanorings formed in pure water with the existence of Ni^{2+}. (D) Different growth stages of nanorings. (E) Schematic model of the assembly of protein nanorings through Ni^{2+}-His interaction. Reprinted with permission from [96]. Copyright 2013, American Chemical Society.

Nanotubes are another common type of 1D structure. In these cases, proteins form ring-like structures in the lateral direction and assemble linearly in the longitudinal direction. The self-assembling tubule-like structures include nanotubes with the stacking of small cylindrical proteins and protofilaments with spirally coiled microtubules. In Yang et al.'s work, highly homogeneous protein microtubes were achieved from tetrameric soybean agglutinin without any chemical or

biological modification [88]. Building units were connected by protein-sugar interactions and π-π interactions. The helical protein microtube consists of three protofilaments, each of which represents an array of soybean agglutinin tetramer linked by the designed ligands.

For 2D protein assembly, Suzuki et al. reported the formation of unsupported 2D protein arrays [36]. Three single- or double-point mutants of RhuA proteins with C4 symmetry were designed to assemble into highly ordered arrays through single-disulfide bonds, double disulfide bonds, or metal-coordination interactions (Figure 1.9). Due to the flexibility of the single-disulfide interactions, the arrays of one of the designs (^{C98}RhuA) were basically defect-free and underwent substantial changes in molecular arrangement, yielding coherently dynamic 2D molecular lattices. Moreover, ^{C98}RhuA lattices exhibited a Poisson's ratio of -1 during the dynamic transformation from an open-gap-state to a close-gap-state, the lowest thermodynamically possible value for an isotropic material, making them auxetic.

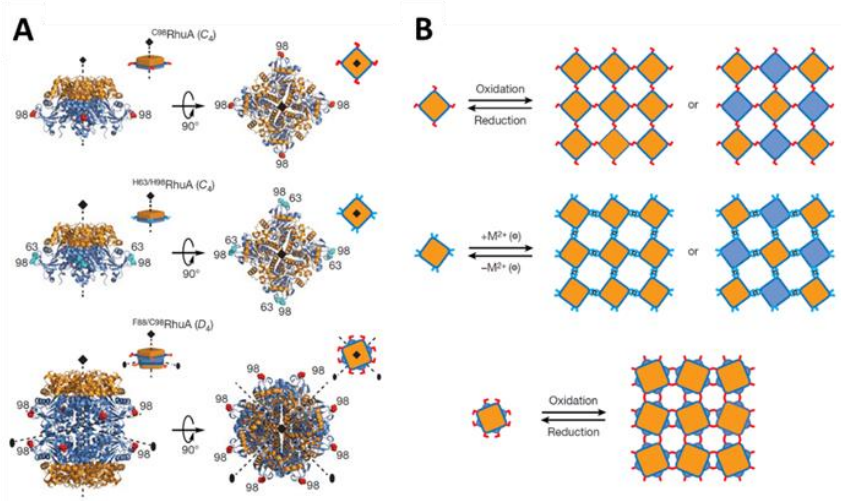

Figure 1.9. Designs of RhuA proteins and their disulfide- and metal-mediated self-assembly. (A) Schematic representations of the ^{C98}RhuA, $^{H63/H98}$RhuA, and $^{F88/C98}$RhuA structures. (B) 2D self-assembled arrays of ^{C98}RhuA, $^{H63/H98}$RhuA and $^{F88/C98}$RhuA. M^{2+} refers to Zn^{2+} or Cu^{2+} ions. Reprinted with permission from [36]. Copyright 2016, Springer Nature.

Besides interface modifications, the computational designed protein-protein interfaces can also be employed in fabricating 0D, 1D, and highly ordered 2D assemblies. Gonen et al. reported a general approach to design 2D protein arrays mediated by noncovalent protein-protein interactions (Figure 1.10) [92]. Protein homo-oligomers were placed into one of the seventeen 2D layer groups, and the degrees of freedom of the array were sampled to identify configurations with shape-complementary interfaces, and the interaction energy was minimized through sequence design calculations. Their results provide new strategies for the design of programmable 2D protein nanostructures with precise structural controls, which will have potential applications in sensing and nanomaterial engineering.

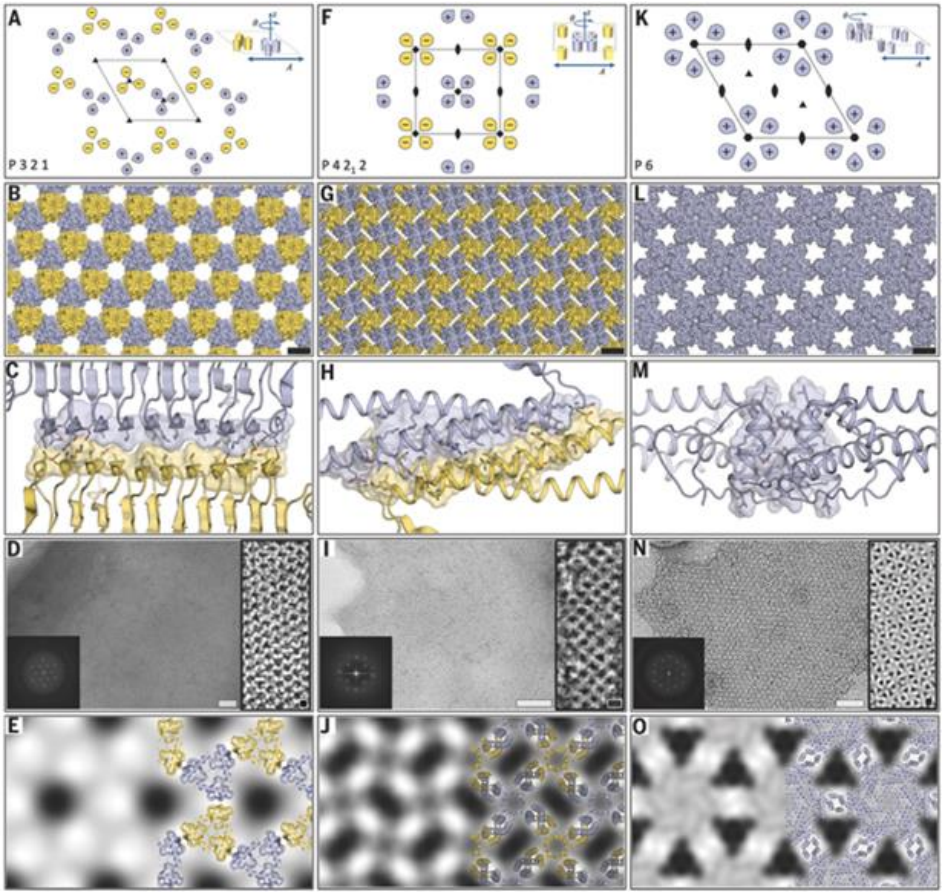

Figure 1.10. Computational design and experimental characterization of designed 2D protein lattices. Reprinted with permission from [92]. Copyright 2015, AAAS.

Although ordered protein assemblies have been achieved, the specificity of protein-protein interactions remains a great challenge. Specific interactions between DNA strands, or between DNA and protein, are usually manipulated by bases or side chains from DNA or protein backbone. However, specificity of protein-protein interactions often come from shape complementarity [97], which is less modular and harder to generalize. In another recent study from Baker's group, Chen et al. reported a strategy to achieve protein-protein interaction specificity through extensive and modular side chain hydrogen-bonding networks [98]. Their capability of designing orthogonal protein heterodimers may enable sophisticated protein-based control logic for synthetic biology and highlights that nature has not fully explored the possibilities of programmable protein interaction modalities.

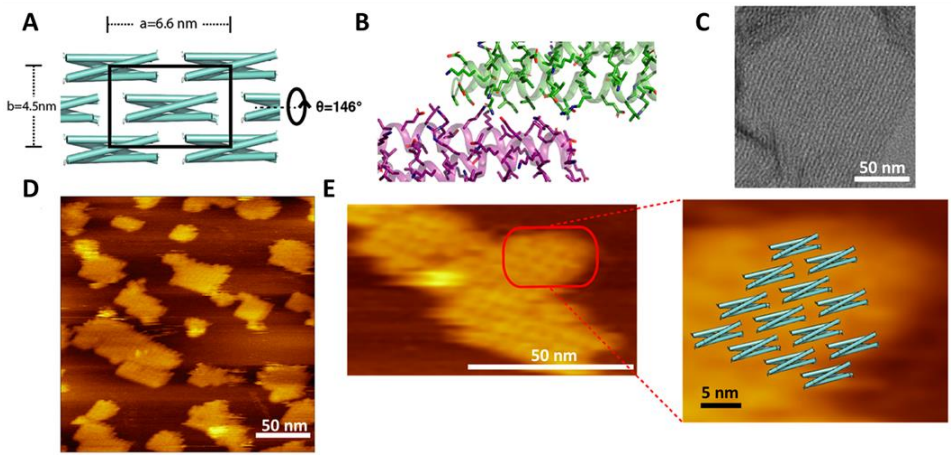

Figure 1.11. Structural characterization of the designed 2D assembled arrays. (A) Lattice design of 2D-HBN. (B) Hydrogen network at the designed interface. (C) Negatively stained TEM image of 2D-HBN assembled arrays. (D) AFM image of 2D-HBN assemblies on mica. (E) High-resolution AFM image showing detailed structures and overlapped on a designed model. Reprinted with permission from [99]. Copyright 2019, American Chemical Society.

Following this strategy, Chen et al. designed pseudosymmetric protein building blocks which can self-assemble into 2D lattices (Figure 1.11) [99]. Their de novo design with pseudosymmetric

building units is an important step toward the fabrication of programmable protein self-assembly with finite shapes, which requires the design of multiple such interfaces on a single pseudosymmetric building block.

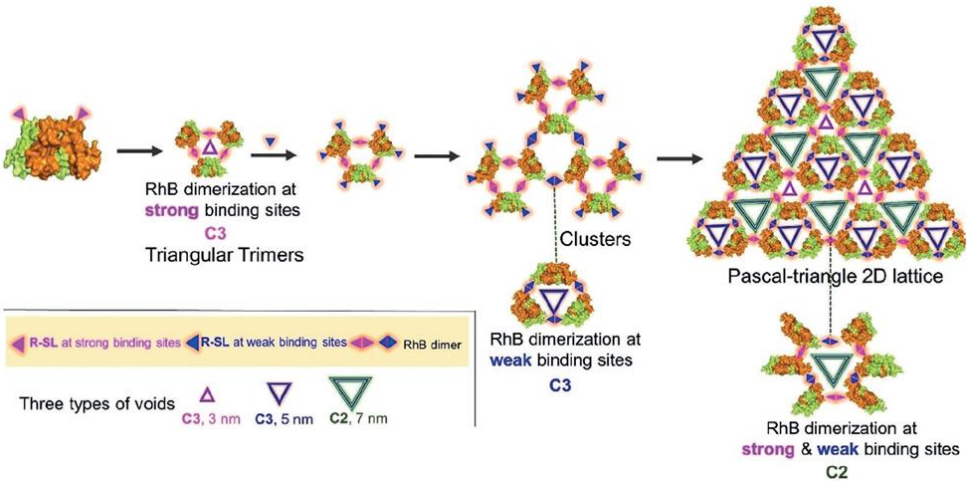

Figure 1.12. Schematic image showing the assembly mechanism of the formation of Pascal-triangle 2D lattice with p3 symmetry. Reprinted with permission from [100]. Copyright 2020, Wiley.

In a recent study, Li et al. reported a more complicated hierarchically self-assembled structure [100]. By introducing ligand (rhodamine B - α2,3-sialyllactose, R-SL) to wheat germ agglutinin (WGA) which is a homodimer with eight independent carbohydrate-binding sites that are concentrated at four locations on monomer interfaces of WGA, Pascal-triangle 2D lattices with 3 sets of triangular voids or 3D crystals were obtained (Figure 1.12). Distinct binding affinities were the key factors to fabricate such sophisticated structure. Interactions between SL groups and different carbohydrate-binding sites linked these ligands and WGA proteins together. The rhodamine B (RhB) dimerization at strong binding sites was responsible for the formation of triangular trimerized building blocks; then the RhB dimerization at weak binding sites tended to enable the assembly of the building blocks into Pascal-triangle 2D lattices. Further increasing the

ratio of ligands introduced more R-SL to the unsaturated carbohydrate-binding sites on WGA, and triggered the interlayer dimerization of RhB, leading to the formation of 3D crystal with analogous protein packing with 2D lattices.

Their study demonstrates the first construction of a Pascal-triangle 2D lattice from native proteins and provides a strategy to fabricate more complicated hierarchical structures, which may give rise to the construction of novel assemblies and provide better understanding of design principles of sophisticated geometries in nature.

1.1.4 *Self-assembly of Peptoids*

Peptoids are biocompatible sequence defined polymers with backbones similar to peptides; however, they exhibit much higher chemical and thermal stabilities than peptides and proteins [101]. Due to the lack of backbone hydrogen bond donors, peptoid-peptoid and peptoid-surface interactions can be simply manipulated through the variation of side chain chemistry during self-assembly processes [102–104]. Moreover, broad side chain diversity enables a wide range of functionalizations of the self-assembling peptoids while maintaining almost unchanged assembly behavior and similar hierarchical structures [102,105,106].

In a recent study, Chen et al. demonstrated the self-assembly of 12-mer peptoids into hexagonally patterned nanoribbons on mica surfaces by carefully controlling the peptoid-peptoid interactions and peptoid-mica interactions [102]. The peptoid was designed to have alternating polar N-(2-carboxyethyl)glycines (Nce) groups and nonpolar N-[2-(4-chlorophenyl)ethyl]glycines (N4-Clpe) groups. Nce groups enable Ca^{2+}-carboxylate interactions and the aromatic N4-Clpe groups build strong intermolecular π-π interactions to stabilize the self-assembled structures.

Inspired by cell membranes, Jin et al. designed and synthesized a series of amphiphilic peptoids, containing a polar domain and an aromatic hydrophilic domain [106]. These lipid-like

peptoids could assemble into highly stable, crystalline, free-standing 2D nanosheets with self-repairing capabilities (Figure 1.13). Combining experimental results and molecular dynamic simulations, they found that these peptoid sheets followed an anisotropic formation process, they grew faster in one direction due to the stronger peptoid-peptoid interactions along that direction [107]. They further demonstrated that such assemblies could be used as a robust platform to incorporate and pattern different functional components.

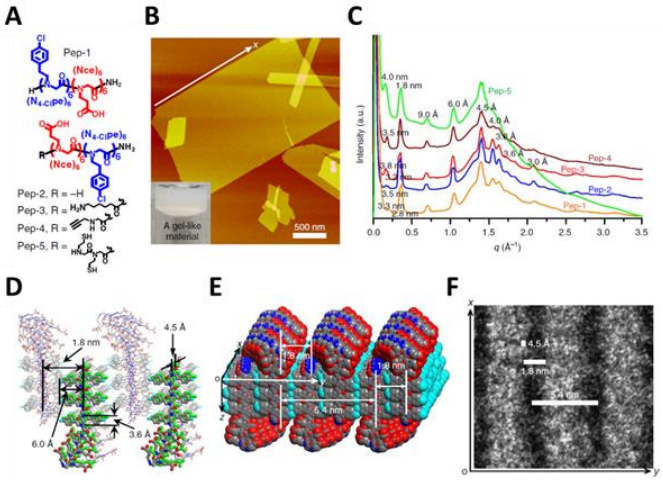

Figure 1.13. Self-assembly of amphiphilic peptoids into highly stable and crystalline 2D nanosheets. (A) Design of peptoids. (B) AFM image of self-assembled Pep-1 membranes. (C) X-ray diffraction data of assembled peptoid nanosheets. (D and E) Molecular model of the assembly. (F) High-resolution TEM image showing well-aligned rows in the membranes. Reprinted with permission from [106]. Copyright 2016, Springer Nature.

Similar peptoid sequences have also been designed to self-assembled into nanotubes and nanofibers [105,108]. In a recent study, the fabrication of highly stable, dynamic, and designable peptoid nanotubes was reported [105]. Researchers also proposed a unique assembly mechanism based on time dependent TEM studies. The assembly process included four steps: amorphous particles, creation of nanoribbons, rolling-up and folding, and the closure to form nanotubes. They

also demonstrated that the diameter and thickness of nanotubes can be tuned by controlling the length of hydrophobic domains.

These peptoid assembling systems discussed above can be sequence-defined and are usually highly stable, biocompatible, and possess protein-like selectivity for molecular recognition [109]. These assembling peptoids may find robust applications in biological imaging, biosensing, drug delivering, and electronics [105].

1.2 Interactions Controlling the Self-assembly of Biomolecules

The driving forces for biomolecular self-assembly are complicated and the assembled nanostructures usually result from a delicate balance between several kinds of non-covalent interactions. In this section, we will discuss some essential intermolecular interactions leading to the self-assembly of biomolecules.

1.2.1 *Hydrogen Bond*

A hydrogen bond is an attraction between a hydrogen (H) atom, which is covalently bound to an electronegative atom, especially the second-row elements such as nitrogen (N), oxygen (O), or fluorine (F), and another electronegative atom with a lone pair of electrons. Hydrogen bonding plays an essential role in many scientific fields, including biochemistry, biomaterials, and organic chemistry. It also plays a crucial role in the assembly and organization of organic compounds and biomolecules.

Here is a straightforward example where we can visualize the hydrogen bonds that lead to the ordered assembly of naphthalene tetracarboxylic diimide (NTCDI, Figure 1.14 A) into 2D arrays on Ag:Si(111) surface [110]. Sweetman et al. used non-contact mode AFM to quantitatively measure the molecular force field and potential energy landscape for hydrogen-bonded molecules.

With a suitably functionalized probe, and carefully operating the scanning in the regime of the tip-sample potential where the repulsive force is dominating, a remarkably high resolution was obtained at a low temperature (Figure 1.14, B and C). Hydrogen bonds (N-H···O) between NTCDI molecules could be directly visualized and the results highlighted the essential role of hydrogen bonding in constructing the arrays of NTCDI molecules.

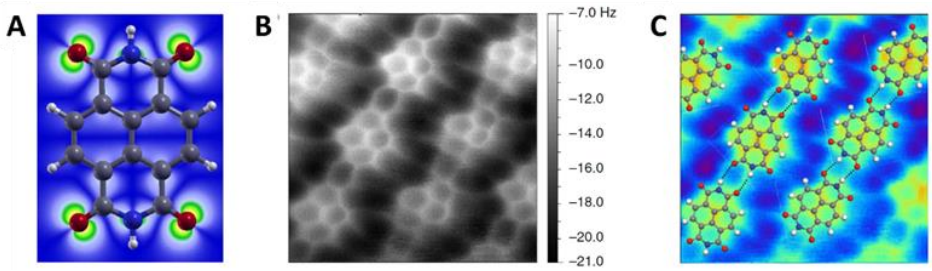

Figure 1.14. Visualization of hydrogen bonding in a 2D assembly system. (A) Molecular structure of NTCDI with a partial charge density isosurface superimposed (Colors: grey-carbon; white-hydrogen; red-oxygen; blue-nitrogen). (B) Constant height AFM image of NTCDI assembly on the Ag:Si(111) surface acquired at 77 K. Image size 2.1 by 2.0 nm (oscillation amplitude, 275 pm). (C) Overlay of the model of NTCDI on an AFM image. The primary intermolecular hydrogen bonds (N-H···O) are shown as black lines. Reprinted with permission from [110]. Copyright 2014, Springer Nature.

In the process of biomolecular self-assembly, hydrogen bonding can sometimes guide the growth of biomolecules in one direction with long-range ordering, leading to the formation of a final one-dimensional assembled structure. Hydrogen bonds between biomolecules and substrates with specific properties can also enhance the formation of functional biomolecular hybrid nanomaterials [1].

Diphenylalanine is a widely studied dipeptide for its self-assembly property in water. In a previous study, Kim et al. have shown that diphenylalanine concentration can tune the ratio of hydrogen bonds between each of the diphenylalanine molecules and water molecules, and further

control the formation of nanowires and nanotubes [111]. Increasing the ionic strength can also weaken the hydrogen bonds between these peptides and water molecules since ions reduce the number of free water molecules around each diphenylalanine molecule. They also showed that sonication and high temperature could break these intermolecular hydrogen bonds while increasing the hydrophobic interactions between diphenylalanine molecules. The strength of the hydrogen bonding would further control the transformation between nanowires and nanotubes [112].

In a similar study, Li et al. reported the fabrication of diphenylalanine microrods by hydrogen-bond-based assembly [31]. Their results demonstrated that 1,1,3,3,6,6-hexafluoro-2-propanol (HFP) could stabilize diphenylalanine molecules in water by forming intermolecular hydrogen bonds with these dipeptides. When the dipeptide/HFP/water solution was dropped onto a silicon wafer, the evaporation of HFP decreased the solubility of diphenylalanine and facilitated the formation of nanofibers, microtubes, and microrods (Figure 1.15). In another study, Li et al. assembled diphenylalanine into nanowires on graphene surfaces [113]. Their results demonstrated that graphene promoted the π-π conjugations between the dipeptides and the substrates, while the intermolecular hydrogen bonding mediated the formation of peptide nanowires on graphene surfaces.

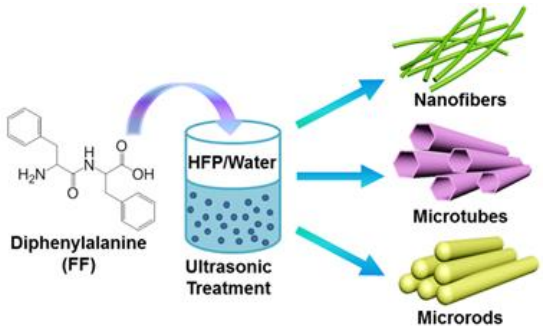

Figure 1.15. Self-Assembly of diphenylalanine into nanofibers, microtubes, and microrods. Reprinted with permission from [31]. Copyright 2015, American Chemical Society.

Besides small peptides, complicated biomolecules, including DNAs, proteins, enzymes, and viruses, can also self-assemble through hydrogen bonding. For example, Lee et al. achieved ultrathin membranes of M13 viruses, which were genetically engineered with selective binding on the edges of graphene-oxide nanosheets [114]. The specific binding affinity for the substrate came from the strong electrostatic interaction and hydrogen bonding. The basic amino acids (histidine and lysine) in the coat protein of the M13 virus enabled the strong electrostatic interactions and hydrogen bonds with the carboxylate groups at the edges of graphene-oxide nanosheets.

In another study, Xue et al. reported the use of surface plasmon resonance for the direct sensing of DNA/graphene-oxide binding and confirmed that hydrogen bonding played an essential role in the interactions between graphene-oxide and single-stranded DNA [115]. Their results enabled the development of a novel biosensor for highly sensitive and selective detection of single-stranded DNA.

In de novo-designed protein systems, optimized hydrogen bonding network can also play an essential role in the design of interfaces and the creation of strong binding affinities, leading to the development of 0D, 1D, 2D, and 3D hierarchically assembled nanostructures [81,92,99,116,117].

1.2.2 *Electrostatic Interaction*

Electrostatic interaction is one of the dominant factors in determining the conformations of biomolecules and is significant in the assembly of peptides, proteins, and peptoids into hierarchical nanostructures. It also plays a key role in the function and stability of these materials [118–120].

Miao et al. reported a simple strategy to construct highly ordered protein nanotubes using electrostatic interactions [119]. Stable protein one (SP1) was used as the building blocks, which was isolated from aspen plants (*Populus tremula*). In aqueous solution, it exhibited a ring-like protein consisting of 12 subunits that were tightly bound to each other through hydrophobic

interactions, forming a double-layered six-member nanoring (Figure 1.16 A). SP1 is an ideal building block due to its unique features: high stability at high-temperature, acid-base imbalance, and resistance to organic solvents. The isoelectric point (pI) of SP1 is about 4.3, which demonstrates that SP1 has negative charges on surface in neutral solution. Thus ethylenediamine (EDA) with two positive charges in neutral solution was chosen to serve as bridges between SP1 protein building blocks and induce the assembly of SP1 nanorings into nanotubes (Figure 1.16, B to E). A similar strategy was also used to construct protein nanotubes using SP1 proteins and positively charged quantum dots or poly(amino amine) dendrimers as linkers [121,122].

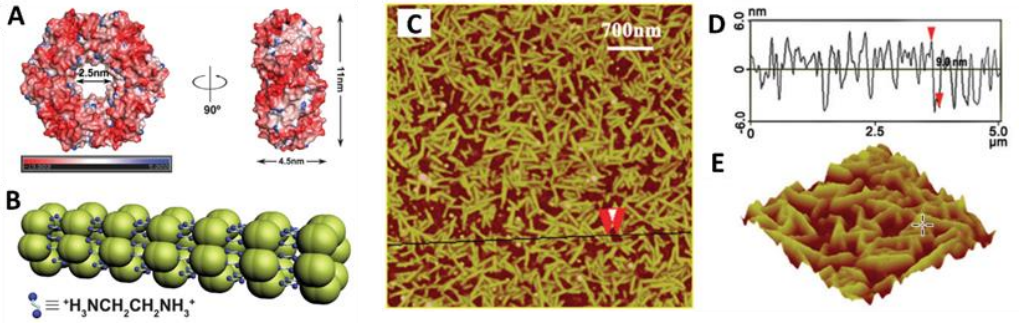

Figure 1.16. Design and AFM images of the EDA induced self-assembly of SP1. (A) Top and side views of the SP1 nanoring with charge distribution on surfaces. The red and blue represent negative charges and positive charges, respectively. (B) Model of the EDA induced self-assembly of SP1 nanorings. (C) AFM image of the EDA induced self-assembly of SP1. (D) Height profile along the line in C. (E) 3D image of a section of C. Reprinted with permission from [119]. Copyright 2016, Royal Society of Chemistry.

In another study, Sun et al. investigated peptide self-assembly using a therapeutic peptide, PTP-7S (EENFLGALFKALSKLL), which was found to self-assemble into nanofibers in solution [120]. Combining experimental results and the coarse-grained (CG) dynamics simulations, they showed that the self-assembly of PTP-7S was a stepwise process that peptide monomers first

clustered into peptide-assembling units (PUs) with charged surfaces, and then the PUs integrated to construct nanofibrils (Figure 1.17). The formation of the hydrophobic core inside the assembling unit, as well as the hydrophilic outer surface, stabilized the aggregated structure, while the electrostatic interaction helped to attract the building units and guided the longitudinal growth of peptide nanofibers.

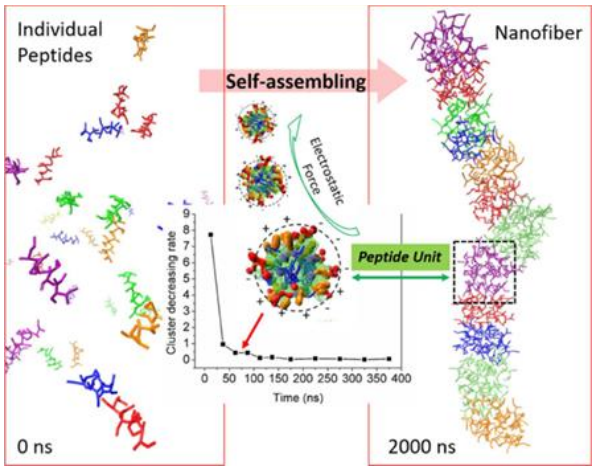

Figure 1.17. Stepwise assembly of PTP-7S (EENFLGALFKALSKLL) into building units and nanofibers through hydrophobic interactions and electrostatic interactions. Reprinted with permission from [120]. Copyright 2017, American Chemical Society.

In Pyles' and Zhang's work, they designed a set of proteins that can specifically bind to muscovite mica surface through electrostatic interactions [117]. The muscovite mica surface was selected because it presents a well-defined K^+ sublattice on the (001) cleavage plane. The proteins were designed to present a flat surface and a regularly repeating backbone with spacing equal to a multiple of the 5.2 Å nearest-neighbor distance between K^+ sites. The binding affinity came from the glutamates on one side of the protein, which lattice-matched to the K^+ ions in the mica lattice. Figure 1.18 shows the designs of the proteins and their alignments along mica lattice. Their study highlighted the importance of electrostatic interaction in surface recognition of these proteins and the further assembly of these protein nanorods into long-range ordered structures.

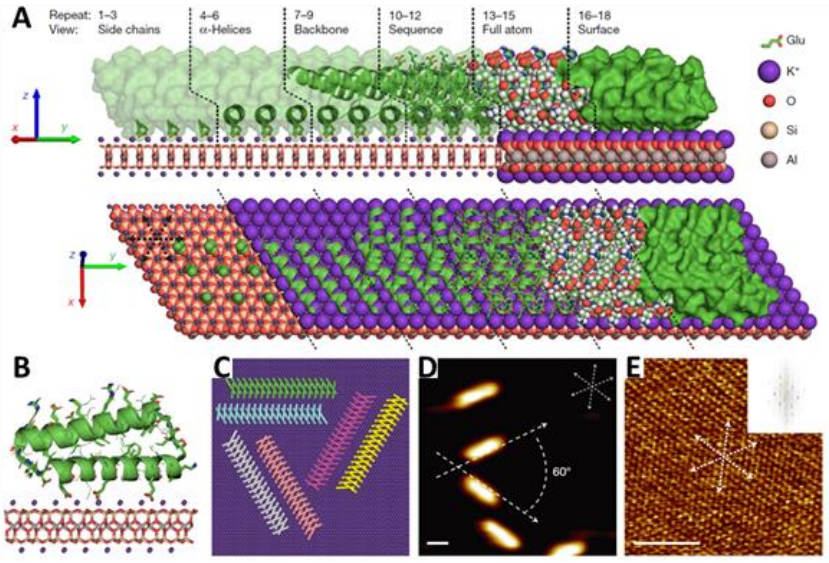

Figure 1.18. Design and characterization of lattice-matched protein monomers. (A) Model of DHR10-mica18 protein lattice-matched to mica (001) surface through the K^+ sublattice. (B) Projection along the y-direction. (C) DHR10-mica18 protein bound to K^+ sublattice in the six symmetry-equivalent orientations predicted by the design model. (D) AFM image of DHR10-mica18 proteins adsorbed on mica surface (anti-parallel orientations look similar). The arrows in the top right corner indicate the orientations of the K^+ sublattice and mica lattice. The scale bar is 5 nm. (E) High-resolution AFM image showing the mica lattice beneath D. The scale bar is 5 nm. Reprinted with permission from [117]. Copyright 2019, Springer Nature.

1.2.3 *Hydrophobic Interaction*

The hydrophobic effect is the tendency of nonpolar substances to aggregate in an aqueous solution and exclude water molecules, which maximizes hydrogen bonding between water molecules and minimizes their surface area in contact with water molecules [123]. The driving force for such effect, hydrophobic interaction, plays an essential role in biological processes, including the formation of cell membrane and vesicle, protein folding, and insertion of membrane proteins into

the lipid bilayer. Such interactions are believed to be inherently entropic effects rather than enthalpic [124–126].

Hydrophobic interactions are also widely applied to construct self-assembled biomolecular structures. In Tsonchev et al.'s work, by combining experimental data and theoretical modeling, researches constructed a phase diagram for the self-assembling biologically active peptide amphiphiles, which could be useful for the design of assembled functional nanomaterials [127]. They found that a dominant hydrogen bonding led to the formation of cylindrical structures, while spherical micelles were found when hydrophobic interaction dominates.

In Liu et al.'s study, a series of peptide nucleic acid amphiphiles (PNAAs) with hybridization properties were designed and synthesized [128]. Driven by hydrophobic interaction, the hybridized PNAAs can form uniform micelles, the base stacking interaction from PNA segments further stabilized the micelles (Figure 1.19). These self-assembled peptide nucleic acid amphiphiles based micelles would find great potential in biomedical applications such as oligonucleotide purification, gene inhibitors, and biosensors.

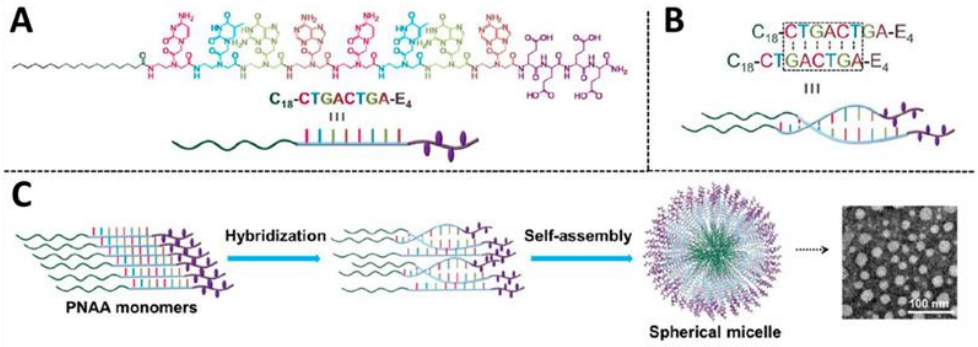

Figure 1.19. Molecular structure of the peptide nucleic acid amphiphile and the assembly process. (A) Structure of C18-CTGACTGA-E4. (B) Formation of PNAA duplex. (C) Self-assembly of PNAAs, exampled with PNAA4. The structures of PNAA duplexes in this figure do not represent its helicity. Reprinted with permission from [128]. Copyright 2014, American Chemical Society.

In a recent study, McGuinness et al. reported the assembly of two-dimensional nanoscale discs driven by hydrophobic interactions [129]. They also showed the co-assembly of these nano-discs and natural fibrous proteins to produce discs-on-a-string nanostructures and revealed that peptide discs facilitated the bundling of protein fibers (Figure 1.20). Their results highlighted the critical role of hydrophobic interactions and provided insight into how synthetic and natural proteins could be combined to develop multi-component, multi-dimensional architectures at the nanoscale.

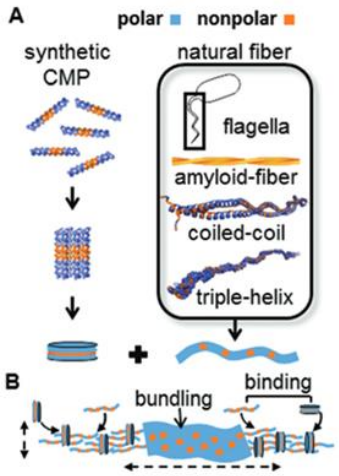

Figure 1.20. Assembly pathway of synthetic peptide discs with natural proteins. (A) Self-assembly of synthetic peptides into discs and natural fibrous proteins. (B) Co-assembly of peptide discs with protein fibers, creating a larger fiber in two dimensions. Reprinted with permission from [129]. Copyright 2017, Royal Society of Chemistry.

In another work done by Lin et al., free-standing nanosheets were achieved via thermodynamically controlled peptide assembly in two dimensions [130]. By taking advantage of self-sorting between peptide β-strands and hydrocarbon chains, they have demonstrated the formation of Janus 2D structures with single-layer thickness, which enable a predetermined surface heterofunctionalization. These nanosheets provide an ideal platform for the engineering of guest components, and enhanced enzyme activity has been observed. The face-selective

functionalization came from the programmed sequences, as well as the distinguished hydrophobic interactions and π-π interactions inside the core of the assembled nanosheet.

1.2.4 *π-π Interaction and Ion-π Interaction*

π interactions are non-covalent interactions that involve π systems. The electron-rich π system can interact with a metal (cationic or neutral), an anion, another molecule or another π system [131]. These interactions are another type of crucial driving force for biomolecular assembly [132]. Amyloid fibril formation is assumed to be the molecular basis for a variety of diseases of unrelated origin. Gazit reported that π interactions might provide energetic contribution as well as ordering and directionality in the assembly process of amyloid structures[133].

In Yu et al.'s work, the co-assembly of peptide amphiphiles and fatty acids was reported [134]. Using nuclear magnetic resonance (NMR), circular dichroism (CD) spectrum, and atomistic simulations, they found that the assembly was primarily driven by anion-π interactions. They also functionalized the peptides with perfluorinated phenylalanine residues to promote the anion-π interactions between peptides and the carboxylate groups in fatty acids. They also showed that positioning of the aromatic units played an important role. As the aromatic units were moved along the peptide backbone away from the hydrophobic part, the interactions with dodecanoic acid transformed the assembled cylindrical structures into ribbon-like structures. Their findings revealed how co-assembly involving specifically designed interaction could drastically control the outcome morphology during the assembly process.

In a recent study, Zhang et al. reported the self-assembly of dipeptides consisting of one fluorinated phenylalanine residue and one natural aromatic residue into laminated nanofibers predominately driven by polar-π interactions [135]. They found that the face-centered stacking patterns of the dipeptide assemblies were stabilized by polar-π interactions, and the antiparallel β-

sheet hydrogen bonding led to the lamination of nanofibers and the formation of ribbonlike structures.

π-π interaction also plays an essential role in the epitaxial assembly of solid binding peptides onto target surfaces. As discussed in section 1.1.2, π-π interactions between aromatic side chains of GrBP5 peptide and graphite lattice contribute to the strong binding affinity of this peptide to the graphite surface [75]. The strength of such interaction will further influence the mobility of peptides on the substrate, as well as the assembly of peptides into ordered patterns.

π-π interaction is also one of the main interactions to manipulate the assembly of peptoids [102,103,106,107], as detailed in section 1.1.4. Because of these robust intermolecular π-π interactions that stabilize these assembled structures, such peptoid assembling systems also show exceptional side chain tolerance, which enable the modification of surface chemistry with a wide range of functional groups and the co-assembly of diverse peptoid building blocks while maintaining similar assembled architectures.

1.3 External Stimulations Towards the Assembly of Biomolecules

Biomolecular self-assembly is highly sensitive to the solution environment, including pH, temperature, and ionic strength. In this section, we will discuss the influence of these external factors on the assembly of biomolecules.

1.3.1 *Influence of pH*

The development of biomolecular nanostructures sometimes strongly depends on the pH condition of the solution [136–138]. For example, Ghosh et al. developed a set of self-assembling peptide amphiphiles that could transform from monomers or spherical micelles into nanofibers when the pH was slightly dropped from 7.4 to 6.6 [139]. A phase diagram for these assembly systems was

also generated after systematically studying the influence of peptide concentration and pH. In a similar work, Chen et al. reported a pH-responsive assembling system that could control the peptide amphiphiles assemble into micelles, nanofibers, or nanofiber bundles [140]. The transformation process came from the electrostatic attraction through oppositely charged amino acid pairs.

In a recent study from Baker's group, Boyken et al. presented a general approach to design pH-responsive protein conformational changes by precisely arranging histidine residues in buried hydrogen bonding networks [141]. They designed homotrimers and heterodimers that were stable above pH 6.5 but underwent dramatic conformational changes when the pH dropped, and electrostatic and steric repulsion built up when histidine residues in the hydrogen bonding networks became protonated (Figure 1.21). The transition pH can also be tuned by the number of histidine-containing networks and the strength of local hydrophobic interactions. This strategy may be used to design novel proteins that can assemble into 1D, 2D or 3D nanostructure with precise structural control. These reversible and rapid pH-responsive structural transformation can find massive applications in targeted drug delivery and biological nanotechnology.

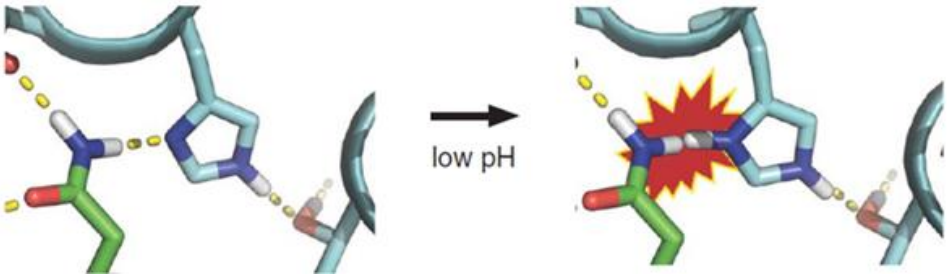

Figure 1.21. Design of pH-responsive proteins. Preorganized histidine residues destabilize intermolecular interfaces upon protonation at low pH. Reprinted with permission from [141]. Copyright 2019, AAAS.

1.3.2 *Influence of Temperature*

Temperature is another important factor that can affect the kinetics or the assembled structures during the biomolecular assembly processes. It can alter the conformation of building units and intermolecular interactions.

In a previous study, Hamley et al. demonstrate a reversible thermal transition process in peptide amphiphile self-assembly [142]. A designed peptide amphiphile C16-KKFFVLK can assemble into nanotubes and helical ribbons in aqueous solution at room temperature (Figure 1.22, A and B). Upon heating, these nanotubes and ribbons undergo a remarkable unwinding transition and form twisted tapes (Figure 1.22 C). This process is reversible, and nanotubes and ribbons dominate again after cooling (Figure 1.22).

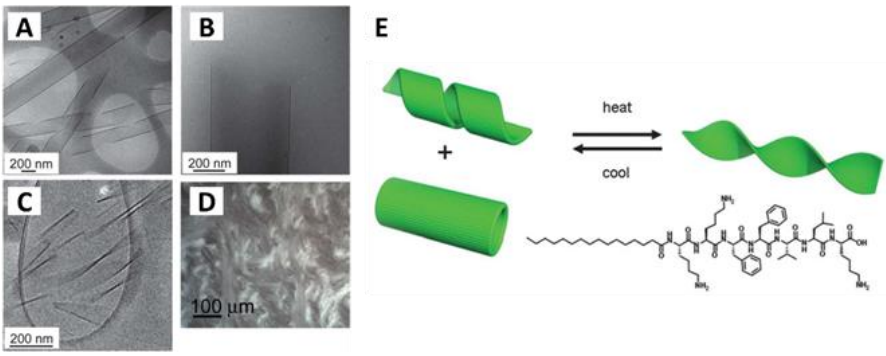

Figure 1.22. Cryo-TEM images showing the self-assembly structures of peptide amphiphiles. (A) Single wall nanotubes coexist with helical ribbons at 22°C. (B) Single wall nanotube at 22°C. (C) Twisted nanotapes at 55°C. (D) Polarized optical micrograph showing the birefringence texture. (E) Schematic model showing the thermo-reversible transformation process. Reprinted with permission from [142]. Copyright 2013, Royal Society of Chemistry.

In Jorgenson et al.'s work, they demonstrated the directed assembly of genetically selected graphite binding peptides on graphite surfaces [143]. They revealed that incubation temperature had a significant effect on the assembled structure due to the tuning of solvated peptide

conformational states. For GrBP5-WT peptides with structurally uniform conformations in solution, they self-assembled into ordered structures readily. Increasing the incubation temperature (thermal energy) elevated the dispersity of the peptide conformations in solution, which negatively impacted the adsorption and assembly process, leading to the increase of amorphous clusters on the surfaces (Figure 1.23). In a follow-up work combining AFM studies and molecular dynamics simulations, Jorgenson et al. reported that the peptide-graphite and peptide-peptide interactions strongly depended on the thermally selected conformations of peptides and that the conformational changes directly led to the different assembled structures observed on graphite surfaces [144].

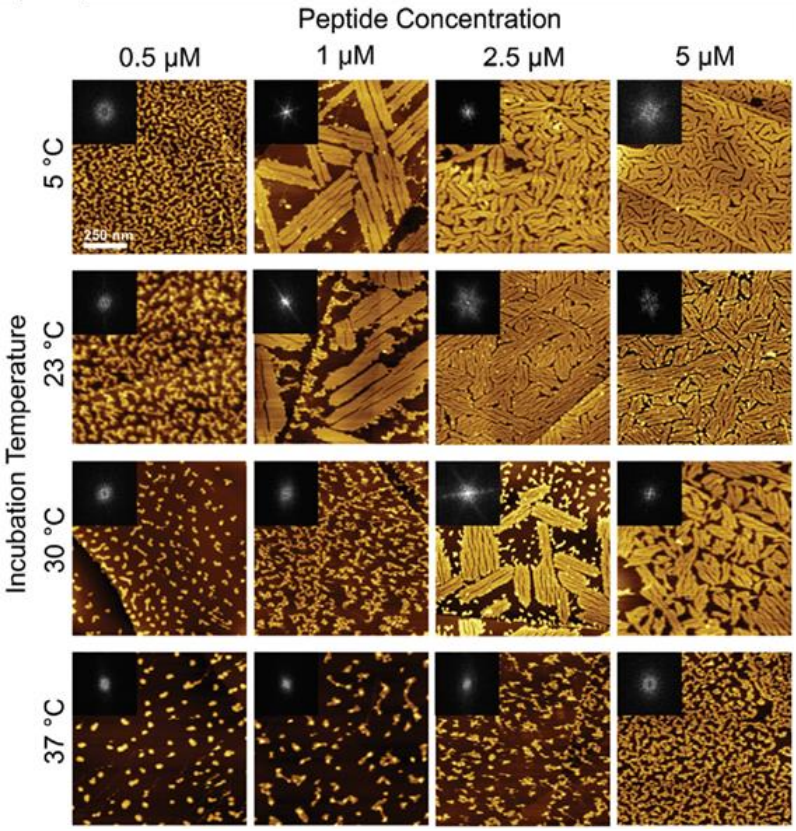

Figure 1.23. GrBP5-WT isothermal self-assembly. AFM images of GrBP5-WT peptides assembled structure at different incubation temperatures and concentrations. All images are 1 μm by 1 μm, and insets are FFTs of the images. Reprinted with permission from [143]. Copyright 2019, Royal Society of Chemistry.

1.3.3 *Influence of Ionic Strength*

Besides the effects of pH and temperature, the influence of ions or ionic strength on the self-assembly processes of proteins [117,145,146], peptides [68], DNAs [147], and RNAs [148] have also been reported.

In Pyles and Zhang's study, protein nanorods were designed to attach to mica (001) surface along lattice direction [117]. They further found out that increasing ionic strength increased the density of protein molecules on the surface. Moreover, a high salt concentration triggered the transformation of assembled patterns from the isotropic phase to the smectic phase with long-range ordering (Figure 1.24). Presumably, the increase of ionic strength contributed to the screening of repulsive electrostatic interactions between protein nanorods, leading to the formation of dense packing and long-range ordering.

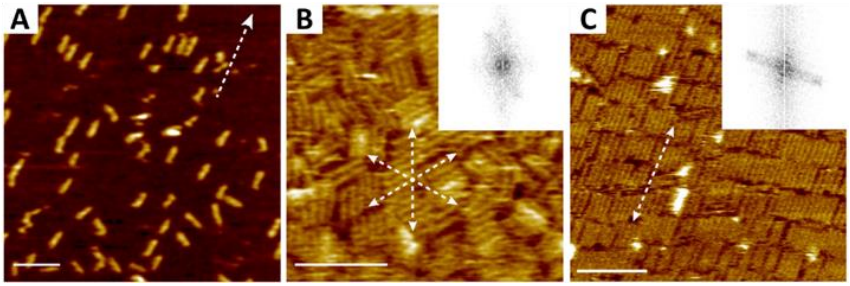

Figure 1.24. Assembly of DHR10-mica18 protein molecules on mica (001). (A to C) AFM images of DHR10-mica18 assembly on mica at 10 mM, 100 mM, and 3 M KCl, respectively. Fast Fourier transforms are shown in the insets of B and C. Increasing KCl concentration leads the protein adsorption from individual monomers to a 2D liquid-crystal-like phase with long-range ordering. Scale bar: 50 nm. Reprinted with permission from [117]. Copyright 2019, Springer Nature.

Semerdzhiev et al. reported the self-assembly of nanometer-sized α-synuclein amyloid fibrils into well-defined micrometer-sized suprafibrillar aggregates with sheet-like or cylindrical morphology depending on the ionic strength of the solution [146]. The formation of suprafibrillar

structures was induced by monovalent and divalent counterions. They also demonstrated that the self-assembly process was controlled by long-range electrostatic repulsion and short-range attraction. With the increase of ionic strength, the electrostatic interactions between fibrils were screened, leading to the formation of sheet-like structures.

In another study, Dai et al. investigated the formation of nanosheets with amyloid-forming peptides [68]. Their results showed that the assembled structures could be tuned by changing the ionic strength of the solution. Increasing NaCl concentration facilitated the formation of peptide nanosheets, leading to larger nanosheet sizes and higher yield. They also indicated that high salt concentration could screen out the repulsive force between the two lysine residues in the sequence, assisting the assembly of peptide molecules.

Besides interaction between biomolecules, ionic strength can also alter the affinity between the biomolecule and the substrate. In Liu et al.'s study, DNA tiles were shown to assemble into ordered arrays on mica surfaces with the existence of Ni^{2+} ions [147]. Ni^{2+} ions served as bridges between DNA tiles and mica. At a low Ni^{2+} concentration, DNA tiles did not have enough binding strength to the surface, while a high Ni^{2+} concentration trapped the DNA tiles on the surface with a strong attraction, prohibiting their ordered assembly. They further showed that 2D arrays with different geometries could be obtained by fine-tuning the Ni^{2+} concentration (Figure 1.25).

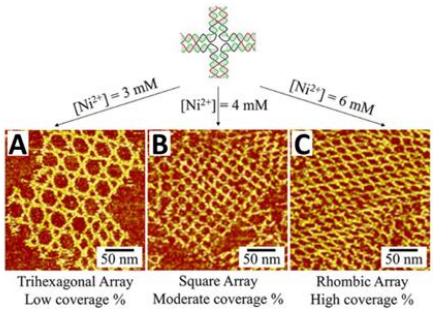

Figure 1.25. Different 2D arrays assembled under different Ni^{2+} concentrations. Reprinted with permission from [147]. Copyright 2017, Wiley.

The morphology of biomolecular assembly on surfaces can also result from the competition between molecule-molecule and molecule-substrate interactions. For example, the morphology of collagen assembly on mica surfaces depends on the balance between collagen-collagen interactions and collagen-mica interactions [35,149]. K^+ ions can bind to the negatively charged mica substrate and neutralize it, which reduce the binding affinity of collagen molecule and promote surface diffusion. As a result, increasing K^+ concentration will decrease the coverage density of collagens on mica, leading to the formation of bundles of collagen fibrils due to the increased collagen-collagen interactions and decreased collagen-mica interactions.

1.3.4 *Influence of Substrate*

Previous studies have shown that substrates have significant effects on the self-assembly processes [22]. Interactions between surfaces and self-assembling building units may facilitate or inhibit the assembly processes, and the lattice symmetries of surfaces can usually guide the packing of these assembling units, leading to epitaxially assembled structures.

In a previous study by Kowalewski et al., Alzheimer's β-amyloid (Aβ) peptide was studies on different surfaces using in situ AFM [150]. Only randomly attached nanoparticulate aggregates of Aβ was found on hydrophilic mica surfaces, while on hydrophobic highly oriented pyrolytic graphite (HOPG) surfaces, Aβ formed directional, elongated, narrow structures. Their study highlighted the importance of hydrophobic interactions between Aβ peptides and graphite surfaces in tuning the assembly behaviors.

In a similar study, Zhang et al. studied the assembly of GAV-9 peptide on both mica and HOPG [32]. Their results showed that such peptide assembled into directional patterns following the symmetry of the substrate (Figure 1.26). On mica surfaces, GAV-9 was oriented upright on mica surfaces with the peptide backbone perpendicular to the substrate. In this case, the

electrostatic interaction between the negatively charged mica surface and the positively charged peptide terminal drove the ordered assembly of GAV-9. However, on graphite surfaces, GAV-9 adopted a flat-lying conformation with their hydrophobic side chains in contact with the graphite surface. Although the final structures may look similar, their results point out that interfacial properties may dramatically affect the self-assembly process.

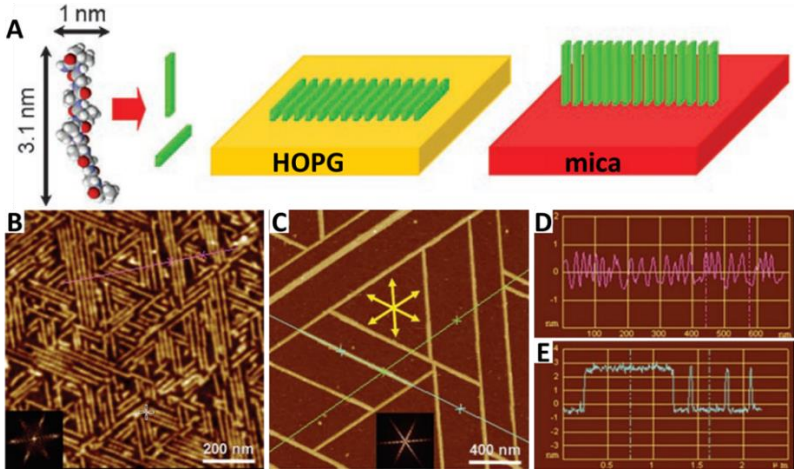

Figure 1.26. Assembly behaviors of GAV-9 peptide on mica and HOPG. (A) Schematic image showing the assembly mechanisms of GAV-9 on HOPG and mica respectively. (B) AFM image showing the assembly on HOPG. (C) AFM image showing the assembly on mica. (D and E) Height profile for B and C respectively, indicating that GAV-9 adopted a flay-lying structure on HOPG while exhibiting an upright conformation on mica. Reprinted with permission from [32]. Copyright 2006, Wiley.

Moreover, slightly different substrates may also lead to huge differences during the self-assembly process. In Leow et al.'s study, researchers followed the assembly of collagen on muscovite mica and phlogopite mica surfaces respectively [149]. On muscovite surfaces, collagens assembled into unidirectionally aligned layer with the D-periodic band. However, on phlogopite surfaces, whose lattice structure is slightly different from muscovite, collagens formed into a novel triangular network where individual fibrils possessed D-periods. Similar self-assembly behavior

was also reported in a recent study by Pyles et al., where de novo designed protein nanorods found a preferred orientation on muscovite surfaces while distributing equivalently along three directions on phlogopite surfaces [117].

1.4 Property and Functionalization of Biomolecular Self-assembly

Self-assembled biomolecular nanomaterials have shown a wide range of potential applications in biomedical and biotechnological fields [22,24,79]. For example, recent studies have revealed that self-assembled peptides can have significant antimicrobial activity[151–153]. Biomolecular assembled materials can also serve as smart delivery platforms. Cargoes such as drugs, proteins, DNAs, RNAs can be loaded and transported in assembled peptide nanostructures [154–156]. For electronics, self-assembled biomaterials can also be a promising alternative for traditional inorganic semiconductors. Some peptide-based materials, especially the phenylalanine-based and tryptophan-based aromatic dipeptide assemblies, exhibit semiconductivity via π-π interactions [132]. The highly ordered and directional intermolecular π-π interactions and hydrogen-bonding networks contribute to the creation of quantum confined structures within the assemblies, decreasing the band gaps of the assembled structures into semiconductor regions [132]. Their electronic properties can also be tuned by the structural diversity and various functionalization of the assembled structures. The development of biomolecule-based semiconductors may fill the gap between inorganic semiconductors and biological applications.

Moreover, biomolecules that bind to 2D electronic material surfaces can alter their conducting properties [17]. Previous studies have revealed that the electronic property of graphene is sensitive to molecular doping and surface binding events [157,158]. The resulting changes in charge transfer and resistance create output signals that enable the specific detection of the surface binding of molecules. In Khatayevich et al.'s study, they demonstrated the selective detection of streptavidin

proteins against a background of serum proteins through the functionalization of graphene sensors with graphite binding peptide assemblies [159]. Their results showed the possibilities to develop various electronic, photonic, and magnetic-based biosensors using appropriately designed and selected solid binding peptides.

Besides the inherent properties, these assembled structures can be further modified with other functional components, including nanoparticles, inorganics, carbon materials, and biomolecules [22]. In Lin et al.'s work, DNA tiles decorated with signaling aptamers were directed to self-assemble into high-density nanoarrays for the detection of protein molecules [160]. The high local density of the signaling component displayed on the DNA nanogrids provides the possibility to detect low concentrations of the target proteins.

In Du et al.'s study, the previously designed ^{C98}RhuA protein arrays [36] were modified to direct the precise assembly of Au nanoparticles into ordered and diverse nanoarchitectures (Figure 1.27) [39]. Their insights about the assembly mechanism may benefit the future development of electronic, plasmonic, and magnetic devices with hierarchically hybrid nanomaterials.

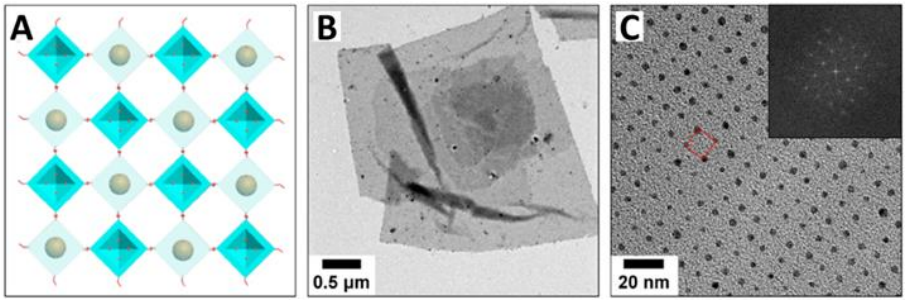

Figure 1.27. Arrangement of Au nanoparticles directed by the ordered assembly of $^{C4/C98}$RhuA proteins. (A) Scheme of the self-assembly of 2D monolayer Au nanoparticles templated by $^{C4/C98}$RhuA array. (B) TEM image of the co-assembled nanosheets, (C) high magnification TEM image showing the well-ordered Au nanoparticles. Reprinted with permission from [39]. Copyright 2020, American Chemical Society.

In Charrier et al.'s work, researchers engineered the paracrystalline surface-layer protein molecules of *Caulobacter crescentus* to display SpyTag peptides that form irreversible isopeptide bonds to SpyCatcher-modified proteins, nanocrystals, and biopolymers on the extracellular surface [161]. Their result proves that 2D protein array can serve as a platform for self-organization of soft and hard nanomaterials on cell surfaces with precise control, which is an essential approach toward building hierarchically ordered living materials with desired properties.

The unique properties of the self-assembled biomolecular materials, combined with diverse functionalizations using nanoparticles, carbon materials, inorganic scaffolds, and biomolecules, have greatly improved and expanded the application of these materials in biosensing, biomimetic mineralization, drug and gene delivery, bioimaging, biotherapy, and bioelectronics.

1.5 SUMMARY AND OUTLOOKS

In this chapter, we summarized recent approaches in the design and formation of biomolecular self-assembly systems including DNAs, peptides, proteins, and peptoids. Various structures can be obtained by carefully controlling the biomolecule-biomolecule interactions and biomolecule-material interactions. The effects of external factors such as pH, temperature, ionic strength, and substrate were also discussed. Moreover, due to the unique structures and functions of these biomolecular assembled materials, as well as diverse functionalization methods, these materials can have promising applications in a wide range of areas. Significant progress has been achieved in the past decades; however, some aspects are attractive but not fully understood and need to be further explored. Firstly, novel strategies and techniques to fabricate and characterize these assembled materials should be developed. Secondly, to address the limits of experimental methods, computational simulations should be improved to better understand the conformations of the biomolecules within the assembled structures, as well as their intermolecular interactions. Thirdly,

more effort should be focused on understanding assembly pathways and mechanisms for biomolecules. Fourthly, new biomolecular motifs with desired properties should be explored. Last but not least, it is also attractive to explore stimuli-responsive assembly systems to achieve, for example, targeted delivery and cancer therapy using pH, thermal, magnetic, electric, and light stimulations.

Chapter 2. SELF-ASSEMBLY OF PEPTIDES ON MoS_2

2.1 INTRODUCTION

Advances in nanotechnology, progresses in biotechnology, and insights in directed assembly have shown that novel and complex composite materials with designed structures and properties can be achieved in multiple dimensions. In the case of 2D systems, self-assembly of 2D molecular arrays on surfaces has been extensively investigated to understand the atomic-scale structural relationships between the substrate and overlying film [162–167]. The results reveal a rich world of frameworks [162,163,167], tilings [162,168], and chiral architectures [162,169] that depend on structural details of both the molecules and the underlying lattice. Recent recognition of the unique electronic [170], optical [170], chemical [163–165] and mechanical [36] properties of 2D materials has intensified interest in their formation and design, yet little attention has been given to the mechanism by which they nucleate. In particular, whether assembly is described by concepts of classical nucleation theory (CNT) in which clusters form stable, ordered structures one growth unit at a time [171], or falls within the broader context of so-called "non-classical" pathways, characterized by formation, transformation and aggregation of transient precursors [172], remains unknown. Understanding the dominant pathways and parameters determining their pathway selection, as well as the formation kinetics, would enable precise control over phase and morphology during synthesis of 2D materials. Using peptides chosen by genetic selection and amplification [173,174] for their binding affinity to MoS_2 (0001) surface, we directly observed nucleation and growth of 2D arrays by molecularly resolved in situ atomic force microscopy and compared the results to molecular dynamics simulations [175]. We find the peptide arrays exhibit an epitaxial relationship to the underlying lattice but assemble one row at a time from dimeric structural units. The nuclei are ordered from the earliest stages and form without a free energy

barrier, a result predicted by CNT for one-dimensional growth. Moreover, because creation of the first row exhibits an order of reaction different from all subsequent rows, aspect ratios of the arrays can be tuned simply via peptide concentration. The results verify long-standing but unproven predictions about nucleation of one-dimensional structures in CNT while revealing key interactions responsible for ordered assembly.

2.2 METHODS

2.2.1 *Peptide Selection and Synthesis*

Peptide selection was carried out using the Ph.D.-7 Phage Display Peptide Library Kit from New England Biolabs as described previously [176]. Bulk molybdenum disulfide was used as the substrate. Scotch tape was used to tear off both sides of the molybdenum disulfide to expose new surfaces. Then the molybdenum disulfide was washed by dipping into acetone and ethanol for several times. For each round of biopanning in the peptide selection cycle, we used a fresh target substrate. Before each round, the target was sterilized in 99% ethanol for 30 min with gentle rocking, followed by washing five times with sterilized water and Tris-buffered saline (TBS). The biopanning steps were carried out according to the protocol from the New England Biolabs Ph.D.-7 manual. The library was exposed to the targets in TBS containing 0.1% TWEEN-20, to reduce phage-phage interactions on the surface. After rocking for 1 h at room temperature, the surfaces were washed with 10 exposures to TBS containing 0.1% TWEEN-20, pH 7.5, and increased TWEEN-20 concentrations to 0.3% and 0.5% for the following two rounds. The phage bound on the target surface was eluted from the surface by adding glycine-HCl (pH 2.2) and rocking gently for 8 min, then transferred to a fresh tube and neutralized with Tris-HCl (pH 9.1). We then amplified the phage eluate after selection by infecting Escherichia coli ER2738 in 25 mL of lysogeny broth (LB), which was then allowed to grow for 4.5 h in an incubating shaker. The

resulting phage were then purified and used for the next round of biopanning. The phage eluate at the third round of biopanning was plated on LB XGal/IPTG plates. Ten blue plaques were then picked from the plate and used for sequencing. Peptides of the selected sequence were synthesized using a CS 336X solid-state peptide synthesizer (C S Bio) with N-terminal acylation and C-terminal amidation, characterized using a Waters Micromass LCT Premier Mass Spectrometer with Water ACQUITY UPLC with Autosampler (LC/MS) and purified by using a Beckman-Coulter Gold high-performance liquid chromatography (HPLC).

2.2.2 *Circular Dichroism Spectrum*

The circular dichroism spectrum of MoSBP1(20 μM) was collected on a JASCO-715 Circular Dichroism Spectropolarimeter at room temperature. High tension (HT) voltage was kept below 600 V to guarantee that the detector was not saturated.

2.2.3 *Preparation of Peptide Stock Solution*

Lyophilized peptides (0.001 g) were mixed with 20 mL nuclease-free water (Ambion, USA) in a centrifuge tube and ultra-sonication was used to facilitate dissolution. The final concentrations of peptide stock solutions were around 0.06 mM. Solutions were diluted to 0.5 - 5 μM for other experiments.

2.2.4 *In situ AFM Imaging*

40 μL of peptide solution was added on top of a freshly cleaved MoS_2 bulk crystal surface (3 mm × 3 mm; Manchester Nanomaterials, UK) for incubation inside the AFM liquid cell at room temperature. In situ images were captured using silicon probes (SNL, k: 0.12 N/m, tip radius: 2 nm; Bruker) and silicon nitride probes (OTR4 and OTR8, k: 0.08 N/m, 0.15 N/m, tip radius: 15 nm; Bruker) under tapping mode or contact mode with a Cypher ES AFM (Asylum Research) and

a Nanoscope VIII (Bruker) at room temperature. Images were analyzed using Nanoscope Analysis v1.5 (Bruker) and Gwyddion SPM data analysis software.

2.2.5 *In situ High-speed AFM Imaging*

20 μL growth solution was added on top of freshly cleaved MoS_2 surface (3 mm × 3 mm). The experiment was done on a Cypher VRS AFM (Asylum Research, CA) with USC-F-1.2-k0.15 probes from Nanoworld. The probes typically had a resonance frequency of 1.2 MHz and a spring constant of 0.15 N/m. Offline data processing was done by Gwyddion SPM data analysis software and Asylum AFM software that was written using Igor from WaveMetrics.

2.3 Results and Discussions

2.3.1 *Assembled Structure of MoSBP1 Peptides on MoS_2 (0001) Surfaces*

The peptides consisted of seven amino acids (Tyr-Ser-Ala-Thr-Phe-Thr-Tyr, YSATFTY, named MoSBP1) with acylated and amidated N- and C-terminals, respectively, to reduce electrostatic interactions (Figure 2.1) [176]. When incubated with freshly cleaved MoS_2 substrates, MoSBP1 assembled into elongated islands aligned along three equivalent directions on MoS_2 (0001) and exhibited aspect ratios that decreased with increasing peptide concentration (Figure 2.2, A to C) [175]. The islands were ~0.7 nm in height (Figure 2.3), indicating they were one monolayer thick, and consisted of parallel rows with 4.1 nm periodicity (Figure 2.2, D to F, and Figure 2.4). Comparison of the row directions to the underlying MoS_2 (0001) lattice demonstrated that they formed at an angle of 30° to the densest sulfur packing directions (Figure 2.5).

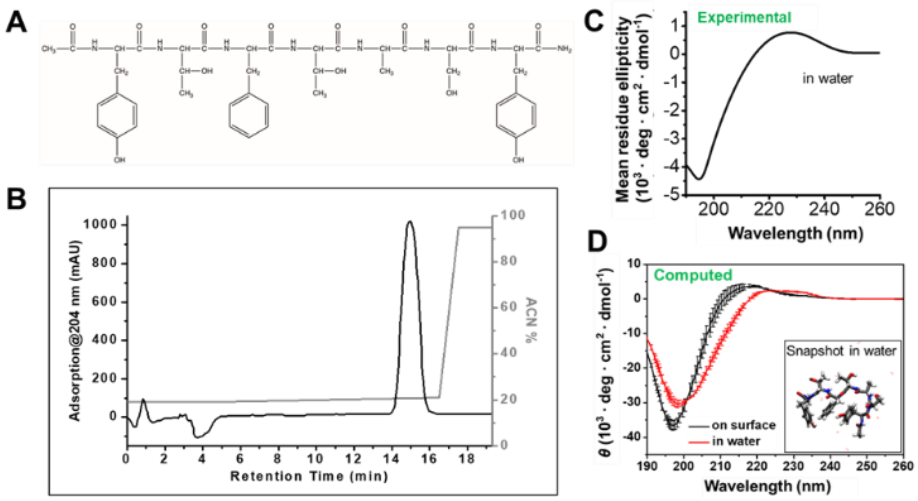

Figure 2.1. (A) Chemical structure of MoSBP1(YSATFTY, Tyr-Ser-Ala-Thr-Phe-Thr-Tyr; with N-terminal acylation and C-terminal amidation). (B) HPLC spectrum of MoSBP1. The black line is the HPLC spectrum and indicates a high purity close to 100%. The grey line is the approximate gradient of acetonitrile versus water. (C and D) The experimental and computed CD spectrums indicate that MoSBP1 adopted a random coil structure in water and the influence of secondary structure can be neglected. Reprinted with permission from [175]. Copyright 2018, AAAS.

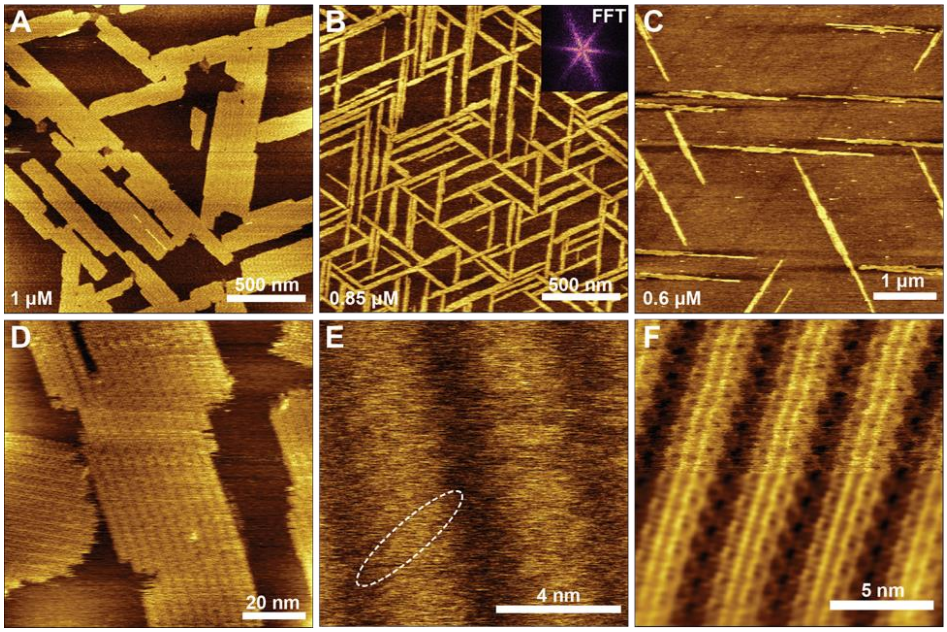

Figure 2.2. In situ AFM images of MoSBP1 on MoS_2 (0001). (A to C) Self-assembled structure at different concentrations. (D) Islands consist of co-aligned rows with

uniform spacing. (E) Non-contact mode image showing each row consists of small building blocks lying at ~60° to the row orientation. (F) High-resolution contact mode image showing detailed structure with connections between rows. The bottom half of F was FFT filtered. Reprinted with permission from [175]. Copyright 2018, AAAS.

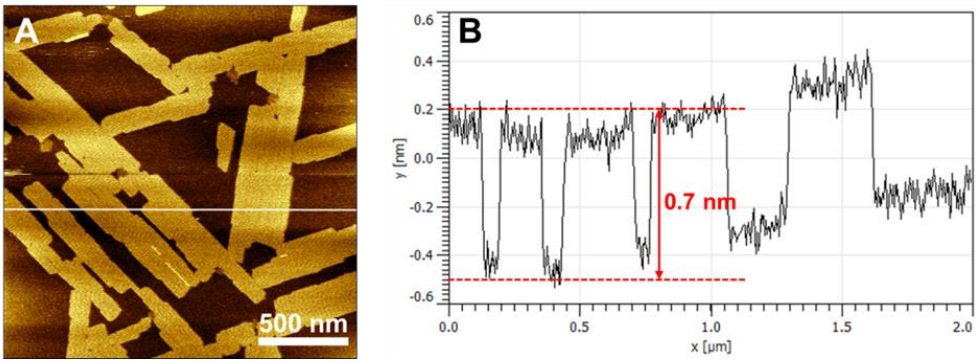

Figure 2.3. (A) In situ AFM image of the assembled islands of MoSBP1. (B) Height profile along the white line in A. The heights of these islands were ~0.7 nm, indicating a monolayer coverage of peptides on the surface. Reprinted with permission from [175]. Copyright 2018, AAAS.

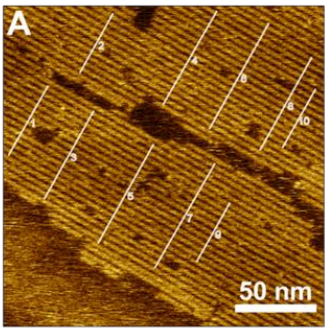

B

#	Length (nm)	Num. of Rows	Average Width (nm)
1	49.1	12	4.09
2	41.7	10	4.17
3	62.4	15	4.16
4	66.8	16	4.18
5	70.4	17	4.14
6	75.0	18	4.17
7	74.5	18	4.14
8	65.9	16	4.12
9	41.4	10	4.14
10	41.4	10	4.14
Average			4.14 ± 0.03

Figure 2.4. (A) High resolution in situ AFM image of the assembled islands of MoSBP1 shows that the peptide rows were uniformly arranged with equal width. (B) The width of peptide rows was ~4.1 nm. Reprinted with permission from [175]. Copyright 2018, AAAS.

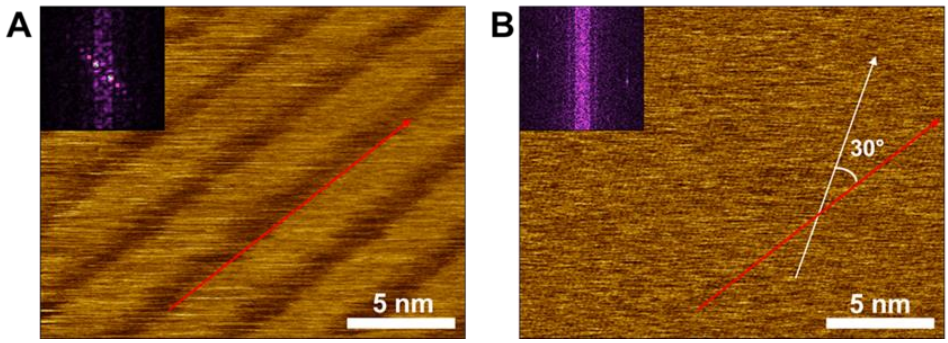

Figure 2.5. (A) High resolution in situ AFM image of an assembled island of MoSBP1 showing the row direction on MoS_2. Inset shows FFT of main panel. (B) Atomic-resolution AFM image showing the orientation of MoS_2 lattice beneath A. Inset shows FFT of main panel. Comparison between images and insets shows that there was a 30° difference between the row direction and one of the closest packing direction of sulfur atoms. Reprinted with permission from [175]. Copyright 2018, AAAS.

Molecular resolution imaging showed each row consists of ~1.1 nm by 4.7 nm units running at ~60° to the rows (Figure 2.2, E and F), demonstrating the highly ordered structure of each row (Figure 2.2 F and Figure 2.6) [175]. The dimensions and symmetry of the units were consistent with dimer formation with the same terminus of the two monomers facing one another (C-to-C or N-to-N) for the following reasons. First, the length of each unit was ~1.7 times the maximum possible length of a fully extended MoSBP1 molecule. Second, the units exhibited two-fold symmetry down to a sub-molecular level. Third, the central portion of each unit was higher than the ends, suggesting overlap of the peptides in that region. Fourth, the absence of chains extending along the direction parallel to the dimers, which would result in variable row widths, excluded an N-to-C or C-to-N association within the dimers. Finally, ring-like structures ~0.5 nm in diameter, similar to the size reported in other AFM studies of a flat-lying phenyl ring [177], lay symmetrically on both sides of the rows (Figure 2.6 C).

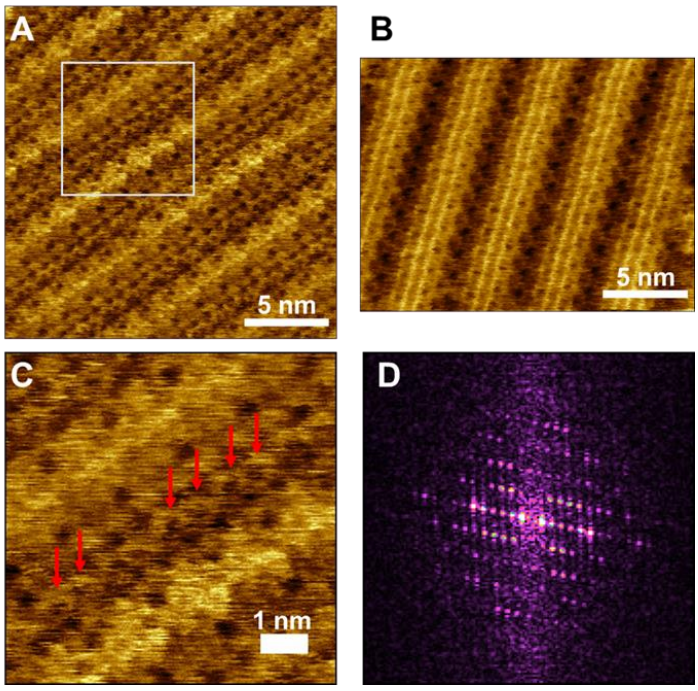

Figure 2.6. (A and B) High resolution in situ AFM images of the assembled rows of MoSBP1. (C) Digital zoom-in of the selected part of A. Red arrows point out the ring-like structures ~0.5 nm in diameter along both sides of the row. (D) FFT of B. A, B, and D indicate a highly ordered assembly structure of MoSBP1 on MoS_2 (0001) surface. Reprinted with permission from [175]. Copyright 2018, AAAS.

2.3.2 *Molecular Dynamics Simulations*

To understand the detailed structure and key interactions that stabilized the film, we performed MD simulations using the CHARMM-Interface force field [178] starting with single peptides on MoS_2 (Figure 2.7 A) [175]. Models of the peptide (MoSBP1), water molecules (TIP3P) and a (0001) surface of 2H-MoS_2 were created using the Builder module of the Materials Studio program. Models of the MoS_2 surface were obtained using the crystal structure data for the hexagonal unit cell reported by Wyckoff [179] and processed into multiples of an orthorhombic super cell. A 3D periodic box of pre-equilibrated water was obtained by MD simulation in the NPT ensemble. For simulations of single peptides in contact with the MoS_2 surface in aqueous solution,

one peptide, 2500 water molecules, and an extended MoS_2 (0001) surface with the dimensions of 49.27 × 50.57 × 24.59 $Å^3$ were employed. To investigate the interaction of multiple peptides with the MoS_2 surface in aqueous solution, 100 peptides, 43702 water molecules, and a surface model of the dimensions 295.59 × 142.22 × 24.59 $Å^3$ were employed.

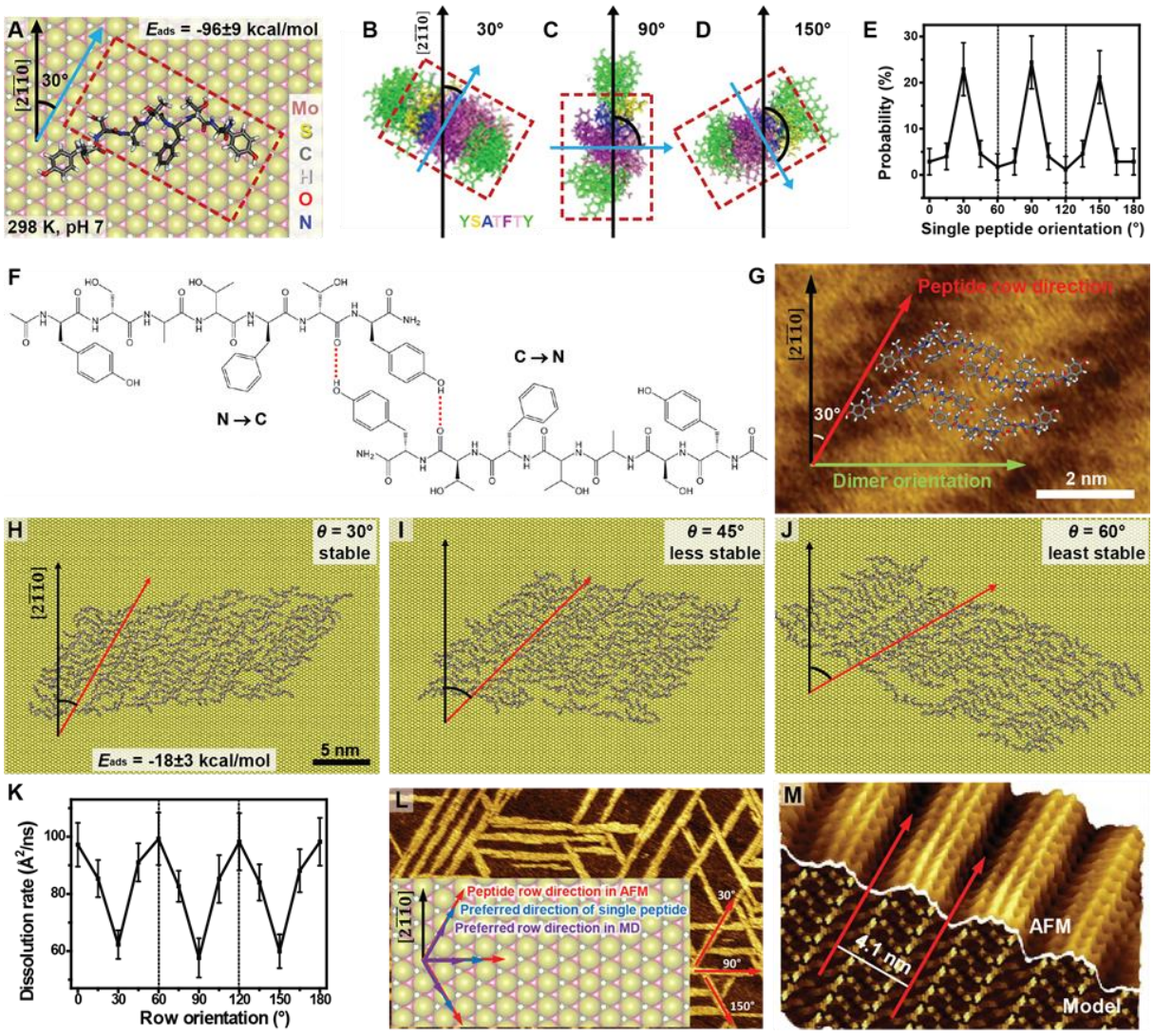

Figure 2.7. Predicted alignments of MoSBP1, dimers, and assemblies on MoS_2 (0001) from MD simulations. (A) Favorable binding conformation of a single peptide. (B to D) Preferred orientations of single peptides on surface colored by residue. Red boxes and blue arrows in A to D show main body and direction of a single peptide. (E) The probability of a single peptide at different angles relative to $[2\bar{1}\bar{1}0]$ direction. (F) Proposed dimer arrangement stabilized by hydrogen bonds. (G) Overlapping of the

most stable dimer conformation on an AFM image. Dimer direction points from a phenyl ring at one end of dimer to another phenyl ring at the other end, which shows a 60° difference from the row direction. (H to J) Snapshots of ~20 nm peptide assemblies with the dimer arrangement in G at different orientations on the surface. (K) The stability (dissolution rate) is the highest (lowest) at 30°, 90°, and 150°. (L) Preferred orientations from MD agree with experiment. (M) Simulated AFM image of peptide rows along preferred orientation is consistent with AFM data. Reprinted with permission from [175]. Copyright 2018, AAAS.

For the study of adsorption of single MoSBP1 peptide on the MoS_2 surface, we first placed a peptide molecule 1 nm away from the surface. The peptide reached the surface within 1 ns simulation time in the NPT ensemble at 298 K, and several equilibrium conformations were selected for follow-on simulations. The adsorption energy (E_{ads}) was determined by using a four-box method that included peptide-surface-water, peptide-water, surface-water, and water systems. Six independent simulations for the peptide-surface-water and peptide-water systems were carried out to sample conformations, and to obtain average energies and standard deviations [175]. Simulation trajectories were analyzed using the Visual Molecular Dynamics (VMD) program.

The MoSBP1 binding energy was -96 ± 9 kcal/mol in the preferred orientation (Figure 2.7 A) and originated from the replacement of ~25 water molecules in direct contact with MoS_2 surface; these were weakly bound and gained more hydrogen bonds upon release into the solution (Figure 2.8, A to C) [175]. There was also an entropy gain of water molecules upon release from the surface and an entropy loss of the peptide upon binding. Hydrogen bonding among water molecules near the MoS_2 surface was non-ideal, mainly because shielding by the surface allowed only about one hydrogen bond per water molecule rather than two hydrogen bonds per water molecule in the bulk. The maximum entropy contribution to water release, from entirely frozen to liquid, given as a free-

energy $-T\Delta S$, equals the melting enthalpy of water (-1.5 kcal/mol). Due to weak attraction (contact angle 69°) and high residual mobility, only a small part of this theoretical entropy would be reversibly lost and regained, i.e., less than -0.5 kcal/mol. Therefore, the entropy contribution, as $-T\Delta S$, would be about -12 kcal/mol for 25 released water molecules. The entropy loss of the peptide upon binding, assuming 3 free rotational states per amino acid, was $-T\Delta S = +RT \cdot \ln 3^7 = +5$ kcal/mol, and partially compensated the entropy increase from released water. On balance, the entropy contribution to the free-energy of adsorption was then approximately -7 ± 3 kcal/mol, suggesting a free-energy of adsorption for a single peptide of -103 ± 10 kcal/mol [175]. Similar considerations have been previously suggested [180] and verified by free-energy calculations [181].

The force field parameters for the peptide were taken from CHARMM27 and parameters for MoS_2 (Table 2.1) were newly derived using the same energy expression following the Interface Force Field (IFF) protocol [178]. The parameters for MoS_2 represent chemical bonding with internal dipole moments expressed via atomic charges, lattice parameters, interfacial energies, and energy derivatives in agreement with experiment, enabling thermodynamic consistency. The MoS_2 force field in IFF reproduces the molecular and lattice geometry of MoS_2, interfacial properties represented by contact angles of water and diiodomethane on a freshly cleaved MoS_2 surface, and mechanical properties (bulk modulus, Young's modulus) in excellent agreement with experimental measurements (Table 2.2). It can thus be assumed that peptide interactions with the MoS_2 surfaces such as computed binding energies and conformations would closely agree with measurements [175], if available, within ±10%, as previously shown for other surfaces with IFF [182].

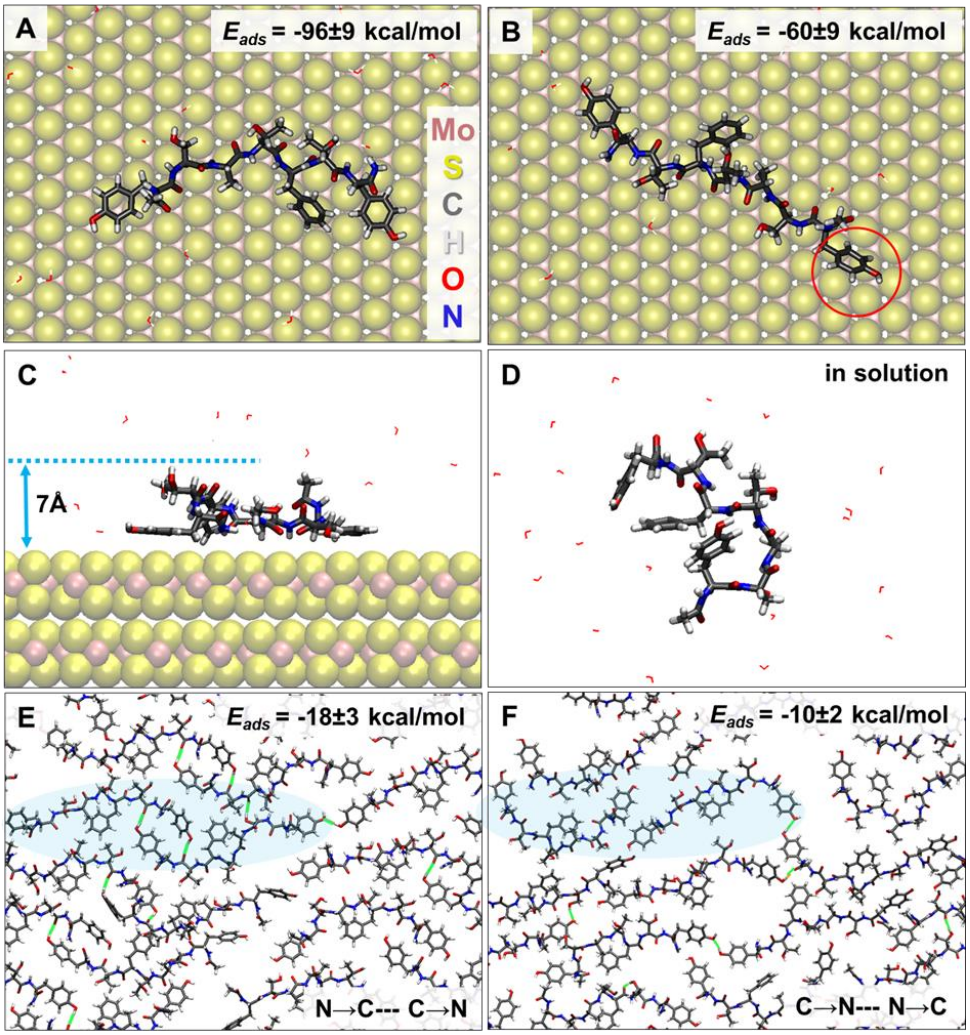

Figure 2.8. Further insights from molecular dynamics simulations. (A and B) Top views of a single MoSBP1 with the favorable (A) and less favorable (B) conformation on MoS_2 surface in solution. (C) Side view of the favorable conformation, showing flat-on binding of two phenyl rings. The height of MoSBP1 is 7 Å. (D) Snapshot of equilibrium conformation for a single MoSBP1 in solution. (E and F) Representation of different dimer arrangements, N→C---C→N (E) and C→N---N→C (F) on the MoS_2 surface in solution after 3 ns NPT simulation, whereby (E) is preferred. In A to D, water molecules are represented in red. In E and F, surface and water are not presented for a clear view. Hydrogen bonds are represented by green lines (distance cutoff of 3 Å and an angle limitation of 180 ± 20°). The blue region represents a single dimer. Reprinted with permission from [175]. Copyright 2018, AAAS.

Table 2.1. Force Field Parameters for 2H-MoS_2. Reprinted with permission from [175]. Copyright 2018, AAAS.

I. Nonbond	**Charge (e)**	**σ (pm)**	**ε (kcal/mol)**
Mo	+0.50	480	0.07
S	-0.25	385	0.3
II. Bond	**r_0 (pm)**	**k_r (kcal mol^{-1} $Å^{-2}$)**	
Mo-S	239	118	
III. Angle	**θ_0 (°) ***	**k_θ (kcal mol^{-1} rad^{-2})**	
∠Mo-S-Mo	84.32	205	
∠S-Mo-S	84.32	205	
	134.4	3.6	
	78.8 and 134.4	0	

* The values match data from XRD and are not adjustable parameters.

Table 2.2. Validation of the Force Field Parameters. Reprinted with permission from [175]. Copyright 2018, AAAS.

Property	**Computed**	**Experimental**	**deviation**
lattice parameter			
a×b×c ($Å^3$)	25.282×18.962×24.5	25.283×18.962×24.59 [183]	0.0-0.4%
density (g/cm^3)	5.02	4.998-5.06 [183,184]	< 0.5%
mechanical			
bulk moduli (GPa)	42	46 [185]	9%
Young's moduli (GPa)	180 (in-plane)	170-370 (in-plane) [186]	agrees
surface contact angle (°)			
water	69	69.2 [187]	< 1%
diiodomethane	14.7	15.2 [187]	~4%

We then tested all possible peptide orientations, without constraints in any direction, and found that the backbone preferred to align in the densest sulfur packing direction (Figure 2.7, A to D). Defining the direction of a single peptide as the orientation perpendicular to the main body of the peptide, we found a strong preference for single peptides to align at 30°, 90°, and 150° relative to the $[2\bar{1}\bar{1}0]$ direction of MoS_2 lattice (Figure 2.7, B to E), matching the observed row directions.

To understand the stabilization of peptide rows, we simulated numerous dimer configurations, the most stable of which is shown schematically in Figure 2.7 F and overlain on an AFM image in Figure 2.7 G [175]. We tested the stability of large assemblies of these dimers ~20 nm in size with different row orientations relative to the lattice in MD simulations (Figure 2.7, H to J). Peptide row stability was again substantially higher when aligned at 30°, 90°, and 150° relative to $[2\bar{1}\bar{1}0]$ (Figure 2.7 K). In all cases, some disorder was introduced during the simulation, presumably because of the smaller domain size compared to experiments and some limitations in both conformation sampling and force fields.

The most stable structures (Figure 2.7 K) were consistent with the topography seen by AFM (Figure 2.7 L), and a simulated AFM image based on the MD results (Figure 2.7 M) confirmed the importance of the phenyl rings of Tyr and Phe in surface recognition and attachment (Figure 2.8, A to C). The dimer itself was stabilized by hydrogen bonds between the -OH of Tyr7 and the -C=O of Thr6, and possibly π-π stacking between phenyl rings (Figure 2.7 F). Interestingly, the adsorption of multiple peptides in large assemblies reduced the attraction per peptide from -96 to -18 kcal/mol (Figure 2.7, A and H). Although this energy still corresponded to strong binding, the result indicated the required removal of 25 water molecules to bind a single peptide was kinetically prohibited and that the ordered domains of dimer rows represented a metastable state, which was more rapidly achieved via hydrogen bonding and van der Waals interactions (Figure 2.8, E and F).

2.3.3 *Assembly Pathway and Kinetics of Array Formation*

We further investigated the pathway and kinetics of array formation by continuously monitoring assembly by AFM with scan rates as high as 2.56 s/frame (Figure 2.9, A to O, and Figure 2.10) [175]. The results showed that MoSBP1 nuclei exhibited the elongated structure of mature islands and grew along the preferred lattice directions from their first appearance with no evidence of a transient precursor phase or attachment of large clusters over the course of ~900 sequential frames (Figure 2.9, F to O, and Figure 2.10). Moreover, the characteristic 4.1 nm rows aligned along one of the three preferred directions were observed even in the smallest islands with lengths as short as ~8 dimers (~9 nm) (Figure 2.9, G and L), further indicating a direct nucleation pathway.

The circular dichroism spectrum of MoSBP1 showed a minimum around 195 nm and a maximum around 226 nm (Figure 2.1 C), which were typical signals from random coil structures where the monomer subunits were oriented randomly while still being bonded to adjacent units [188]. Thus, the influence of secondary structure in MoSBP1 could be neglected. In MD simulations, close contact between two peptides was observed for only 1-2% of time over tens of nanoseconds, and dimers in solution dissociated quickly after formation. In addition, computed time-average CD spectra of single peptides in solution showed an excellent fit to the experimentally measured CD spectrum (Figure 2.1, C and D). These results showed that MoSBP1 preferred to remain in a monomeric state in bulk solution, suggesting that these were the likely growth units.

In the early stages of assembly, a few islands grew along directions lying at 30° to the preferred directions but disappeared over time (~25 min) (Figure 2.11). Islands that grew along the preferred directions sometimes dissolved as nearby islands grew (~10 min) (Figure 2.12).

These observations demonstrated both the higher stability of islands exhibiting dominant orientations and the reversibility of peptide binding.

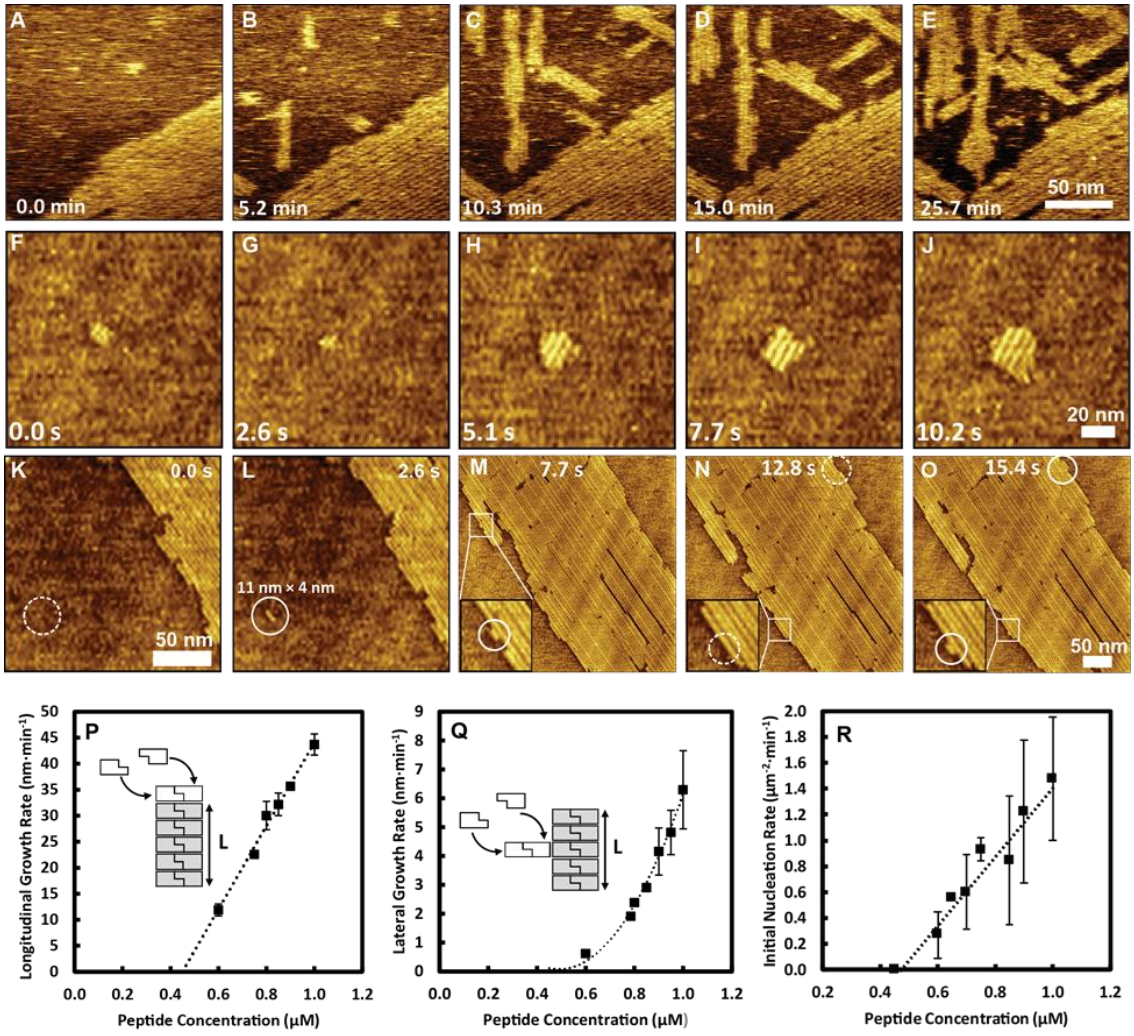

Figure 2.9. Nucleation and growth dynamics of MoSBP1 on MoS_2 (0001). (A to E) In situ AFM images show that the peptides attached to the surface and directly grew into ordered structures. (F to J) In situ high-speed AFM images showing the formation and development of a small island. (K and L) In situ high-speed AFM images showing nucleation of a single row. (M to O) In situ high-speed AFM images showing the creation of new rows adjacent to existing ones. Circles highlight regions where new rows appear (dashed: before; solid: after). (P to R) The longitudinal (P) and lateral (Q) island growth rates and initial nucleation rate (R) vs. peptide concentration. Reprinted with permission from [175]. Copyright 2018, AAAS.

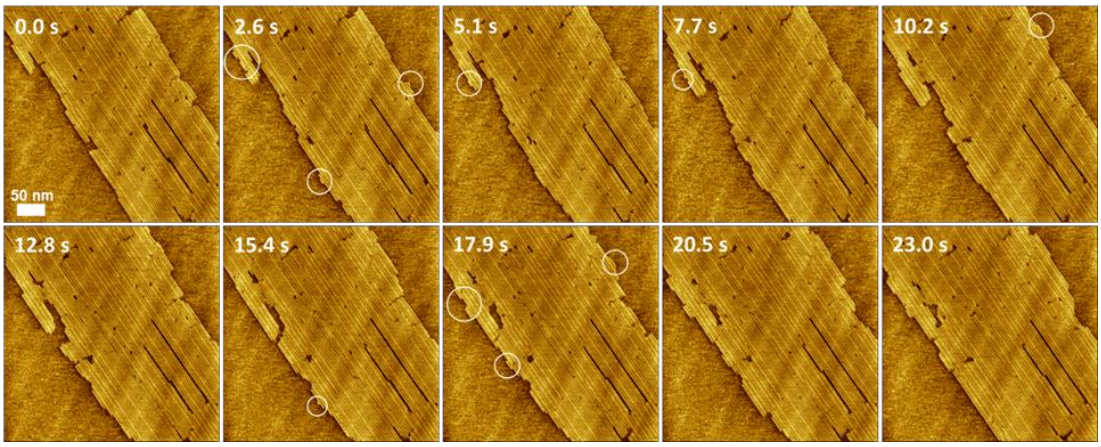

Figure 2.10. High-speed AFM images collected at a frame rate of 2.56 s/frame showing the growth of peptide rows and the creation of new rows adjacent to the existing rows. Circles highlight regions where new rows were added. No metastable oligomeric species or amorphous precursors were observed adsorbing to the surface or attaching to the rows in any of the ~900 images collected during the growth process. Reprinted with permission from [175]. Copyright 2018, AAAS.

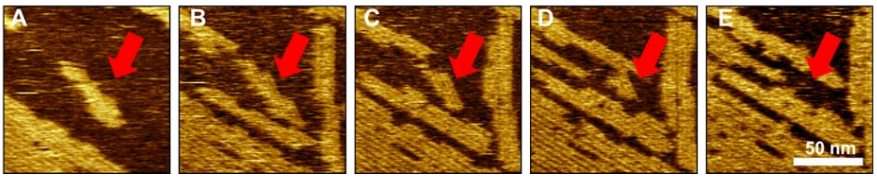

Figure 2.11. (A to E) In situ AFM images collected with 0.75 µM MoSBP1 taken at t = 24.8 (A), 30.0 (B), 35.1 (C), 39.8 (D) and 50.5 (E) min show that mis-aligned islands lying at 30° to the dominant directions could exist but would disappear over time (~25 min). Reprinted with permission from [175]. Copyright 2018, AAAS.

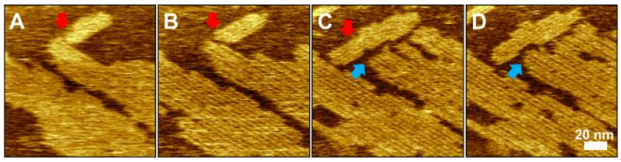

Figure 2.12. (A to D) In situ AFM images collected with 0.75 µM MoSBP1 taken at t = 24.8 (A), 30.0 (B), 35.1 (C) and 39.8 (D) min show that island growing along one of the three dominant orientations sometimes dissolved as nearby island grew (see arrows). Reprinted with permission from [175]. Copyright 2018, AAAS.

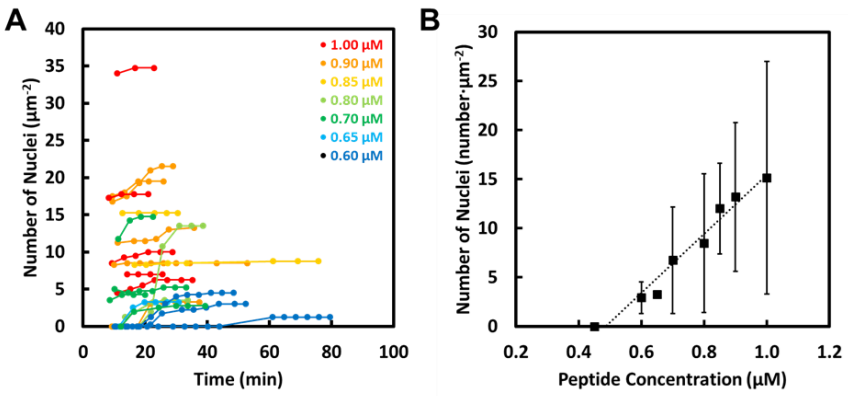

Figure 2.13. (A) The number density of nuclei reached a balance as islands approach one another and prevent the appearance of new nuclei through competition for peptide adsorbates. (B) Asymptotic number density of nuclei (MoSBP1) varied linearly with peptide concentration. Reprinted with permission from [175]. Copyright 2018, AAAS.

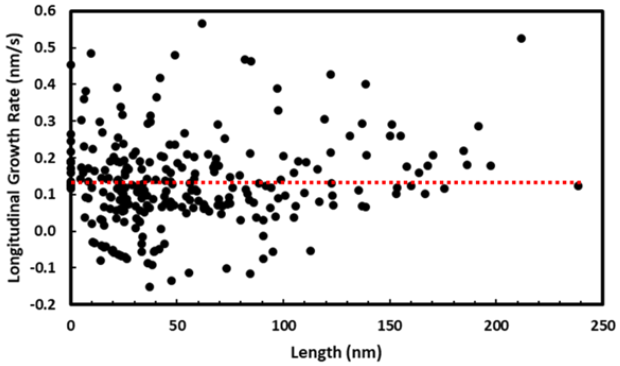

Figure 2.14. Measured longitudinal growth rates of islands vs. their lengths. The rates for all islands were measured during a single experiment. On average, they showed a similar and constant longitudinal growth rate of ~0.13 nm/s, independent of island length. In addition, there was no lower limit to the length of islands that exhibited finite growth rates, indicating that there was no critical island length. Reprinted with permission from [175]. Copyright 2018, AAAS.

To understand the energetic controls on assembly, we used time-resolved in situ data to measure nucleation and growth rates, which revealed the crucial role of row-by-row assembly in

controlling film formation [175]. The longitudinal speed v_{lg} was ∝ peptide concentration c (Figure 2.9 P), whereas the lateral speed $v_{la} \propto c^2$ (Figure 2.9 Q). The initial nucleation rate J_n was also ∝ c (Figure 2.9 R), as was the number density of nuclei n_∞ approached asymptotically as time $t \rightarrow \infty$ (Figure 2.13). Moreover, the concentration below which $J_n = 0$ (0.48 μM), within error, was identical to that at which v_{lg} and v_{la} reached zero (0.45 μM) — i.e., the island solubility limit c_e — and there was no lower limit to the size of nuclei that grew spontaneously (Figure 2.14). Thus, nucleation began as soon as c exceeded c_e, $J_n \propto c$, and the critical island size $N_c = 0$.

These observations are seemingly in violation of predictions of CNT, which hold that 2D islands exhibit a critical size below and above which islands will, on average, dissolve and grow, respectively, and that N_c should scale inversely with supersaturation σ. Moreover, in 2D, CNT predicts an exponential dependence of J_n on σ, leading to a strongly nonlinear dependence on c [171]. We can reconcile the apparent contradictions and understand all of the observed phenomena by recognizing that, although the final islands are 2D, they form one row at a time. The free-energy barrier of CNT arises from the difference in the dimensional dependence between the free-energy change ΔG associated with the drop in chemical potential upon crystallization and that associated with surface (3D) or line (2D) tension of the new phase. In two dimensions, the (negative) first term scales with island area A, while the (positive) second term is proportional to the perimeter. The second dominates at small size, but the first eventually wins out, giving rise to a barrier at finite A and a critical size N_c (Figure 2.15) [171]. In contrast, in 1D, both contributions to $\Delta G \propto$ the length L of the nucleus, consequently, there is no barrier, and $N_c = 0$ (Figure 2.15). Moreover, according to the classical nucleation theory, we fitted the measured nucleation rate using 3D and 2D models [171]. The surface energy, α, and step edge energy, γ, that resulted from fitting the data with these models were $\alpha = 6.2 \times 10^{-4}$ J/m^2, $\gamma = 1.3 \times 10^{-12}$ J/m. The latter gave a step edge energy

per height, γ/h = 1.8 × 10^{-3} J/m^2. These values were about an order of magnitude smaller than expected for small organic molecules (~10 × 10^{-3} J/m^2), indicating that, in addition to providing poor fits to the data, the predictions of the 3D and 2D models were not reasonable. Thus, when the assembly process is viewed as continual nucleation of 1D rows, rather than conflicting with CNT, the results verify its long-standing prediction that nucleation of 1D structures occurs without a free-energy barrier.

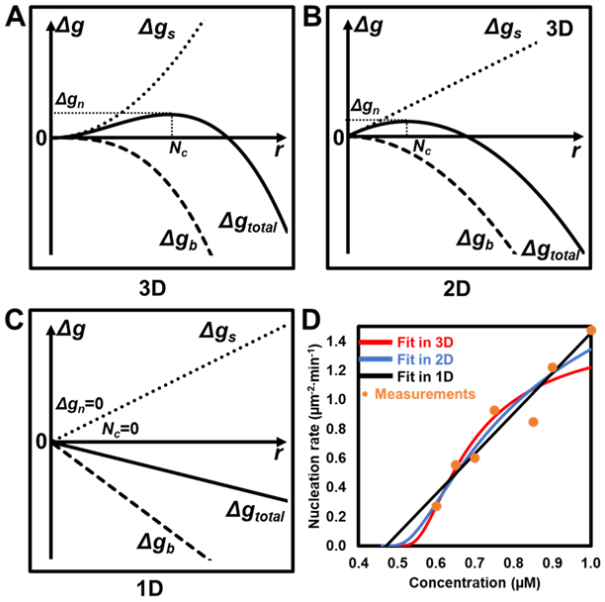

Figure 2.15. (A to C) Free-energy changes predicted by classical nucleation theory for 3D, 2D, and 1D systems, respectively. Δg_b is the free-energy change associated with the drop in chemical potential upon crystallization and Δg_s is the free-energy change associated with the surface (3D) or line (2D) tension of the new phase. C shows that there is no free-energy barrier for 1D nucleation. (D) Nucleation rate data fit using the three different models. The curves were plotted based on the best fit parameters of the three different models. Reprinted with permission from [175]. Copyright 2018, AAAS.

The distinction between the nucleation kinetics of MoSBP1 rows and that of amyloid fibrils, which comprise a quasi-1D material, further highlights the 1D nature of MoSBP1 nucleation. In

the amyloid fibril system, which exhibits similar 1D growth behavior, a two-step condensation-ordering process with a nucleation barrier is widely observed [189]. However, in that system, the initial formation of the disordered oligomeric precursor phase comprises the nucleation step and leads to the typical shape of nucleation barrier in 3D as described by CNT [189].

The fact that there is no free-energy barrier to nucleation does not mean nucleation or, for that matter, growth is unopposed by kinetic barriers associated with molecular-level processes, such as desolvation, conformational changes, or breaking and making of hydrogen bonds. However, these activation barriers are fundamentally different from free-energy barriers that are associated with the ability of the system to explore all the available configurational states and are governed by the probability of a state comprised of an island larger than the critical size. The activation barriers do not depend on supersaturation and thus have no impact on the dependence of J_n on σ.

The difference in the concentration dependence of longitudinal and lateral growth rates can also be understood as a consequence of row-by-row growth [175]. Monomers that attach at the row ends are strongly bound and every attachment is an independent event. Thus, v_{lg} should be linear in c, as observed (Figure 2.9 P). However, to form a new row (n = 2) adjacent to the first (n = 1), the weakness of end-to-end binding causes the attached monomers to have low stability and requires a second attachment event before the first monomer detaches in order to create a stable dimer (Figure 2.9 Q). Hence, v_{la} should be quadratic in c. This difference explains why increasing c leads to smaller island aspect ratios (Figure 2.2, A to C): the rate at which rows $n \geq 2$ are created relative to the rate at which existing rows lengthen $\propto (c - c_e)$. In addition, the fact that the lateral growth rate also reaches zero at $c = c_e$ further demonstrates the barrier-free nature of nucleation in this system. The lateral growth rate is directly proportional to the rate at which new rows nucleate heterogeneously along existing rows. While this rate can be expected to exceed that of new,

isolated rows (i.e., homogeneous nucleation), in CNT the kinetics of heterogeneous nucleation are governed by the same expressions with a modified value of the surface or line tension. Thus, a critical size and barrier are expected, contrary to the experimental results.

The question then arises as to why the nucleation rate of the first row is linear in *c*, while that of rows n ≥ 2 is quadratic. We constructed a set of rate equations to describe the creation and destruction of all adsorbed species, including monomers, dimers, and rows as a function of time.

$$\frac{dn_c}{dt} = k_c^+ \cdot c \cdot n_n - k_c^- \cdot n_c \tag{2.1}$$

$$\frac{dn_n}{dt} = k_n^+ \cdot c \cdot n_m - k_n^- \cdot n_n - k_c^+ \cdot c \cdot n_n \tag{2.2}$$

$$\frac{dn_m}{dt} = k_m^+ \cdot c \cdot (1 - n_m - n_n - n_c) - k_m^- \cdot n_m + k_n^- \cdot n_n - k_n^+ \cdot c \cdot n_m \tag{2.3}$$

where *c* is the peptide concentration, n_c, n_n, and n_m are the number densities of new rows (islands), dimers (nuclei), and adsorbed monomers, respectively, and k_c^+, k_c^-, k_n^+, k_n^-, k_m^+, and k_m^- are the rate coefficients for formation of a dimer to an existing dimer to create a row, destruction of a row by detachment, monomer attachment to an adsorbed monomer to form a nucleus, destruction of a nucleus by detachment, monomer adsorption, and monomer desorption, respectively.

At small *t* with low coverage of rows, we have n_n, $n_c \ll n_m \leq 1$. Here we assume that the rate coefficient for addition of a dimer to an existing dimer is close to that of the first dimer, $k_c^+ \approx k_n^+$, and row destruction is negligible due to the stability of the rows, $k_c^- \approx 0$. Also, as an intermediate species, it's also safe to assume that the number density of attached monomer is stable, which means $\frac{dn_m}{dt} = 0$. So, we can rewrite the equations as,

$$\frac{dn_c}{dt} = k_n^+ \cdot c \cdot n_n \tag{2.4}$$

$$\frac{dn_n}{dt} = k_n^+ \cdot c \cdot n_m - k_n^- \cdot n_n - k_c^+ \cdot c \cdot n_n \tag{2.5}$$

$$\frac{dn_m}{dt} = k_m^+ \cdot c \cdot (1 - n_m) - k_m^- \cdot n_m + k_n^- \cdot n_n - k_n^+ \cdot c \cdot n_m = 0 \tag{2.6}$$

The solutions to these equations are given by,

$$n_n = \frac{A+D}{B} \cdot (e^{Bt} - 1) \tag{2.7}$$

$$n_c = E\left[\frac{1}{B}(e^{Bt} - 1) - t\right] \tag{2.8}$$

where,

$A = \frac{k_m^+ k_n^+ c^2}{c(k_m^+ + k_n^+) + k_m^-}$, $B = \frac{k_n^+ k_n^- c}{c(k_m^+ + k_n^+) + k_m^-} - k_n^- - k_c^+ c$, $D = -\frac{k_m^+ k_n^+ c_e^2}{c_e(k_m^+ + k_n^+) + k_m^-}$, $E = -\frac{(A+D)k_n^+ c}{B}$

When *t* is small, the number density of islands becomes,

$$n = n_n + n_c \approx (A + D)t + \frac{EB}{2}t^2 = (A + D)t + \frac{(A+D)k_n^+ c}{2}t^2 \tag{2.9}$$

$$n \approx (A + D)t = \left[\frac{k_m^+ k_n^+ c^2}{c(k_m^+ + k_n^+) + k_m^-} - \frac{k_m^+ k_n^+ c_e^2}{c_e(k_m^+ + k_n^+) + k_m^-}\right]t \tag{2.10}$$

Thus, the initial nucleation rate $\frac{dn}{dt}$ (near $t = 0$):

$$\frac{dn}{dt} \approx \frac{k_m^+ k_n^+ c^2}{c(k_m^+ + k_n^+) + k_m^-} - \frac{k_m^+ k_n^+ c_e^2}{c_e(k_m^+ + k_n^+) + k_m^-} \tag{2.11}$$

In the limit of high k_m^- — i.e., low coverage — $J_n \propto c^2$. However, at high high k_m^+ — high monomer coverage — $J_n \propto c$, because every adsorbing monomer had a high probability of finding a monomer that had already adsorbed. Thus, although the need to dock a monomer to the side of a row led to a quadratic dependence on *c* for nucleation of rows n ≥ 2, a high coverage of adsorbed monomers produced a linear dependence on *c* for the first row of any island [175].

2.3.4 *Impact of Sequence and Surface on the Assembly Pathway*

Finally, to determine the impact of sequence and surface on the pathway, we investigated assembly on MoS_2 (0001) by three other sequences: the reversed sequence MoSBP1-R (YTFTASY), the

scrambled sequence MoSBP1-S (SAYFYTT), and a weak-binding sequence MoSBP20 (TSHMSNT), as well as assembly of the original sequence on HOPG [175]. The reversed sequence MoSBP1-R assembled on MoS_2 into a structure similar to that of MoSBP1 (Figure 2.16, A to C), although a larger concentration (5 μM) was required to initiate nucleation and growth. For both the scrambled version MoSBP1-S, which still contained the phenyl rings and the weak-binding sequence MoSBP20, which contained no phenyl rings, no assembly occurred (Figure 2.16, D and E) even at c = 5 μM.

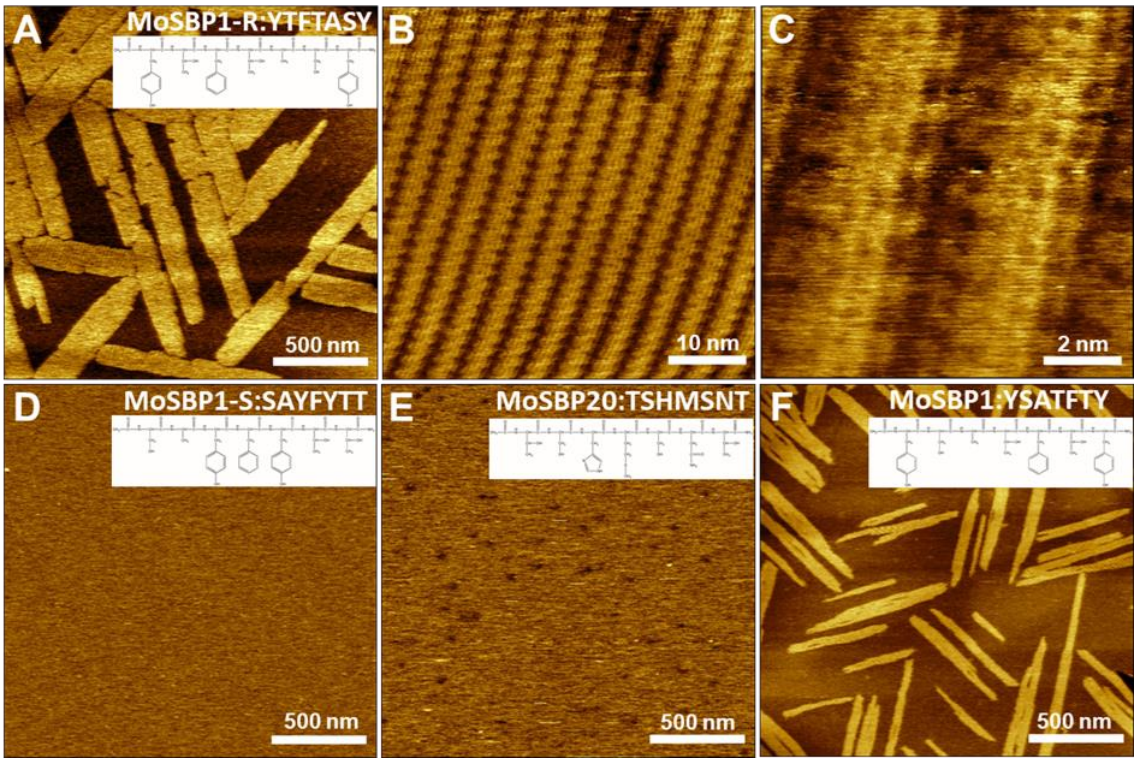

Figure 2.16. In situ AFM images of MoSBP1 on HOPG and other sequences on MoS_2 (0001). (A to C) Assembly of reversed version (MoSBP1-R) of original sequence at 5 μM on MoS_2 showing structure similar to that seen for MoSBP1. (D and E) No assembly occurred when scrambled version of MoSBP1 (MoSBP1-S) or a weak-binding sequence (MoSBP20) was used, even at 5 μM concentration. (F) MoSBP1 also assembled on HOPG and showed three-fold symmetry. Reprinted with permission from [175]. Copyright 2018, AAAS.

2.4 CONCLUSIONS

The use of peptides identified through phage display [173,174,176] has enabled control over formation of a wide range of materials [173,174,176,190–192] and surface-directed assembly of such peptides has been shown to modulate electronic properties of 2D materials [78]. In cases where structure has been investigated, patterns like those observed here are commonly reported. Our findings provide a mechanistic description of their formation and define the key controlling parameters [175].

The peptides investigated here [175] exhibit structural features common to many polymeric and chain-like organic molecules that self-assemble on surfaces [75,78,163–166,169,193]. They possess a mix of hydrophobic and hydrophilic groups, form many contacts between side chains and with both neighboring molecules and the underlying substrate and, by comparison, exhibit weak end-to-end binding. Indeed, a wide variety of systems form ordered 2D films exhibiting a row-by-row structure [75,78,193–195]. In addition, many peptides and other polymers form one-dimensional fibers in bulk solution that then interact to form 2D and 3D structures [196–199]. The above findings place these systems in the context of well-developed theories for the emergence of order and post-nucleation growth and provide a guide for interpreting and controlling their assembly.

Chapter 3. SELF-ASSEMBLY OF PEPTIDES ON GRAPHITE

3.1 INTRODUCTION

Two-dimensional materials such as molybdenum disulfide and graphite have demonstrated unique electrical and optical properties [200–202]. Patterning their surfaces with biomolecules including proteins, peptides, and DNAs under precise control is a crucial step towards the fabrication of biocompatible and bioactive 2D hybrid materials, which can have broad applications in biosensing, bioimaging, and biomedical engineering [203–206]. Peptides are widely explored for the functionalization of surfaces due to the structural diversity and the relative simplicity for design, simulation, and synthesis [182,207,208]. Various designs have been made to pattern the surfaces of 2D materials including mica [32,209], graphite [32,75,78,143,209–213], and transition-metal dichalcogenides [78,175,212,213]. Moreover, effects of sequence [75,78,212,213], electrostatic interactions [210], temperature [143,144], pH [211], and electrochemical bias [213] have also been investigated to control the assembled structures at the interfaces. However, little attention has been given to their nucleation and growth pathway. Whether assembly comes from a monomer by monomer growth mechanism or goes through a phase transformation process remains unclear. Understanding these fundamental backgrounds can better guide the design and fabrication of biomolecular assembly at solid-liquid interfaces. In this study, we explored the self-assembling behaviors of the phage-selected peptide, MoSBP1, on graphite surfaces. Our results demonstrated that these peptides could also assemble into ordered structures on graphite, similar to those observed on MoS_2 surfaces [175]. Besides, two distinct ordered states could coexist at the same time. The kinetically preferred metastable state followed the same row-by-row growth pathway described in our previous study [175]. It formed rapidly at high supersaturations and then dissolved gradually. The thermodynamically stable structure exhibited another possible row-by-row

mechanism, which included nucleation, diffusion, aggregation, and stabilization, similar to an "oriented attachment" process in two dimensions. The transition from the metastable to the stable state was not a direct phase transformation, yet it went through a dissolution-reprecipitation mechanism. Our study here demonstrates the importance of substrate in assembly pathway selection, and it also reveals the growth pathways and phase transformation mechanism of two distinct assembled structures on graphite surfaces, which can be used to guide and interpret different biomolecular self-assembling systems at solid-liquid interfaces.

3.2 METHODS

3.2.1 *Preparation of Peptide Solution*

The selection and synthesis of peptide MoSBP1 follow the same methods described in section 2.2.1. Lyophilized peptides powder (0.0005 g) were mixed with 10 mL nuclease-free water (Ambion, USA) in a centrifuge tube, and ultra-sonication was used to facilitate dissolution. The final concentrations of peptide stock solutions were around 0.06 mM. The stock solution was further diluted to 1 to 5 μM for AFM experiments.

3.2.2 *In situ AFM Characterization*

The AFM characterization was done with a Cypher ES AFM (Asylum Research). A freshly cleaved HOPG surface (12 mm × 12 mm) on top of a metal disc was set inside the AFM chamber. 40 μL of peptide solution was added onto the center of the HOPG surface and incubated at room temperature. In situ images were captured using silicon nitride probes (OTR4 and OTR8, k: 0.08 N/m, 0.15 N/m, tip radius: 15 nm; Bruker) under tapping mode or contact mode. Images were processed and analyzed using Gwyddion SPM data analysis software.

3.3 RESULTS AND DISCUSSIONS

3.3.1 *Nucleation-diffusion-aggregation Growth Mechanism on Graphite Surfaces*

The peptide, MoSBP1 (Tyr-Ser-Ala-Thr-Phe-Thr-Tyr, YSATFTY), was selected by the phage display technique for its strong binding affinity to MoS_2 (0001) surface. These peptides can form highly ordered structures along three equivalent directions on MoS_2 surfaces following a row-by-row growth process [175]. To explore the effect of substrates on the assembling behaviors, we tested the assembly of MoSBP1 on graphite surfaces, which were also hydrophobic and displayed a three-fold symmetry. When incubated with freshly cleaved HOPG substrates, MoSBP1 could also assemble into elongated 2D islands like the ones observed on MoS_2 (Figure 3.1). The height of the island was ~0.8 nm, indicating that they comprised monolayer-thick films (Figure 3.2). These islands also consisted of parallel rows with a uniform center-to-center distance around 4.5 nm (Figure 3.1 and Figure 3.2). These islands mainly aligned along three equivalent directions of graphite lattices. While misaligned peptide rows or islands were not stable on MoS_2 surfaces and would gradually dissolve, another two sets of metastable directions were also observed for these islands on graphite surfaces (Figure 3.1). The angle difference between these two sets of directions and the dominant one was 23.5° and -18.3°, respectively. Comparisons of the prevailing row directions to the underlying graphite lattice demonstrated that rows aligned at an angle of 30° to the zig-zag orientation of the graphite lattice (Figure 3.3).

By continuously monitoring the assembly process of MoSBP1 on graphite, our results revealed yet another assembly pathway made possible through the row-by-row growth mechanism. Most of the peptide rows comprising these 2D islands began as isolated, independent nuclei (Figure 3.4, A to D). Over time, the MoSBP1 rows, which were immobile on MoS_2, were able to diffuse across the graphite surface and aggregate to form the final compact, highly ordered 2D

domains (Figure 3.4, E and F). The lower stability and weaker binding of individual rows aligned along another two sets of directions enhanced the possibility for these rows to diffuse across the surface, aiding in the aggregation process. These results highlighted the critical role of the epitaxial match in tuning the assembly pathway at interfaces. While MoSBP1 exhibited commensurate epitaxial growth on MoS_2, the mismatch with the graphite lattice led to weaker binding to the substrate, which contributed to the observed mobility of the peptide rows. The nucleation-diffusion-aggregation growth mechanism of these 2D islands demonstrated an "oriented attachment" mediated growth process for these crystalline self-assembled structures in two dimensions.

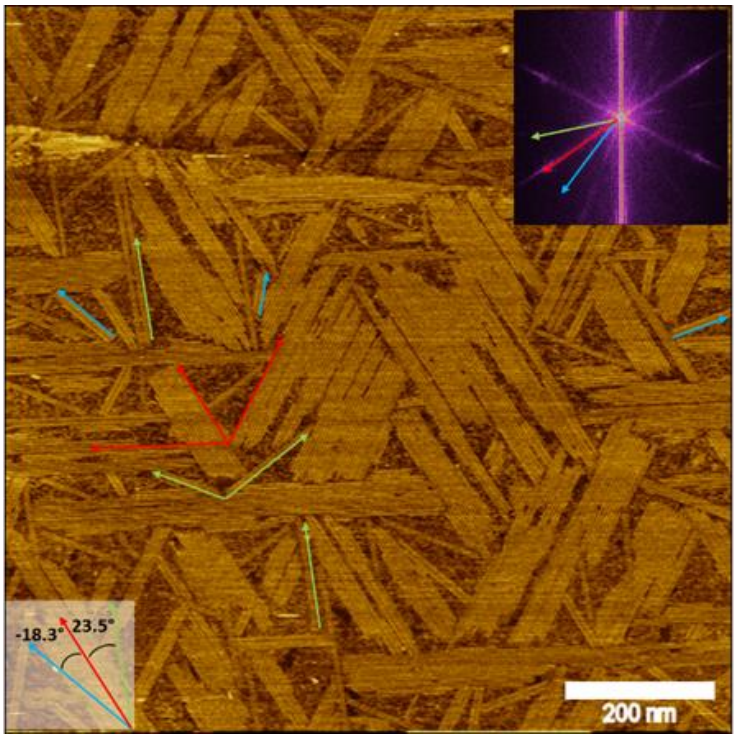

Figure 3.1. Self-assembled patterns of peptide MoSBP1 (5 μM) on a graphite surface. 2D islands mainly aligned along three equivalent lattice direction (marked with red arrows). However, there were another two sets of possible orientations (marked with green and blue arrows, respectively), which were also shown in the FFT image in the inset.

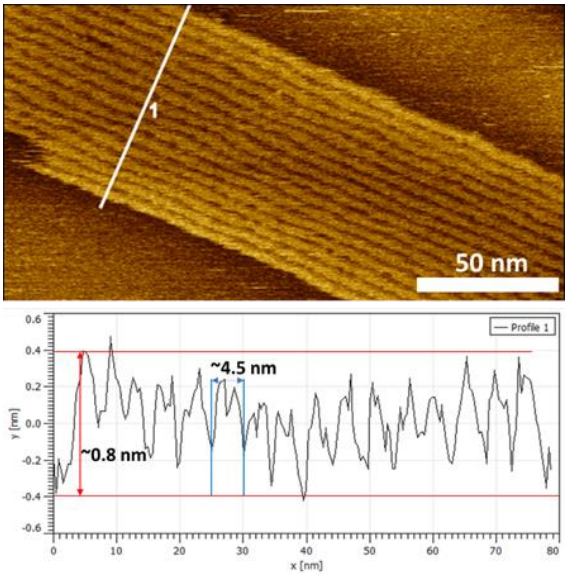

Figure 3.2. High-resolution AFM image and height profile of the self-assembled patterns of MoSBP1 on a graphite surface. The 2D island consisted of parallel rows with uniform spacing. The height of the island was ~0.8 nm, and the center-to-center distance of rows was ~4.5 nm.

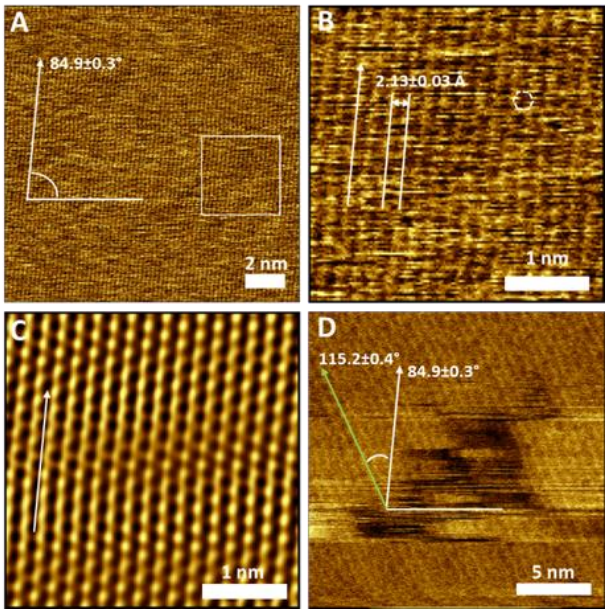

Figure 3.3. The relative direction between peptide rows and graphite lattices. (A) Atomic-resolution AFM image showing the graphite lattice. (B) Digital zoom-in of the region in A denoted by the square. The distance between rows was 2.13 ± 0.03 Å. (C) FFT-filtered image of B. White arrows in A to C lie along the zig-zag direction of the

graphite lattice. (D) High-resolution in situ AFM image of an assembled island of MoSBP1 in one of the dominant directions. Rows lie at an angle of ~30° to the zig-zag direction of graphite, which is the armchair direction. Reprinted with permission from [175]. Copyright 2018, AAAS.

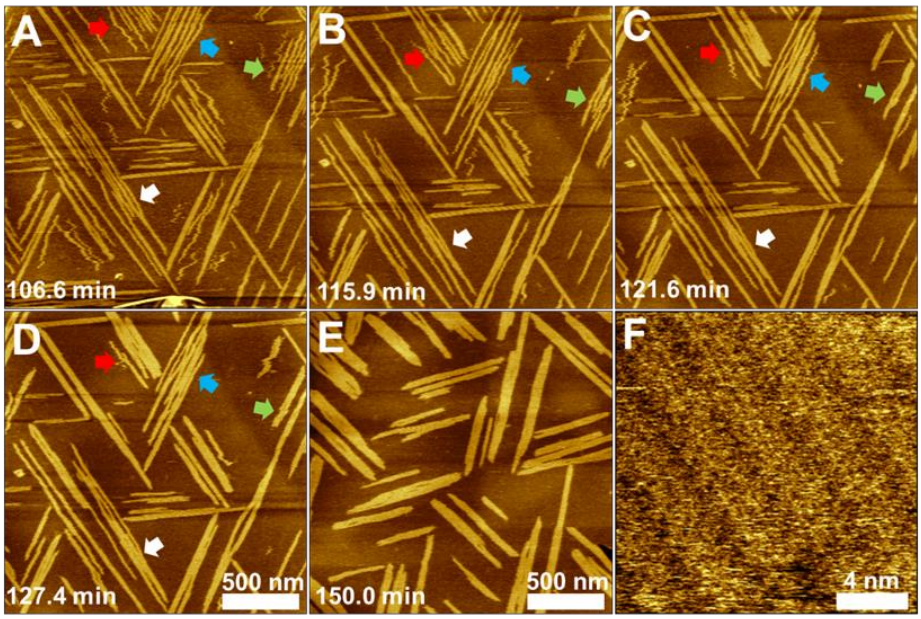

Figure 3.4. In situ AFM images of MoSBP1 (1 µM) on graphite. (A to D) A sequence of images showing rows of MoSBP1 on graphite can diffuse across the surface (see arrows), aggregating with other rows to form immobile islands. (E) Aggregated islands at another location showing the final state of these single rows as constituents of compact 2D islands. (F) High-resolution image showing the highly ordered structure of these islands. Reprinted with permission from [175]. Copyright 2018, AAAS.

3.3.2 *Metastable State*

When the supersaturation of the peptide solution was increased, a metastable state was also observed initially during the assembly process of MoSBP1 on graphite surfaces (Figure 3.5 A). The metastable assembled structures only aligned along three equivalent directions (one set of

directions). The height of these islands was ~0.6 nm, which was slightly smaller than that of the stable structures (Figure 3.5 A). The metastable islands were also highly ordered and consisted of parallel peptide rows with uniform spacing around 3.5 nm (Figure 3.5, A and B).

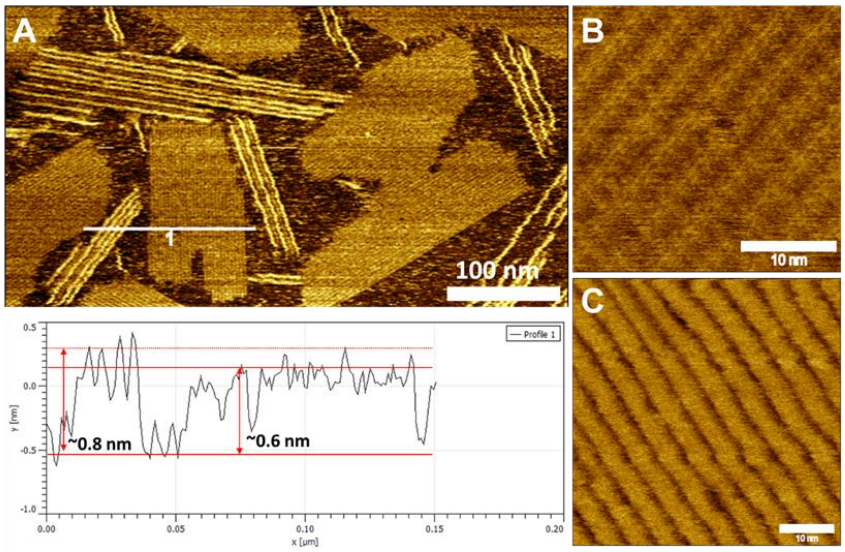

Figure 3.5. Coexistence of two different states on graphite surfaces. (A) AFM image and height profile of the metastable assembled structure. (B) High-resolution AFM image of the metastable assembled structure. (C) High-resolution AFM image of the stable structure.

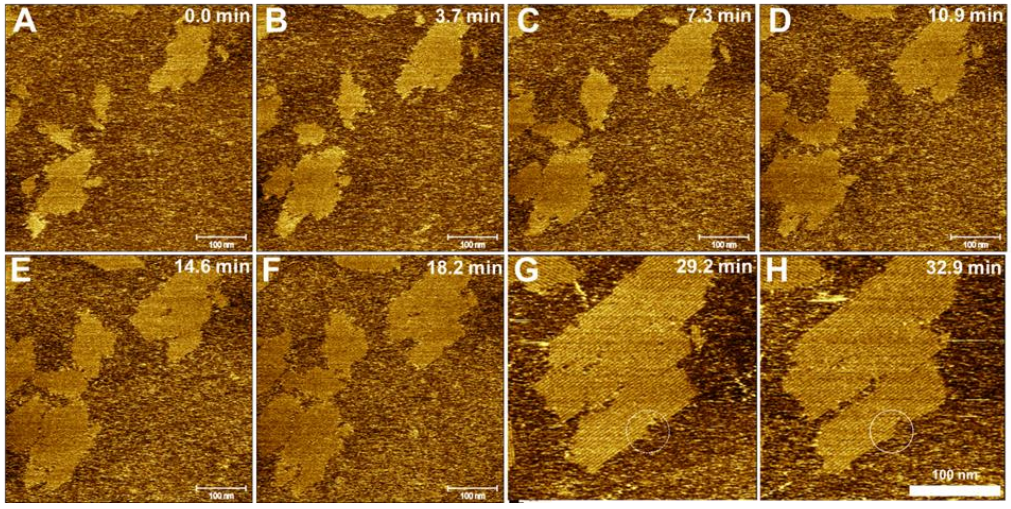

Figure 3.6. Row-by-row growth of the metastable islands on graphite. (A to F) When 4 µM MoSBP1 solution was incubated with a freshly cleaved graphite surface,

metastable islands formed and grew along preferred directions. Scan size: 500 nm. (G and H) High-resolution AFM images showing the creation of a new row to the side of an island.

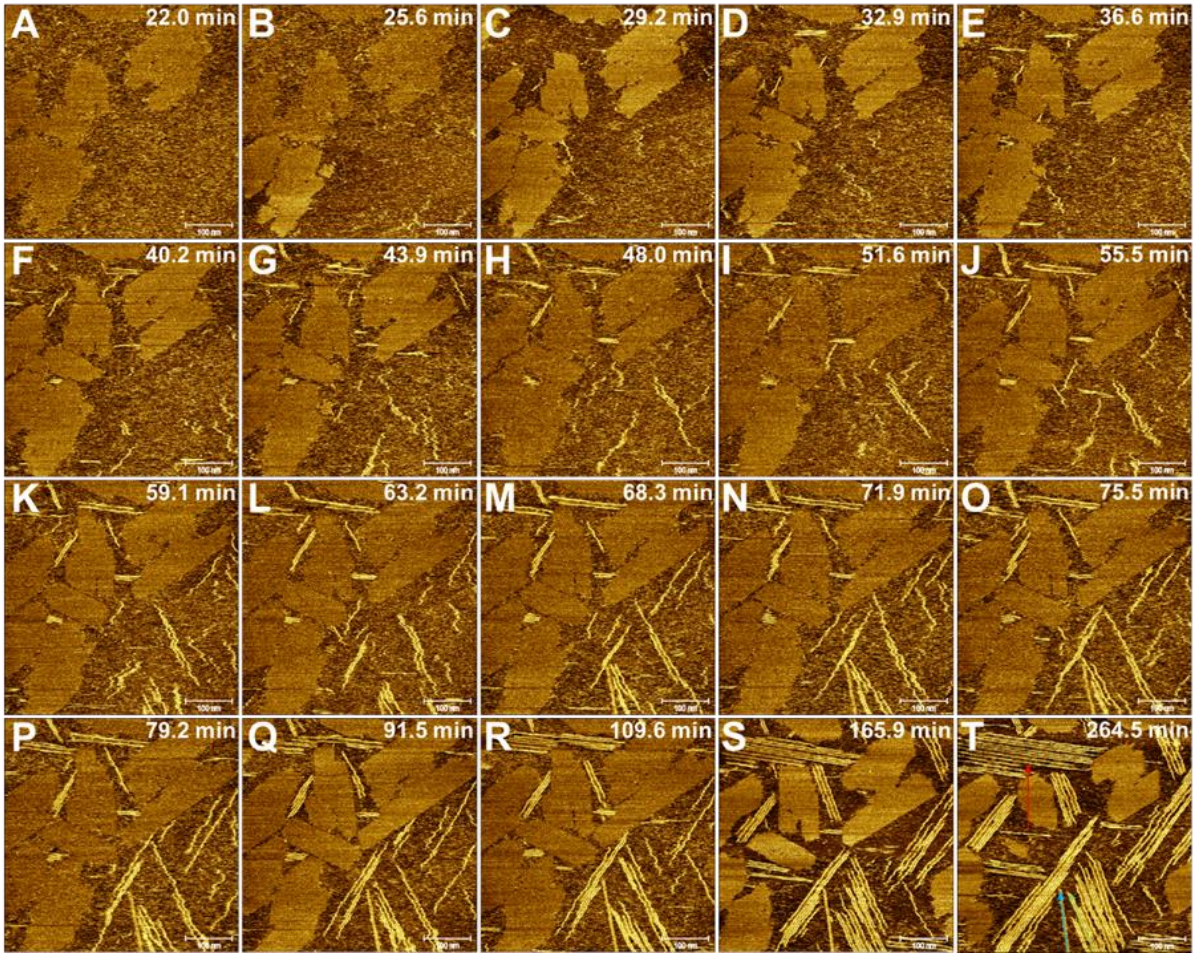

Figure 3.7. Development of the metastable and stable states under 4 μM MoSBP1 on a graphite surface. Metastable islands were created first and then gradually dissolved. Stable structures formed slowly and started to dominate over time. Colored arrows mark different orientations of peptide rows. Scan size: 500 nm.

While the stable structures followed a nucleation-diffusion-aggregation growth mechanism, the metastable islands went through the classical monomer-by-monomer pathway, which was the same as the row-by-row growth mechanism seen on MoS_2 surfaces (Figure 3.6). These islands

were kinetically preferred and formed much faster than the stable structures (Figure 3.7). However, they would gradually dissolve as the stable structure took over, grew, and kept consuming the free monomers in the solution. Moreover, peptide rows that comprised the stable domains had to nucleate on the bare graphite surface; subsequent diffusion and aggregation led to the final stable structures (Figure 3.7). There was no evidence for a direct transformation from the metastable state to the stable state. We also noticed that these two distinct structures preferred to align along different sets of directions and there was a 20.7° difference between these two sets of orientations (Figure 3.7, S and T). While the metastable state only aligned along one set of directions, the stable structure exhibited two sets of directions, one of which was only seen in a minority of the peptide rows (Figure 3.7 T).

3.3.3 *Transition Through a Dissolution-reprecipitation Mechanism*

When we further increased the peptide concentration to 5 μM, metastable islands formed and grew rapidly, fully covering the graphite surface within ~10 min (Figure 3.8). Defects could be found along the boundaries of islands and within the islands. There were some clusters deposited on the islands, but we never observed the formation of a second layer on top of the islands (Figure 3.8).

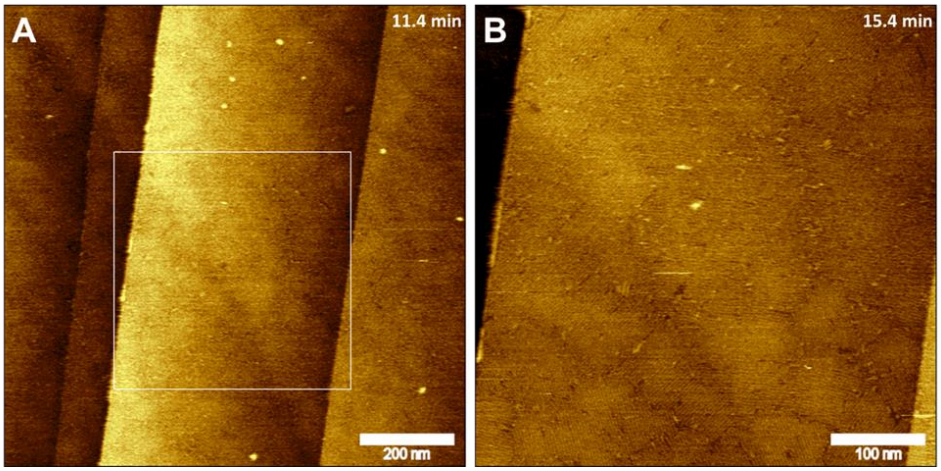

Figure 3.8. In situ AFM images of assembled structures of MoSBP1 (5 μM) at an early time on a graphite surface. (A) The graphite surface was fully covered by a layer of

peptides. (B) High-resolution image of the selected part in A, showing that the surface was covered by ordered domains.

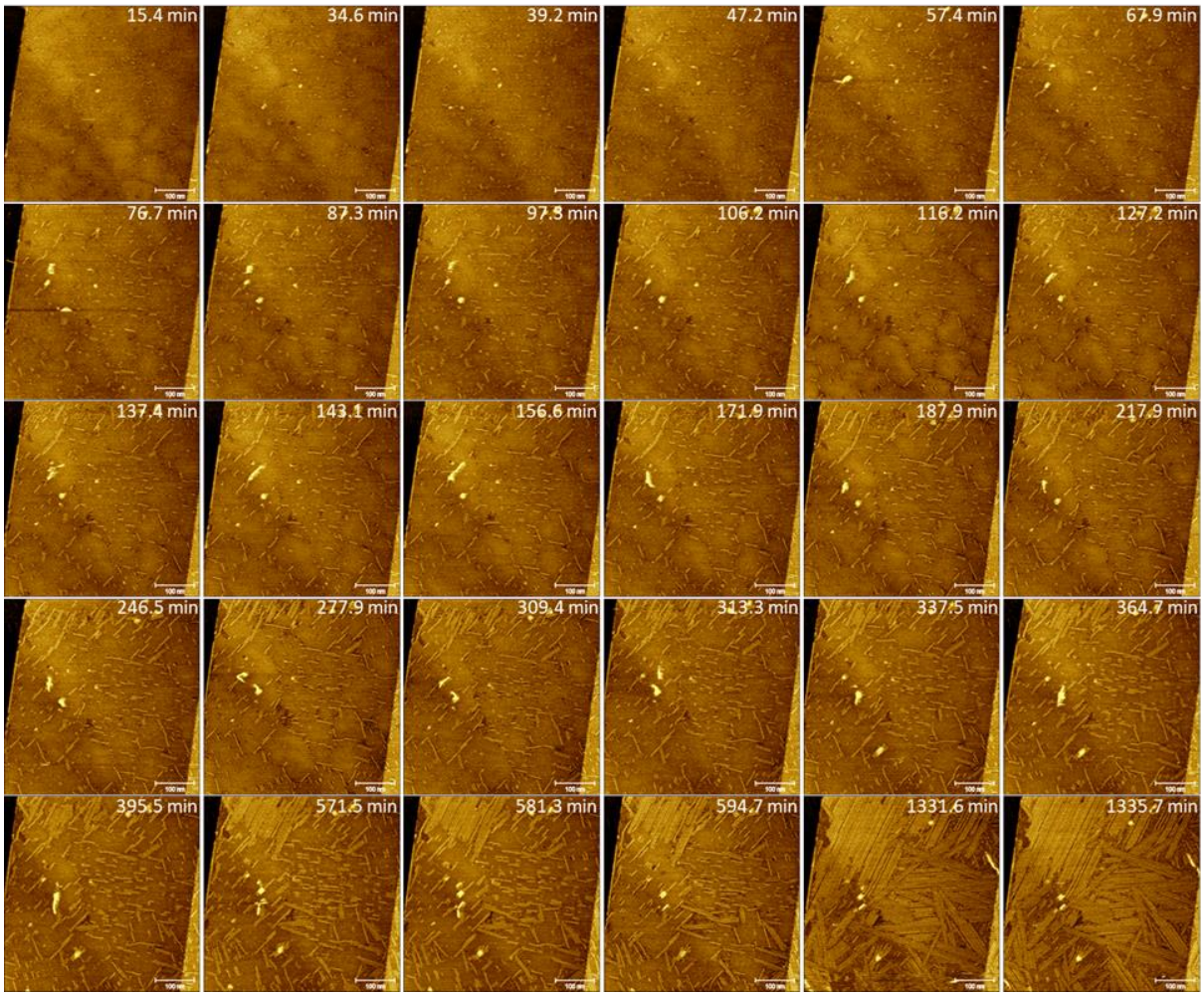

Figure 3.9. Development of assembled structures of MoSBP1 (5 μM) on graphite. Metastable structures covered the surface rapidly, stable structures formed gradually, and started to dominate over time.

By continuously monitoring the assembly process, our results showed that, while the metastable structures rapidly covered the surface, the stable structures formed gradually, but still came to dominate over time (Figure 3.9). We also noticed that the peptide rows comprising the stable domains could not form on top of the metastable structures. They had to nucleate and grow

on the bare graphite surface. Since the surface was almost entirely covered by the metastable islands, stable structures could only nucleate within the gaps between the boundaries of metastable islands or within the defects inside the metastable domains; they then grew as the metastable structures dissolved, which created further available space (Figure 3.10). While peptide rows comprising stable structures could diffuse freely across the surface and explore possible orientations to settle down in a preferred direction under lower peptide concentrations, the rows created within confined spaces at boundaries or defect sites under 5 μM peptide concentration lost their ability to rotate and diffuse. In this case, metastable islands with a high coverage on the surface served as templates to force the stable rows to align along metastable directions (Figure 3.11). Combined with the two possible direction sets for stable islands, the extra direction set templated by metastable islands led to the observed three direction sets for the stable islands in the final state after long incubation times (Figure 3.1).

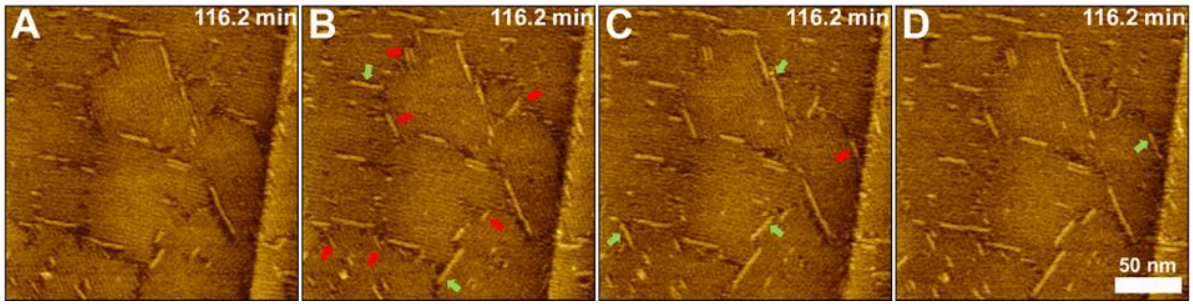

Figure 3.10. Nucleation of peptide rows within the gaps between islands. The red arrow marks the creation of a new row. The green arrow marks the growth of an existing row.

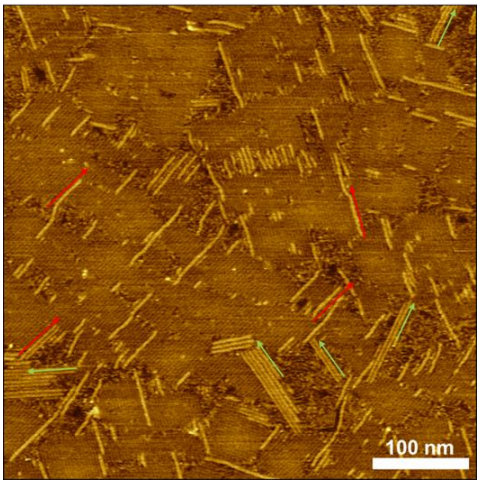

Figure 3.11. Rows comprising the stable structures were sometimes templated to align along the orientations of metastable islands. Stable rows created at larger gaps could rotate and align along preferred directions (marked with green arrows). Stable rows that formed at the boundaries or defect sites were forced to align along the directions of metastable islands.

3.4 CONCLUSIONS

In this study, we explored the assembly process of MoSBP1 on graphite surfaces. Two distinct ordered states coexisted at high peptide supersaturation. Our results show that the kinetically preferred metastable state can only form at high peptide supersaturation in the solution. It is kinetically preferred and assembles rapidly on graphite following a row-by-row growth pathway. The thermodynamically stable state forms more slowly through a nucleation-diffusion-aggregation mechanism and gradually dominates the surface over time. The metastable state dissolves as the stable one grows and serves as a reservoir of peptide monomers. There is no direct transition from a metastable state to a stable state; thus, the development of assembled peptide arrays on graphite surfaces demonstrates a perfect example of the dissolution-reprecipitation growth mechanism for a 2D crystalline system (Figure 3.12). Our study here revealed the growth pathways and phase

transformation mechanism of two distinct peptide-assembled structures on graphite surfaces, which can be used to guide and interpret different biomolecular self-assemblies at solid-liquid interfaces.

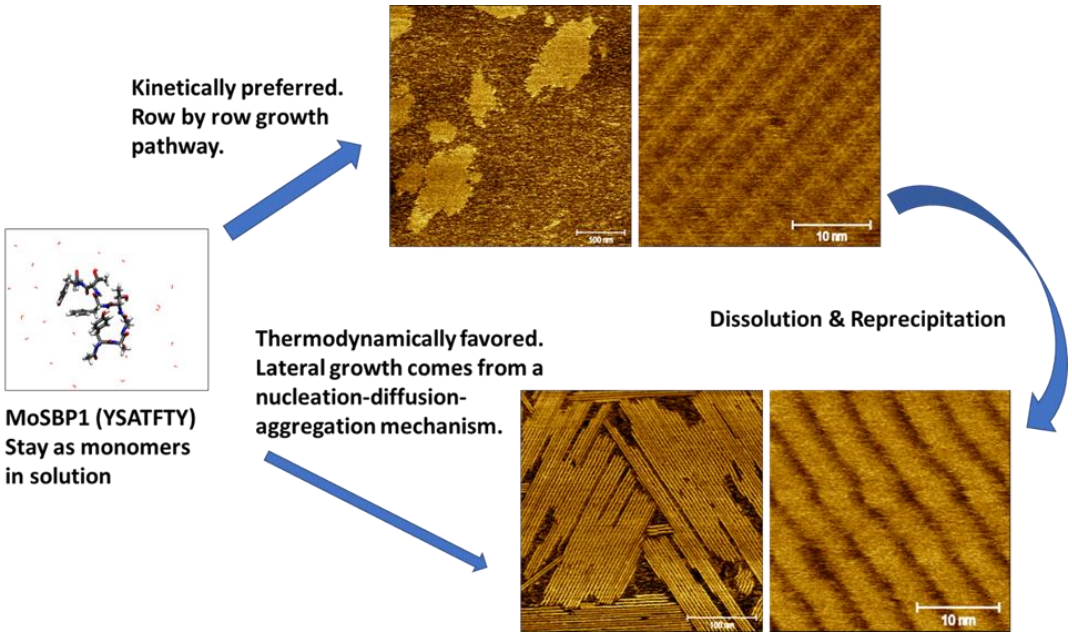

Figure 3.12. Behaviors of MoSBP1 and pattern development on graphite surfaces.

However, there are still some unknown but interesting parts that require further exploration. First, the conformations of MoSBP1 in these states are not yet understood. It will be helpful if we can figure out the structural change of the peptide building block that leads to the different assembled structures with different growth mechanisms. Second, it is surprising to us that the thermodynamically favored structure is more mobile than the metastable one. Finally, it is also important to understand the interactions that lead to the direction preferences for these two distinct peptide arrays. Understanding the driving forces behind these phenomena will provide us insights into the biomolecular self-assembly at the solid-liquid interface.

Chapter 4. SELF-ASSEMBLY OF DESIGNED PEPTOIDS ON MoS_2

4.1 INTRODUCTION

Peptoids are biocompatible materials with similar backbones to peptides; however, they exhibit much higher chemical and thermal stabilities than peptides and proteins [101]. Moreover, peptoid-peptoid and peptoid-surface interactions can be conveniently controlled by the side chain chemistry during self-assembly processes due to the lack of hydrogen bonding from backbones [89-91]. The broad side chain diversity also provides a wide range of functionalizations of the peptoids while maintaining the assembling behavior nearly unchanged and producing similar hierarchically assembled structures [102,105,106]. In our study, we replaced our selected peptides with rationally designed peptoids to pattern the MoS_2 surface in order to achieve assembled arrays with better chemical and thermal stability. A long sequence was found to form a uniform monolayer that fully covered the MoS_2 surface with self-healing capability. In another design, a short sequence assembled into row-by-row structures on MoS_2 surfaces, which could perfectly mimic the behaviors of the original peptide (MoSBP1). The assembly of peptoids into robust structures on MoS_2 surfaces provides the possibility to functionalize the semiconducting substrate for future applications.

4.2 METHODS

4.2.1 *Synthesis of Peptoid*

The peptoids were synthesized using a modified solid-phase submonomer synthesis method, as described in Jin et al.'s work [106]. They were either synthesized using a commercial Aapptec Apex 396 robotic synthesizer or synthesized manually in a 6-mL plastic vial. Peptoids were

cleaved from the resin by the addition of 95% trifluoroacetic acid in water and then dissolved in water and acetonitrile solution (*v*/*v* = 1:1) for HPLC purification.

4.2.2 *Preparation of Peptoid Solution*

Lyophilized and HPLC-grade peptoids were dissolved in pure water with the help of sodium chloride. The final concentration of the peptoid solution is 2mM, with a pH value of ~12.

4.2.3 *In situ AFM Characterization*

The AFM characterization was done with a Cypher ES AFM (Asylum Research). A freshly cleaved MoS_2 bulk crystal surface (3 mm × 3 mm; Manchester Nanomaterials, UK) on top of a metal disc was set inside the AFM chamber. 40 μL of peptoid solution was added onto the MoS_2 surface and incubated at room temperature. In situ images were captured using silicon nitride probes (OTR4 and OTR8, k: 0.08 N/m, 0.15 N/m, tip radius: 15 nm; Bruker) under tapping mode. Images were processed and analyzed using Gwyddion SPM data analysis software.

4.2.4 *Ex situ AFM Imaging*

40 μL peptoid solution was incubated on a MoS_2 surface in a sealed chamber. After incubation, the droplet was wiped with filter paper and the MoS_2 surface was washed with DI water. Then the substrate was gently dried with N_2 flow. Images were captured using silicon probes (RTESPA-300, k: 40 N/m, tip radius: 8 nm; Bruker) under tapping mode with a Cypher ES AFM (Asylum Research) and a Nanoscope VIII (Bruker) at room temperature. Images were analyzed using Nanoscope Analysis v1.5 (Bruker) and Gwyddion SPM data analysis software.

4.3 RESULTS AND DISCUSSIONS

With the fundamental understanding of the assembly mechanisms of peptides on MoS_2, we are trying to increase the stability of the assembled structure for further functionalization and future application. A straightforward approach is replacing peptides with peptoids which have similar backbones with peptides. Based on the previous structural study, we designed several peptoid sequences, two of which gave excellent results. One long sequence formed continuous monolayer films with self-healing capability on MoS_2 surfaces, and a short sequence assembled into ordered row-by-row structures on MoS_2 surfaces, which closely mimicked the behavior of the original peptide (MoSBP1).

4.3.1 *Continuous Monolayer Film on MoS_2*

From our previous study [175], we noticed that phenyl groups played an essential role in the binding affinity of MoSBP1 to MoS_2 substrates, as well as in controlling the ordered assembly.

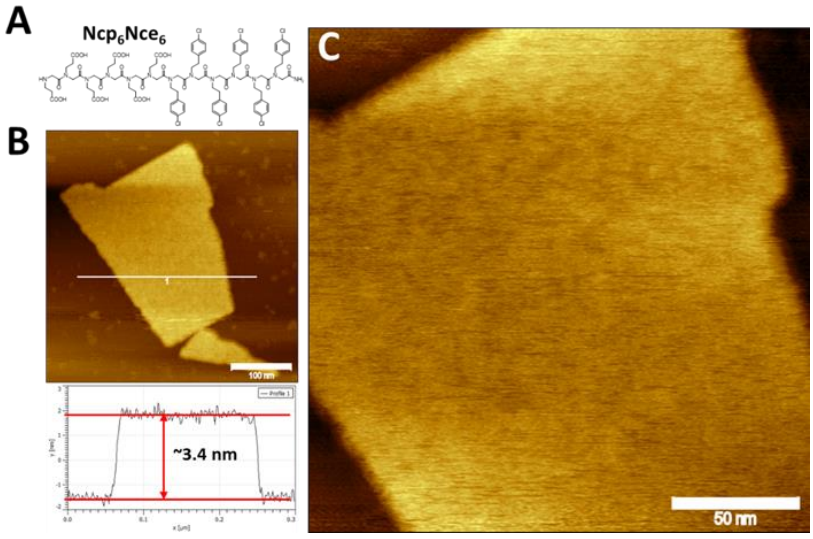

Figure 4.1. Self-assembly of lipid-like peptoid into highly stable 2D nanosheets. (A) Structure of Ncp_6Nce_6. (B) AFM image and height profile of self-assembled nanosheets deposited on a MoS_2 surface. (C) High-resolution AFM image of the self-assembled nanosheets.

The first successful peptoid sequence was Ncp_6Nce_6 (Figure 4.1 A), which has been shown to assemble into free-standing, membrane-like 2D nanosheets in bulk solution (Figure 4.1, B and C) [106,107]. It possesses a phenyl group-rich domain which we hypothesized would provide adequate binding affinity to the hydrophobic MoS_2 surface. Thus, we tested the assembly of Ncp_6Nce_6 on MoS_2 surfaces.

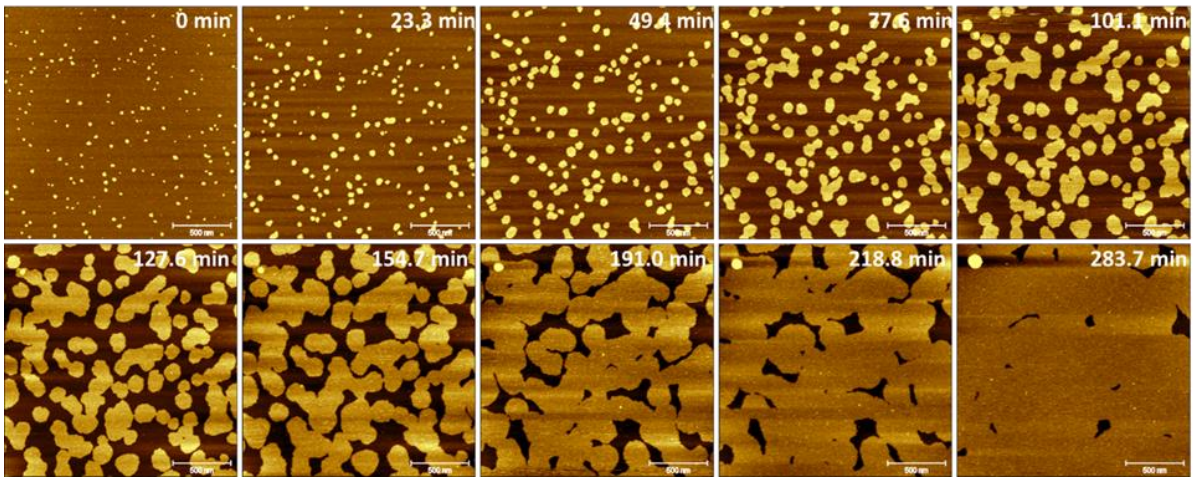

Figure 4.2. Development of continuous films of Ncp_6Nce_6 on a MoS_2 surface. Scan size: 2 μm.

Our result showed that these peptoids assembled into a continuous film that could cover the whole MoS_2 surface (Figure 4.2). When incubated with freshly cleaved MoS_2 surfaces, these peptoids nucleated and grew into 2D islands with irregular shapes without directional preferences. These islands gradually expanded in size and merged with nearby islands as they grew. No boundaries were observed after merging and gaps between islands could be filled. In other words, they exhibited the self-healing capability and lipid-like properties (Figure 4.2 and Figure 4.3) reported earlier for these same peptoids assembled on mica [107]. No order was observed on the surfaces of the assembled islands, which did not exhibit a row-by-row structure (Figure 4.4 A) reported in previous TEM-based studies [106,107]. The height of these islands was ~2.3 nm

(Figure 4.4 B), indicating that they comprised monolayer-thick films with peptoids standing on the substrate [107]. The aromatic domain was hidden towards the MoS_2 surface and the hydrophilic tail was exposed to the bulk solution (Figure 4.4 C). The assembled structure was mainly stabilized by the π-π interactions between peptoid molecules.

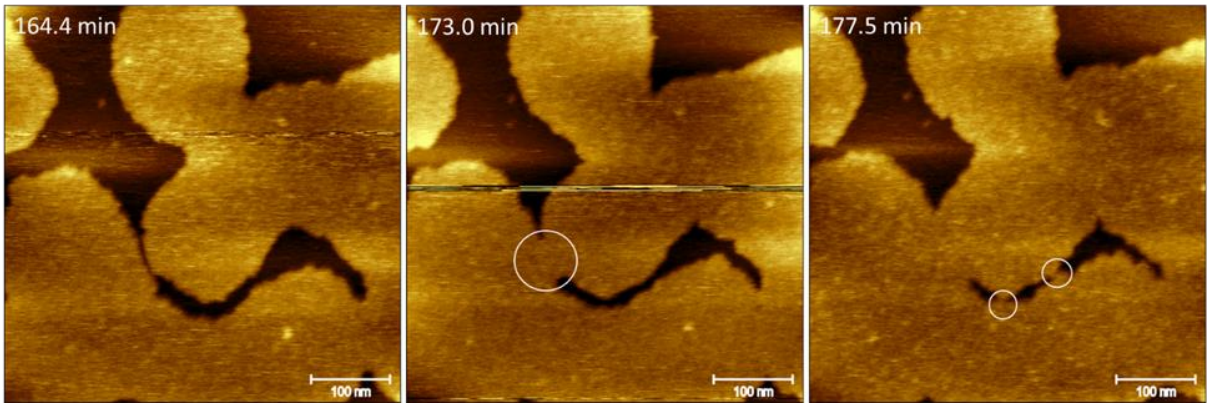

Figure 4.3. Merging of individual islands and the self-healing of the gaps. Circles highlight the necking between islands. Scan size: 500 nm.

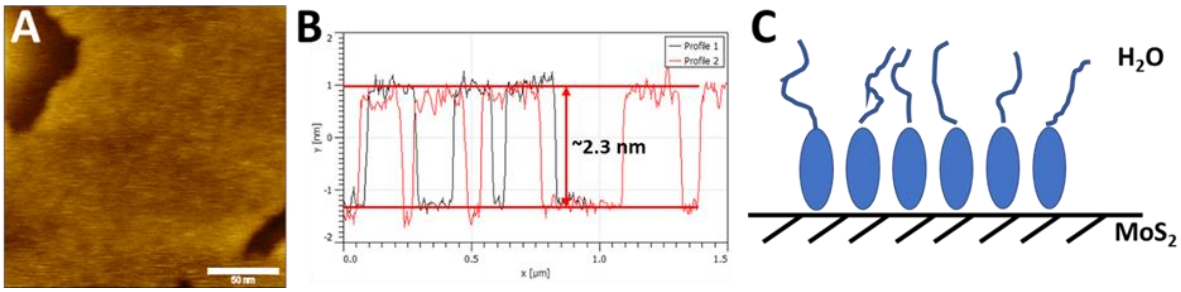

Figure 4.4. (A) High-resolution AFM image of an assembled film on MoS_2. (B) Height profile of assembled domains on MoS_2. The height of these islands was ~2.3 nm. (C) Schematic model of the assembled islands. Peptoids had their hydrophobic parts buried and exposed their long hydrophilic tail towards the bulk solution.

The self-healing capability of the assembled film on MoS_2 provides us the possibility to pattern the substrate with different peptoid components, which maintain similar structural features but have distinct functional groups. Such an assembling system on a semiconducting substrate can

serve as a robust platform to combine different functional components together with precise control and may find wide applications in biosensing and bionanotechnology.

4.3.2 *Row-by-row Structure on MoS_2*

A short peptoid sequence, $NBrpe_6Dig$, was also designed with six phenyl groups and a short hydrophilic part (Figure 4.5 A). The strong π-π interactions between peptoid molecules led to the formation of membrane-like 2D nanosheets in bulk solution (Figure 4.5 B). However, they assembled into a completely different, highly ordered structure on MoS_2 surfaces.

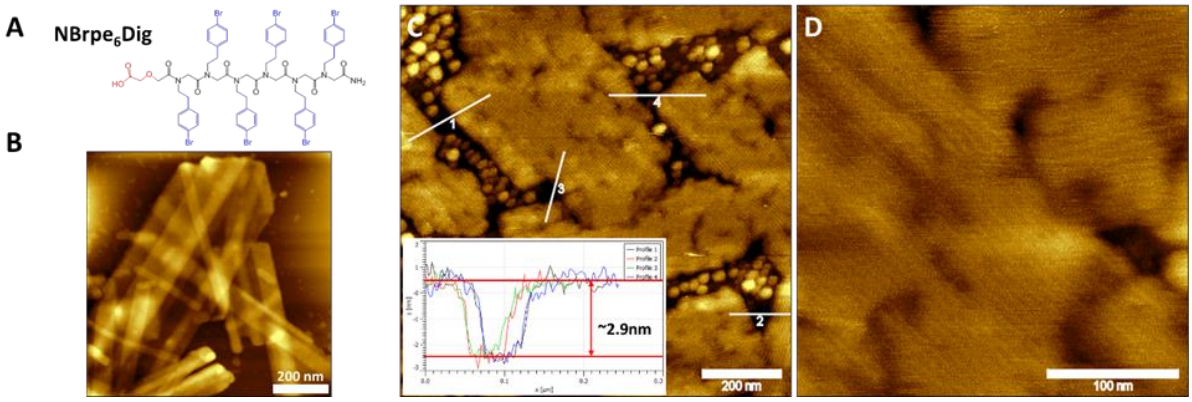

Figure 4.5. Self-assembly of $NBrpe_6Dig$ peptoid molecules in bulk solution and on MoS_2 surfaces. (A) Structure of $NBrpe_6Dig$. (B) AFM image showing the assembled 2D nanosheets in bulk solution deposited on a mica surface. (C) AFM image and height profile of self-assembled islands on a MoS_2 surface. (C) High-resolution AFM image showing that the islands consisted of parallel rows.

When incubated with freshly cleaved MoS_2 surfaces, $NBrpe_6Dig$ formed elongated islands along three equivalent lattice directions of MoS_2 lattices (Figure 4.5, C and D). The height of these islands was ~2.9 nm. Each island consisted of parallel peptoid rows with a center-to-center distance of ~7.4 nm. The boundaries between islands were conspicuous since islands had different orientations. This observation was different from the case of Ncp_6Nce_6, where boundaries

completely disappeared after the merging of two islands. The behavior of $NBrpe_6Dig$ on MoS_2 surfaces closely mimicked that of the original peptide, MoSBP1, except that the height of the peptoid islands was much greater than that of MoSBP1 islands (2.9 nm vs. 0.7 nm). Besides, width of the peptoid rows (~7.4 nm) is much larger than the width of one standing peptoid molecule. However, based on the current resolution of the assembled structures, we cannot reveal their detailed structures and determine their smallest building units. There is a large possibility that each of these observed peptoid rows are actually assembled nanoribbons, which then aligned together into ordered domains, following a similar development process described in previous nanotube formation study [105]. But it is a 2D version that develop into films instead of nanotubes. Anyway, in situ study and high-resolution imaging are required in order to reveal the assembly pathway and the assembled structure.

4.4 CONCLUSIONS

In our study, we have successfully designed two peptoid sequences that can assemble and pattern the MoS_2 surface. The long sequence, Ncp_6Nce_6, can form a continuous monolayer which fully covers the MoS_2 surface with self-healing capability. The short sequence, $NBrpe_6Dig$, assemble into directional islands which consist of parallel peptoid rows. The development of these stable structures on MoS_2 surfaces provides the possibility to pattern 2D material surfaces with precise control, which can lead to a broad range of potential applications in drug delivery, biosensing, and biomimicry.

Chapter 5. SELF-ASSEMBLY OF COMPUTATIONALLY DESIGNED PROTEINS

We have used the capability of in situ AFM to study the kinetics and mechanisms of other types of self-assembling systems. For example, we used in situ AFM to follow the assembly of computationally designed proteins into helical filaments and revealed the cap-induced dissolution of the filaments [116]. In another case, two complementary proteins were designed to co-assemble into highly ordered honeycomb arrays. We analyzed the distribution of edge sites and, from that, determined the rate-determining step in the assembly process.

5.1 Self-assembly of 1D Helical Filaments

DHF119 proteins were computationally designed to assemble into micrometer-scale filaments from monomeric protein building units [116]. The reconstructed structures of two primary intermonomer interfaces in the filament from high-resolution cryo-EM images showed that they were very close to the computationally designed model (Figure 5.1).

In our study, we followed the assembly process of designed proteins into helical filaments using in situ AFM and found that the growth rate of DHF119 protein fibers changed linearly with monomer concentration (Figure 5.2, A and E). To determine whether fiber dissolution can also be tuned by designed accessory proteins, monomeric capping units lacking one of the two designed interfaces in the DHF119 fibers were designed. These caps are expected to attach to only one end of the fiber, but not the other, preventing further elongation. Since the two ends of the fibers are distinct, there are two types of caps, named N-cap and C-cap. The addition of increasing concentrations of the capping units to already assembled filaments resulted in shrinking and

eventual disappearance of the filaments, suggesting that the assembly process is highly dynamic and reversible.

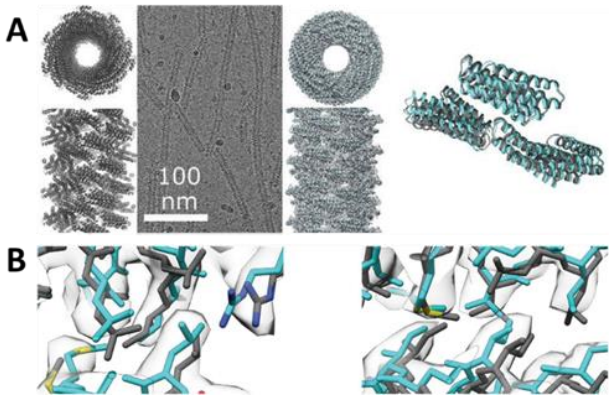

Figure 5.1. Cryo-EM structural determination of the assembly of DHF119 proteins. (A) (Left to right) Computational model, representative filaments in cryo-EM micrographs, cryo-EM structure, and overlay between the model and structure for DHF119 filaments. (B) Close-up views of the two main intermonomer interfaces in the filament for DHF119, with the computational model (gray) and cryo-EM structure (cyan) in sticks in the helical reconstruction density (3.4-Å resolution). The high-resolution structure of DHF119 is very close to the design model. Reprinted with permission from [116]. Copyright 2018, AAAS.

Monitoring of cap-induced disassembly showed that fibers incubated with single end caps disassembled primarily from one end, presumably the uncapped end, while in the presence of both caps, disassembly occurred from both ends (Figure 5.2, B to D). Interestingly, these two ends dissolved asymmetrically with the presence of the same concentration of two different capping units (N-cap and C-cap) (Figure 5.2, D and F). These two ends are expected to shrink at similar rates since the designed protein interfaces and interactions at these two ends should be the same. However, the solvation effects at these two ends should be different, which may lead to the observed difference in dissolution rates at different ends.

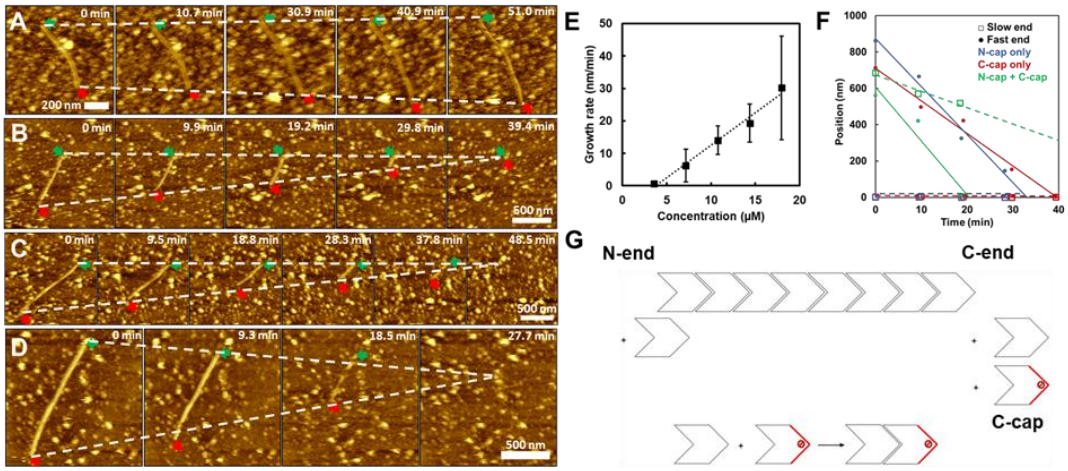

Figure 5.2. Growth and dissolution of DHF119 filaments. (A) In situ AFM images showing the growth process of filaments with 7.2 μM DHF119. (B) In situ AFM images showing the dissolution of filaments (3.8 μM) from one end in the presence of N-caps (3.8 μM). (C) In situ AFM images showing the dissolution of filaments (3.8 μM) from one end in the presence of C-caps (3.8 μM). (D) In situ AFM images showing the dissolution of filaments (3.8 μM) from both ends in the presence of N-caps (1.9 μM) and C-caps (1.9 μM). (E) Measurements of growth rates of DHF119 filaments at different concentrations shows that the growth rate changes linearly with protein concentration. (F) Positions of fiber ends vs. time in solutions with N-caps, C-caps, and N-caps + C-caps, respectively. In all cases, the DHF119 monomer concentration and the total cap concentration are each 3.8 μM (at this concentration of monomer, fibers neither dissolve nor grow in the absence of caps). Because they lack one of the filament interfaces, caps can only bind to one end; disassembly from this end will be slower as the combined on-rate of caps and monomers is greater than the on-rate of monomers alone at the other end. (G) A simplified model for disassembly. At the C-end, both monomers and caps bind to the fiber while at the N-end, only monomers can be incorporated. Caps complex with monomers in solution effectively reducing the free monomer concentration that can bind to the N-end. Reprinted with permission from [116]. Copyright 2018, AAAS.

The observed cap-induced dissolution behavior can be understood as follows. At the critical monomer concentration where fibers neither grow nor shrink, the (concentration dependent) rate

of monomer addition to the ends is balanced by the (concentration independent) disassociation rate. Caps perturb this balance by complexing with monomers in solution (Figure 5.2 G) effectively reducing the free monomer concentration, hence when both N-caps and C-caps are present, disassembly wins out over growth, leading to a net shrinking of the filaments from both ends. When one cap is present, C-cap for example, the net rate of subunit addition is greater at the C-end where both free monomers and free C-caps can add (Figure 5.2 G) than at the N-end where only free monomers can add (Figure 5.2 G). Since the rate of monomer dissociation is the same at both ends, the fibers shrink primarily from one end (the uncapped end) as observed.

Our study here provides us the insight into the growth and dissolution mechanisms of the protein filaments. Combining the study here [116] and the pH-driven conformational changes reported in Boyken et al.'s work [141], pH-responsive protein filaments have been designed. It will be interesting to study their dynamic response during pH changes and explore their applications.

5.2 Self-assembly of 2D Honeycomb Arrays

In another computationally designed protein system, two complementary proteins (one with three-fold symmetry, named A-unit; the other with two-fold symmetry, named B-unit) can organize into a two-dimensional honeycomb lattice in bulk solution (Figure 5.3, A and B). To determine whether the rate-determining step in growth is initiation or completion of hexagonal units, we analyzed the numbers of each of the possible edge states in a set of AFM images. The results showed that A-units bonded with two B-units —designated as A-II sites — comprised the most stable edge states (Figure 5.3 C). While A-units with just one neighboring B-unit — designated as A-I sites — were the least stable, occurring far less often than exposed B-units (B-I sites) (Figure 5.3 C). The results imply that the attachment of a B-unit to an A-I site to create a stable A-II site is the rate-determining

step during assembly. Assuming the observed percentages of occurrence p(i) represent an equilibrium distribution, we can estimate the relative free energies ΔG(i-j) of any two sites from p(i)/p(j) = exp[-(ΔG(i-j))/kT], from which we obtain ΔG(A-II – A-I) = -6.2 kJ/mol, ΔG(B-I – A-I) = -5.4 kJ/mol, and ΔG(A-II - B) = -0.9 kJ/mol.

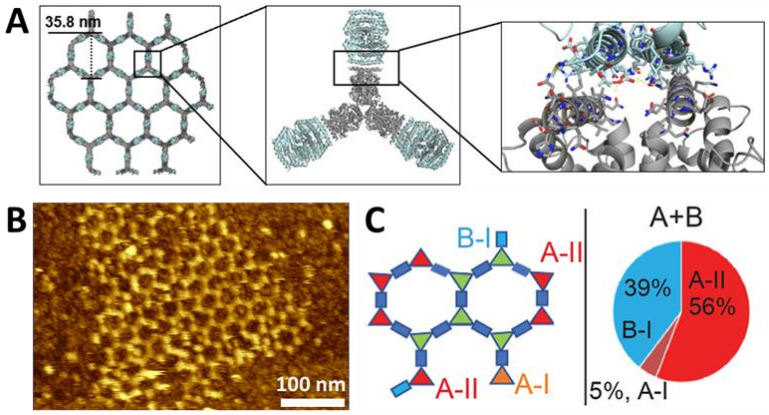

Figure 5.3. Design and analysis of the self-assembled 2D honeycomb arrays. (A) Designs of the two complementary proteins that co-assemble into highly ordered honeycomb lattices. (B) In situ AFM of the self-assembled protein arrays. (C) Statistics of lattice edge states.

The growth and healing process of such assembled lattice were also observed using in situ AFM. Cracked edges were reformed and point defects or vacancies in the interior part of the lattice were filled over time. However, interaction between AFM probe and sample needs to be precisely controlled. The honeycomb structures can be easily destructed or removed from of the surface during the scanning process of the AFM probe.

Recently, several new designs have been made to anchor these proteins and arrays to lipid bilayer surfaces. The advantage of using lipid bilayers as substrates for this assembly system in AFM study is that protein components can possess a strong binding affinity to the surface while maintaining the mobility required to generate organized structures. This approach may allow us to

further study their growth behaviors and kinetics with in situ AFM, which can provide us a better understanding of their assembly processes and guide future designs of assembling systems in bulk solution and at interfaces.

Chapter 6. CLOSING REMARKS AND CONCLUTIONS

Using phage selected peptides, controllable assembly of hierarchical architectures was achieved on MoS_2 surfaces. In situ AFM revealed a row-by-row growth mechanism of the 2D arrays and the results highlighted the importance of dimensionality on nucleation and growth. Assembly of these peptides on HOPG surfaces showed a transition from metastable to stable state and another possible row-by-row pathway for the development of 2D structure, like an "oriented attachment" process in two dimensions. Rational designed peptoids were also used to mimic the behaviors of the original peptide. These studies demonstrated that numerous factors played essential roles in determining both pathways and final outcomes of assembly. Based on the developed approaches, the assembly and disassembly of de novo designed proteins were also investigated. These systems explored here share similar features with many other self-assembling systems. The above studies place these systems in the context of well-developed theories for the emergence of order and post nucleation growth and provide a guide for interpreting and controlling their assembly.

However, despite the progresses we have made, further efforts are still required to reach the stage where precise engineering of biomolecules and controllable assembly into desired phases and structures is feasible. We still know little about the interplay of intermolecular interactions and the energy landscapes across which hierarchical assembly develops. Moreover, it is still difficult to predict intermediate states that will merge prior to the final ordered state. Additionally, it is still challenging to design systems with multi-well potentials for out-of-equilibrium switching in response to external stimuli. With further insights in these areas, biomolecular self-assembly may find promising applications in tissue engineering, biosensing, drug delivery, diagnosis, catalysis, biomineralization, electronic nanodevices, energy storage and harvesting, and environmental remediation.

BIBLIOGRAPHY

[1] L. Wang, C. Gong, X. Yuan, G. Wei, *Nanomaterials* **2019**, *9*, 285.

[2] S. Gwo, H.-Y. Chen, M.-H. Lin, L. Sun, X. Li, *Chem. Soc. Rev.* **2016**, *45*, 5672.

[3] L. Wang, Y. Sun, Z. Li, A. Wu, G. Wei, *Materials* **2016**, *9*, 53.

[4] M. A. Boles, M. Engel, D. V. Talapin, *Chem. Rev.* **2016**, *116*, 11220.

[5] A. Dong, J. Chen, P. M. Vora, J. M. Kikkawa, C. B. Murray, *Nature* **2010**, *466*, 474.

[6] X. Ye, J. Chen, M. Engel, J. A. Millan, W. Li, L. Qi, G. Xing, J. E. Collins, C. R. Kagan, J. Li, S. C. Glotzer, C. B. Murray, *Nat. Chem.* **2013**, *5*, 466.

[7] T. Paik, C. B. Murray, *Nano Lett.* **2013**, *13*, 2952.

[8] J. Duan, Y. Li, Y. Pan, N. Behera, W. Jin, *Coord. Chem. Rev.* **2019**, *395*, 25.

[9] M. Zhao, Y. Huang, Y. Peng, Z. Huang, Q. Ma, H. Zhang, *Chem. Soc. Rev.* **2018**, *47*, 6267.

[10] U. Schlickum, R. Decker, F. Klappenberger, G. Zoppellaro, S. Klyatskaya, M. Ruben, I. Silanes, A. Arnau, K. Kern, H. Brune, J. V. Barth, *Nano Lett.* **2007**, *7*, 3813.

[11] A. Dmitriev, H. Spillmann, N. Lin, J. V. Barth, K. Kern, *Angew. Chem., Int. Ed.* **2003**, *42*, 2670.

[12] S. Stepanow, M. Lingenfelder, A. Dmitriev, H. Spillmann, E. Delvigne, N. Lin, X. Deng, C. Cai, J. V. Barth, K. Kern, *Nat. Mater.* **2004**, *3*, 229.

[13] C. Lin, Y. Liu, H. Yan, *Biochemistry* **2009**, *48*, 1663.

[14] C. K. McLaughlin, G. D. Hamblin, H. F. Sleiman, *Chem. Soc. Rev.* **2011**, *40*, 5647.

[15] G. Wei, Z. Su, N. P. Reynolds, P. Arosio, I. W. Hamley, E. Gazit, R. Mezzenga, *Chem. Soc. Rev.* **2017**, *46*, 4661.

[16] W. Zhang, X. Yu, Y. Li, Z. Su, K. D. Jandt, G. Wei, *Prog. Polym. Sci.* **2018**, *80*, 94.

[17] D. T. Yucesoy, D. Khatayevich, C. Tamerler, M. Sarikaya, *Med. Devices Sens.* **2020**, e10065.

[18] A. Battigelli, *Biopolymers* **2019**, *110*, e23265.

[19] Y. Bai, Q. Luo, J. Liu, *Chem. Soc. Rev.* **2016**, *45*, 2756.

[20] J. D. Perlmutter, M. F. Hagan, *Annu. Rev. Phys. Chem.* **2015**, *66*, 217.

[21] H. Wang, Z. Feng, Y. Wang, R. Zhou, Z. Yang, B. Xu, *J. Am. Chem. Soc.* **2016**, *138*, 16046.

[22] X. Zhang, C. Gong, O. U. Akakuru, Z. Su, A. Wu, G. Wei, *Chem. Soc. Rev.* **2019**, *48*, 5564.

[23] N. Stephanopoulos, J. H. Ortony, S. I. Stupp, *Acta Mater.* **2013**, *61*, 912.

[24] X. Hu, M. Liao, H. Gong, L. Zhang, H. Cox, T. A. Waigh, J. R. Lu, *Curr. Opin. Colloid Interface Sci.* **2020**, *45*, 1.

[25] G. Zhu, R. Hu, Z. Zhao, Z. Chen, X. Zhang, W. Tan, *J. Am. Chem. Soc.* **2013**, *135*, 16438.

[26] B. Liu, Y. Cao, Z. Huang, Y. Duan, S. Che, *Adv. Mater.* **2015**, *27*, 479.

[27] M. Mauro, A. Aliprandi, D. Septiadi, N. S. Kehr, L. De Cola, *Chem. Soc. Rev.* **2014**, *43*, 4144.

[28] L. Wang, Y. Zhang, A. Wu, G. Wei, *Anal. Chim. Acta* **2017**, *985*, 24.

[29] L. Wang, A. Wu, G. Wei, *Analyst* **2018**, *143*, 1526.

[30] N. Nishitani, T. Hirose, K. Matsuda, *Chem. Commun.* **2019**, *55*, 5099.

[31] Q. Li, Y. Jia, L. Dai, Y. Yang, J. Li, *ACS Nano* **2015**, *9*, 2689.

[32] F. Zhang, H.-N. Du, Z.-X. Zhang, L.-N. Ji, H.-T. Li, L. Tang, H.-B. Wang, C.-H. Fan, H.-J. Xu, Y. Zhang, J. Hu, H.-Y. Hu, J.-H. He, *Angew. Chem., Int. Ed.* **2006**, *45*, 3611.

[33] M. A. Elsawy, A. M. Smith, N. Hodson, A. Squires, A. F. Miller, A. Saiani, *Langmuir* **2016**, *32*, 4917.

[34] Y. Li, A. Asadi, M. R. Monroe, E. P. Douglas, *Mater. Sci. Eng., C* **2009**, *29*, 1643.

[35] B. Narayanan, G. H. Gilmer, J. Tao, J. J. De Yoreo, C. V. Ciobanu, *Langmuir* **2014**, *30*, 1343.

[36] Y. Suzuki, G. Cardone, D. Restrepo, P. D. Zavattieri, T. S. Baker, F. A. Tezcan, *Nature* **2016**, *533*, 369.

[37] J. Zhang, Y. Liu, Y. Ke, H. Yan, *Nano Lett.* **2006**, *6*, 248.

[38] A. D. Merg, J. C. Boatz, A. Mandal, G. Zhao, S. Mokashi-Punekar, C. Liu, X. Wang, P. Zhang, P. C. A. van der Wel, N. L. Rosi, *J. Am. Chem. Soc.* **2016**, *138*, 13655.

[39] M. Du, K. Zhou, X. Wang, J. Zhang, Y. Zhang, J. Dong, L. Wu, Z. Qiao, G. Chen, Q. Wang, *Nano Lett.* **2020**, *20*, 1154.

[40] Z. Zhao, Y. Liu, H. Yan, *Org. Biomol. Chem.* **2013**, *11*, 596.

[41] C. Li, J. Adamcik, R. Mezzenga, *Nat. Nanotechnol.* **2012**, *7*, 421.

[42] J. Wang, Z. Ouyang, Z. Ren, J. Li, P. Zhang, G. Wei, Z. Su, *Carbon* **2015**, *89*, 20.

[43] Q. Zhang, M. Li, C. Zhu, G. Nurumbetov, Z. Li, P. Wilson, K. Kempe, D. M. Haddleton, *J. Am. Chem. Soc.* **2015**, *137*, 9344.

[44] Q. Zou, M. Abbas, L. Zhao, S. Li, G. Shen, X. Yan, *J. Am. Chem. Soc.* **2017**, *139*, 1921.

[45] N. C. Seeman, *Nature* **2003**, *421*, 427.

[46] N. C. Seeman, *J. Theor. Biol.* **1982**, *99*, 237.

[47] A. Turberfield, *Phys. World* **2003**, *16*, 43.

[48] C. Lin, Y. Liu, S. Rinker, H. Yan, *ChemPhysChem* **2006**, *7*, 1641.

[49] U. Feldkamp, C. M. Niemeyer, *Angew. Chem., Int. Ed.* **2006**, *45*, 1856.

[50] F. A. Aldaye, A. L. Palmer, H. F. Sleiman, *Science* **2008**, *321*, 1795.

[51] C. Mao, W. Sun, N. C. Seeman, *J. Am. Chem. Soc.* **1999**, *121*, 5437.

[52] D. Liu, M. Wang, Z. Deng, R. Walulu, C. Mao, *J. Am. Chem. Soc.* **2004**, *126*, 2324.

[53] H. Yan, S. H. Park, G. Finkelstein, J. H. Reif, T. H. LaBean, *Science* **2003**, *301*, 1882.

[54] P. W. K. Rothemund, *Nature* **2006**, *440*, 297.

[55] W. M. Shih, J. D. Quispe, G. F. Joyce, *Nature* **2004**, *427*, 618.

[56] S. M. Douglas, J. J. Chou, W. M. Shih, *Proc. Natl. Acad. Sci. U.S.A.* **2007**, *104*, 6644.

[57] X. Zhao, F. Pan, H. Xu, M. Yaseen, H. Shan, C. A. E. Hauser, S. Zhang, J. R. Lu, *Chem. Soc. Rev.* **2010**, *39*, 3480.

[58] S. M. Chin, C. V. Synatschke, S. Liu, R. J. Nap, N. A. Sather, Q. Wang, Z. Álvarez, A. N. Edelbrock, T. Fyrner, L. C. Palmer, I. Szleifer, M. Olvera de la Cruz, S. I. Stupp, *Nat. Commun.* **2018**, *9*, 2395.

[59] S. Zhang, *Nat. Biotechnol.* **2003**, *21*, 1171.

[60] R. Chapman, M. Danial, M. L. Koh, K. A. Jolliffe, S. Perrier, *Chem. Soc. Rev.* **2012**, *41*, 6023.

[61] Y. Zhao, W. Yang, C. Chen, J. Wang, L. Zhang, H. Xu, *Curr. Opin. Colloid Interface Sci.* **2018**, *35*, 112.

[62] F. Chiti, C. M. Dobson, *Annu. Rev. Biochem.* **2006**, *75*, 333.

[63] D. Eisenberg, M. Jucker, *Cell* **2012**, *148*, 1188.

[64] M. R. Chapman, L. S. Robinson, J. S. Pinkner, R. Roth, J. Heuser, M. Hammar, S. Normark, S. J. Hultgren, *Science* **2002**, *295*, 851.

[65] S. K. Maji, M. H. Perrin, M. R. Sawaya, S. Jessberger, K. Vadodaria, R. A. Rissman, P. S. Singru, K. P. R. Nilsson, R. Simon, D. Schubert, D. Eisenberg, J. Rivier, P. Sawchenko, W. Vale, R. Riek, *Science* **2009**, *325*, 328.

[66] J. Li, T. McQuade, A. B. Siemer, J. Napetschnig, K. Moriwaki, Y.-S. Hsiao, E. Damko, D. Moquin, T. Walz, A. McDermott, F. K.-M. Chan, H. Wu, *Cell* **2012**, *150*, 339.

[67] R. Nelson, M. R. Sawaya, M. Balbirnie, A. Ø. Madsen, C. Riekel, R. Grothe, D. Eisenberg, *Nature* **2005**, *435*, 773.

[68] B. Dai, D. Li, W. Xi, F. Luo, X. Zhang, M. Zou, M. Cao, J. Hu, W. Wang, G. Wei, Y. Zhang, C. Liu, *Proc. Natl. Acad. Sci. U.S.A.* **2015**, *112*, 2996.

[69] M. D. Shoulders, R. T. Raines, *Annu. Rev. Biochem.* **2009**, *78*, 929.

[70] T. Jiang, C. Xu, Y. Liu, Z. Liu, J. S. Wall, X. Zuo, T. Lian, K. Salaita, C. Ni, D. Pochan, V. P. Conticello, *J. Am. Chem. Soc.* **2014**, *136*, 4300.

[71] A. D. Merg, G. Touponse, E. van Genderen, X. Zuo, A. Bazrafshan, T. Blum, S. Hughes, K. Salaita, J. P. Abrahams, V. P. Conticello, *Angew. Chem., Int. Ed.* **2019**, *58*, 13507.

[72] K. Tao, A. Levin, L. Adler-Abramovich, E. Gazit, *Chem. Soc. Rev.* **2016**, *45*, 3935.

[73] R. Chapman, K. A. Jolliffe, S. Perrier, *Adv. Mater.* **2013**, *25*, 1170.

[74] H. He, H. Wang, N. Zhou, D. Yang, B. Xu, *Chem. Commun.* **2018**, *54*, 86.

[75] C. R. So, Y. Hayamizu, H. Yazici, C. Gresswell, D. Khatayevich, C. Tamerler, M. Sarikaya, *ACS Nano* **2012**, *6*, 1648.

[76] Z. E. Hughes, T. R. Walsh, *Nanoscale* **2018**, *10*, 302.

[77] D. Khatayevich, C. R. So, Y. Hayamizu, C. Gresswell, M. Sarikaya, *Langmuir* **2012**, *28*, 8589.

[78] Y. Hayamizu, C. R. So, S. Dag, T. S. Page, D. Starkebaum, M. Sarikaya, *Sci. Rep.* **2016**, *6*, 33778.

[79] A. Solomonov, U. Shimanovich, *Isr. J. Chem.* **2019**, ijch. 201900083.

[80] Y.-T. Lai, G. L. Hura, K. N. Dyer, H. Y. H. Tang, J. A. Tainer, T. O. Yeates, *Sci. Adv.* **2016**, *2*, e1501855.

[81] J. B. Bale, S. Gonen, Y. Liu, W. Sheffler, D. Ellis, C. Thomas, D. Cascio, T. O. Yeates, T. Gonen, N. P. King, D. Baker, *Science* **2016**, *353*, 389.

[82] E. Sasaki, D. Böhringer, M. van de Waterbeemd, M. Leibundgut, R. Zschoche, A. J. R. Heck, N. Ban, D. Hilvert, *Nat. Commun.* **2017**, *8*, 14663.

[83] W. M. Park, J. A. Champion, *J. Am. Chem. Soc.* **2014**, *136*, 17906.

[84] J. C. T. Carlson, S. S. Jena, M. Flenniken, T. Chou, R. A. Siegel, C. R. Wagner, *J. Am. Chem. Soc.* **2006**, *128*, 7630.

[85] H. Kitagishi, K. Oohora, H. Yamaguchi, H. Sato, T. Matsuo, A. Harada, T. Hayashi, *J. Am. Chem. Soc.* **2007**, *129*, 10326.

[86] C. Hou, J. Li, L. Zhao, W. Zhang, Q. Luo, Z. Dong, J. Xu, J. Liu, *Angew. Chem., Int. Ed.* **2013**, *52*, 5590.

[87] K. M. Cosert, A. Castro-Forero, R. J. Steidl, R. M. Worden, G. Reguera, *mBio* **2019**, *10*, e02721.

[88] G. Yang, X. Zhang, Z. Kochovski, Y. Zhang, B. Dai, F. Sakai, L. Jiang, Y. Lu, M. Ballauff, X. Li, C. Liu, G. Chen, M. Jiang, *J. Am. Chem. Soc.* **2016**, *138*, 1932.

[89] A. W. P. Fitzpatrick, G. T. Debelouchina, M. J. Bayro, D. K. Clare, M. A. Caporini, V. S. Bajaj, C. P. Jaroniec, L. Wang, V. Ladizhansky, S. A. Muller, C. E. MacPhee, C. A. Waudby, H. R. Mott, A. De Simone, T. P. J. Knowles, H. R. Saibil, M. Vendruscolo, E. V. Orlova, R. G. Griffin, C. M. Dobson, *Proc. Natl. Acad. Sci. U.S.A.* **2013**, *110*, 5468.

[90] E. Tayeb-Fligelman, O. Tabachnikov, A. Moshe, O. Goldshmidt-Tran, M. R. Sawaya, N. Coquelle, J.-P. Colletier, M. Landau, *Science* **2017**, *355*, 831.

[91] P. van Rijn, M. Tutus, C. Kathrein, N. C. Mougin, H. Park, C. Hein, M. P. Schürings, A. Böker, *Adv. Funct. Mater.* **2014**, *24*, 6762.

[92] S. Gonen, F. DiMaio, T. Gonen, D. Baker, *Science* **2015**, *348*, 1365.

[93] V. Liljeström, J. Seitsonen, M. A. Kostiainen, *ACS Nano* **2015**, *9*, 11278.

[94] J. D. Brodin, X. I. Ambroggio, C. Tang, K. N. Parent, T. S. Baker, F. A. Tezcan, *Nat. Chem.* **2012**, *4*, 375.

[95] W. Zhang, Q. Luo, L. Miao, C. Hou, Y. Bai, Z. Dong, J. Xu, J. Liu, *Nanoscale* **2012**, *4*, 5847.

[96] Y. Bai, Q. Luo, W. Zhang, L. Miao, J. Xu, H. Li, J. Liu, *J. Am. Chem. Soc.* **2013**, *135*, 10966.

[97] S. Jones, J. M. Thornton, *Proc. Natl. Acad. Sci. U.S.A.* **1996**, *93*, 13.

[98] Z. Chen, S. E. Boyken, M. Jia, F. Busch, D. Flores-Solis, M. J. Bick, P. Lu, Z. L. VanAernum, A. Sahasrabuddhe, R. A. Langan, S. Bermeo, T. J. Brunette, V. K. Mulligan, L. P. Carter, F. DiMaio, N. G. Sgourakis, V. H. Wysocki, D. Baker, *Nature* **2019**, *565*, 106.

[99] Z. Chen, M. C. Johnson, J. Chen, M. J. Bick, S. E. Boyken, B. Lin, J. J. De Yoreo, J. M. Kollman, D. Baker, F. DiMaio, *J. Am. Chem. Soc.* **2019**, *141*, 8891.

[100] R. Liu, Z. Kochovski, L. Li, Y.-W. Yin, J. Yang, G. Yang, G. Tao, A. Xu, E. Zhang, H.-M. Ding, Y. Lu, G. Chen, M. Jiang, *Angew. Chem., Int. Ed.* **2020**, *59*, 2.

[101] P. Mu, G. Zhou, C.-L. Chen, *Nano-Structures & Nano-Objects* **2018**, *15*, 153.

[102] C.-L. Chen, R. N. Zuckermann, J. J. DeYoreo, *ACS Nano* **2016**, *10*, 5314.

[103] X. Ma, S. Zhang, F. Jiao, C. J. Newcomb, Y. Zhang, A. Prakash, Z. Liao, M. D. Baer, C. J. Mundy, J. Pfaendtner, A. Noy, C.-L. Chen, J. J. De Yoreo, *Nat. Mater.* **2017**, *16*, 767.

[104] F. Jiao, X. Wu, T. Jian, S. Zhang, H. Jin, P. He, C. Chen, J. J. De Yoreo, *Angew. Chem., Int. Ed.* **2019**, *58*, 12223.

[105] H. Jin, Y.-H. Ding, M. Wang, Y. Song, Z. Liao, C. J. Newcomb, X. Wu, X.-Q. Tang, Z. Li, Y. Lin, F. Yan, T. Jian, P. Mu, C.-L. Chen, *Nat. Commun.* **2018**, *9*, 270.

[106] H. Jin, F. Jiao, M. D. Daily, Y. Chen, F. Yan, Y.-H. Ding, X. Zhang, E. J. Robertson, M. D. Baer, C.-L. Chen, *Nat. Commun.* **2016**, *7*, 12252.

[107] F. Jiao, Y. Chen, H. Jin, P. He, C.-L. Chen, J. J. De Yoreo, *Adv. Funct. Mater.* **2016**, *26*, 8960.

[108] H. Jin, T. Jian, Y. Ding, Y. Chen, P. Mu, L. Wang, C. Chen, *Biopolymers* **2019**, *110*, e23258.

[109] J. Sun, R. N. Zuckermann, *ACS Nano* **2013**, *7*, 4715.

[110] A. M. Sweetman, S. P. Jarvis, H. Sang, I. Lekkas, P. Rahe, Y. Wang, J. Wang, N. R. Champness, L. Kantorovich, P. Moriarty, *Nat. Commun.* **2014**, *5*, 3931.

[111] J. Kim, T. H. Han, Y.-I. Kim, J. S. Park, J. Choi, D. G. Churchill, S. O. Kim, H. Ihee, *Adv. Mater.* **2010**, *22*, 583.

[112] L. Ziserman, H.-Y. Lee, S. R. Raghavan, A. Mor, D. Danino, *J. Am. Chem. Soc.* **2011**, *133*, 2511.

[113] P. Li, X. Chen, W. Yang, *Langmuir* **2013**, *29*, 8629.

[114] Y. M. Lee, B. Jung, Y. H. Kim, A. R. Park, S. Han, W.-S. Choe, P. J. Yoo, *Adv. Mater.* **2014**, *26*, 3899.

[115] T. Xue, X. Cui, W. Guan, Q. Wang, C. Liu, H. Wang, K. Qi, D. J. Singh, W. Zheng, *Biosens. Bioelectron.* **2014**, *58*, 374.

[116] H. Shen, J. A. Fallas, E. Lynch, W. Sheffler, B. Parry, N. Jannetty, J. Decarreau, M. Wagenbach, J. J. Vicente, J. Chen, L. Wang, Q. Dowling, G. Oberdorfer, L. Stewart, L. Wordeman, J. J. De Yoreo, C. Jacobs-Wagner, J. Kollman, D. Baker, *Science* **2018**, *362*, 705.

[117] H. Pyles, S. Zhang, J. J. De Yoreo, D. Baker, *Nature* **2019**, *571*, 251.

[118] B. Kundu, M. Eltohamy, V. K. Yadavalli, S. C. Kundu, H.-W. Kim, *ACS Appl. Mater. Interfaces* **2016**, *8*, 28458.

[119] L. Miao, Q. Fan, L. Zhao, Q. Qiao, X. Zhang, C. Hou, J. Xu, Q. Luo, J. Liu, *Chem. Commun.* **2016**, *52*, 4092.

[120] F. Sun, L. Chen, X. Ding, L. Xu, X. Zhou, P. Wei, J. F. Liang, S.-Z. Luo, *J. Phys. Chem. B* **2017**, *121*, 7421.

[121] L. Miao, J. Han, H. Zhang, L. Zhao, C. Si, X. Zhang, C. Hou, Q. Luo, J. Xu, J. Liu, *ACS Nano* **2014**, *8*, 3743.

[122] H. Sun, L. Miao, J. Li, S. Fu, G. An, C. Si, Z. Dong, Q. Luo, S. Yu, J. Xu, J. Liu, *ACS Nano* **2015**, *9*, 5461.

[123] D. Chandler, *Nature* **2005**, *437*, 640.

[124] J. N. Israelachvili, *Intermolecular and Surface Forces*, Academic Press, Burlington, MA, **2011**.

[125] D. Ben-Amotz, *Annu. Rev. Phys. Chem.* **2016**, *67*, 617.

[126] B. J. Berne, J. D. Weeks, R. Zhou, *Annu. Rev. Phys. Chem.* **2009**, *60*, 85.

[127] S. Tsonchev, K. L. Niece, G. C. Schatz, M. A. Ratner, S. I. Stupp, *J. Phys. Chem. B* **2008**, *112*, 441.

[128] L.-H. Liu, Z.-Y. Li, L. Rong, S.-Y. Qin, Q. Lei, H. Cheng, X. Zhou, R.-X. Zhuo, X.-Z. Zhang, *ACS Macro Lett.* **2014**, *3*, 467.

[129] K. McGuinness, V. Nanda, *Org. Biomol. Chem.* **2017**, *15*, 5893.

[130] Y. Lin, M. R. Thomas, A. Gelmi, V. Leonardo, E. T. Pashuck, S. A. Maynard, Y. Wang, M. M. Stevens, *J. Am. Chem. Soc.* **2017**, *139*, 13592.

[131] E. V. Anslyn, D. A. Dougherty, *Modern Physical Organic Chemistry*, University Science, Sausalito, CA, **2006**.

[132] K. Tao, P. Makam, R. Aizen, E. Gazit, *Science* **2017**, *358*, eaam9756.

[133] E. Gazit, *FASEB J.* **2002**, *16*, 77.

[134] Z. Yu, A. Erbas, F. Tantakitti, L. C. Palmer, J. A. Jackman, M. Olvera de la Cruz, N.-J. Cho, S. I. Stupp, *J. Am. Chem. Soc.* **2017**, *139*, 7823.

[135] H. Zhang, S. Lou, Z. Yu, *Langmuir* **2019**, *35*, 4710.

[136] Y. Cote, I. W. Fu, E. T. Dobson, J. E. Goldberger, H. D. Nguyen, J. K. Shen, *J. Phys. Chem. C* **2014**, *118*, 16272.

[137] P. Jana, M. Ehlers, E. Zellermann, K. Samanta, C. Schmuck, *Angew. Chem., Int. Ed.* **2016**, *55*, 15287.

[138] M.-C. Hsieh, C. Liang, A. K. Mehta, D. G. Lynn, M. A. Grover, *J. Am. Chem. Soc.* **2017**, *139*, 17007.

[139] A. Ghosh, M. Haverick, K. Stump, X. Yang, M. F. Tweedle, J. E. Goldberger, *J. Am. Chem. Soc.* **2012**, *134*, 3647.

[140] Y. Chen, H. X. Gan, Y. W. Tong, *Macromolecules* **2015**, *48*, 2647.

[141] S. E. Boyken, M. A. Benhaim, F. Busch, M. Jia, M. J. Bick, H. Choi, J. C. Klima, Z. Chen, C. Walkey, A. Mileant, A. Sahasrabuddhe, K. Y. Wei, E. A. Hodge, S. Byron, A. Quijano-Rubio, B. Sankaran, N. P. King, J. Lippincott-Schwartz, V. H. Wysocki, K. K. Lee, D. Baker, *Science* **2019**, *364*, 658.

[142] I. W. Hamley, A. Dehsorkhi, V. Castelletto, S. Furzeland, D. Atkins, J. Seitsonen, J. Ruokolainen, *Soft Matter* **2013**, *9*, 9290.

[143] T. D. Jorgenson, M. Milligan, M. Sarikaya, R. M. Overney, *Soft Matter* **2019**, *15*, 7360.

[144] T. D. Jorgenson, D. T. Yucesoy, M. Sarikaya, R. M. Overney, *Langmuir* **2020**, *36*, 318.

[145] R. M. Putri, J. J. L. M. Cornelissen, M. S. T. Koay, *ChemPhysChem* **2015**, *16*, 911.

[146] S. A. Semerdzhiev, D. R. Dekker, V. Subramaniam, M. M. A. E. Claessens, *ACS Nano* **2014**, *8*, 5543.

[147] L. Liu, Y. Li, Y. Wang, J. Zheng, C. Mao, *ChemBioChem* **2017**, *18*, 2404.

[148] R. F. Garmann, M. Comas-Garcia, A. Gopal, C. M. Knobler, W. M. Gelbart, *J. Mol. Biol.* **2014**, *426*, 1050.

[149] W. W. Leow, W. Hwang, *Langmuir* **2011**, *27*, 10907.

[150] T. Kowalewski, D. M. Holtzman, *Proc. Natl. Acad. Sci. U.S.A.* **1999**, *96*, 3688.

[151] C. Chen, J. Hu, S. Zhang, P. Zhou, X. Zhao, H. Xu, X. Zhao, M. Yaseen, J. R. Lu, *Biomaterials* **2012**, *33*, 592.

[152] J. Li, Z. Chen, M. Zhou, J. Jing, W. Li, Y. Wang, L. Wu, L. Wang, Y. Wang, M. Lee, *Angew. Chem., Int. Ed.* **2016**, *55*, 2592.

[153] L. Schnaider, S. Brahmachari, N. W. Schmidt, B. Mensa, S. Shaham-Niv, D. Bychenko, L. Adler-Abramovich, L. J. W. Shimon, S. Kolusheva, W. F. DeGrado, E. Gazit, *Nat. Commun.* **2017**, *8*, 1365.

[154] N. Habibi, N. Kamaly, A. Memic, H. Shafiee, *Nano Today* **2016**, *11*, 41.

[155] H. He, J. Wang, H. Wang, N. Zhou, D. Yang, D. R. Green, B. Xu, *J. Am. Chem. Soc.* **2018**, *140*, 1215.

[156] M. Cao, S. Lu, N. Wang, H. Xu, H. Cox, R. Li, T. Waigh, Y. Han, Y. Wang, J. R. Lu, *ACS Appl. Mater. Interfaces* **2019**, *11*, 16357.

[157] T. R. Page, Y. Hayamizu, C. R. So, M. Sarikaya, *Biosens. Bioelectron.* **2012**, *33*, 304.

[158] A. H. Castro Neto, F. Guinea, N. M. R. Peres, K. S. Novoselov, A. K. Geim, *Rev. Mod. Phys.* **2009**, *81*, 109.

[159] D. Khatayevich, T. Page, C. Gresswell, Y. Hayamizu, W. Grady, M. Sarikaya, *Small* **2014**, *10*, 1505.

[160] C. Lin, E. Katilius, Y. Liu, J. Zhang, H. Yan, *Angew. Chem., Int. Ed.* **2006**, *45*, 5296.

[161] M. Charrier, D. Li, V. R. Mann, L. Yun, S. Jani, B. Rad, B. E. Cohen, P. D. Ashby, K. R. Ryan, C. M. Ajo-Franklin, *ACS Synth. Biol.* **2019**, *8*, 181.

[162] J. V. Barth, G. Costantini, K. Kern, *Nature* **2005**, *437*, 671.

[163] J. A. A. W. Elemans, S. Lei, S. De Feyter, *Angew. Chem., Int. Ed.* **2009**, *48*, 7298.

[164] J. C. Love, L. A. Estroff, J. K. Kriebel, R. G. Nuzzo, G. M. Whitesides, *Chem. Rev.* **2005**, *105*, 1103.

[165] F. Rosei, *Science* **2002**, *296*, 328.

[166] J. A. Theobald, N. S. Oxtoby, M. A. Phillips, N. R. Champness, P. H. Beton, *Nature* **2003**, *424*, 1029.

[167] X.-Y. Wang, A. Narita, K. Müllen, *Nat. Rev. Chem.* **2018**, *2*, 0100.

[168] S. Whitelam, I. Tamblyn, J. P. Garrahan, P. H. Beton, *Phys. Rev. Lett.* **2015**, *114*, 115702.

[169] M. Lingenfelder, G. Tomba, G. Costantini, L. Colombi Ciacchi, A. De Vita, K. Kern, *Angew. Chem., Int. Ed.* **2007**, *46*, 4492.

[170] A. K. Geim, I. V. Grigorieva, *Nature* **2013**, *499*, 419.

[171] J. J. De Yoreo, P. G. Vekilov, *Rev. Mineral. Geochem.* **2003**, *54*, 57.

[172] J. J. De Yoreo, P. U. P. A. Gilbert, N. A. J. M. Sommerdijk, R. L. Penn, S. Whitelam, D. Joester, H. Zhang, J. D. Rimer, A. Navrotsky, J. F. Banfield, A. F. Wallace, F. M. Michel, F. C. Meldrum, H. Colfen, P. M. Dove, *Science* **2015**, *349*, aaa6760.

[173] M. Sarikaya, C. Tamerler, A. K.-Y. Jen, K. Schulten, F. Baneyx, *Nat. Mater.* **2003**, *2*, 577.

[174] S. R. Whaley, D. S. English, E. L. Hu, P. F. Barbara, A. M. Belcher, *Nature* **2000**, *405*, 665.

[175] J. Chen, E. Zhu, J. Liu, S. Zhang, Z. Lin, X. Duan, H. Heinz, Y. Huang, J. J. De Yoreo, *Science* **2018**, *362*, 1135.

[176] C.-Y. Chiu, Y. Li, L. Ruan, X. Ye, C. B. Murray, Y. Huang, *Nat. Chem.* **2011**, *3*, 393.

[177] L. Gross, F. Mohn, N. Moll, G. Meyer, R. Ebel, W. M. Abdel-Mageed, M. Jaspars, *Nat. Chem.* **2010**, *2*, 821.

[178] H. Heinz, T.-J. Lin, R. Kishore Mishra, F. S. Emami, *Langmuir* **2013**, *29*, 1754.

[179] R. W. G. Wyckoff, *Crystal Structures*, Krieger, **1964**.

[180] H. Heinz, B. L. Farmer, R. B. Pandey, J. M. Slocik, S. S. Patnaik, R. Pachter, R. R. Naik, *J. Am. Chem. Soc.* **2009**, *131*, 9704.

[181] F. S. Emami, V. Puddu, R. J. Berry, V. Varshney, S. V. Patwardhan, C. C. Perry, H. Heinz, *Chem. Mater.* **2014**, *26*, 5725.

[182] H. Heinz, H. Ramezani-Dakhel, *Chem. Soc. Rev.* **2016**, *45*, 412.

[183] H. Ramezani-Dakhel, L. Ruan, Y. Huang, H. Heinz, *Adv. Funct. Mater.* **2015**, *25*, 1374.

[184] W. M. Haynes, *CRC Handbook of Chemistry and Physics*, CRC Press, **2014**.

[185] A. W. Webb, J. L. Feldman, E. F. Skelton, L. C. Towle, C. Y. Liu, I. L. Spain, *J. Phys. Chem. Solids* **1976**, *37*, 329.

[186] S. Bertolazzi, J. Brivio, A. Kis, *ACS nano* **2011**, *5*, 9703.

[187] A. Kozbial, X. Gong, H. Liu, L. Li, *Langmuir* **2015**, *31*, 8429.

[188] I. Gokce, R. W. Woody, G. Anderluh, J. H. Lakey, *J. Am. Chem. Soc.* **2005**, *127*, 9700.

[189] S. Auer, C. M. Dobson, M. Vendruscolo, *HFSP J.* **2007**, *1*, 137.

[190] M. Umetsu, M. Mizuta, K. Tsumoto, S. Ohara, S. Takami, H. Watanabe, I. Kumagai, T. Adschiri, *Adv. Mater.* **2005**, *17*, 2571.

[191] W.-J. Chung, K.-Y. Kwon, J. Song, S.-W. Lee, *Langmuir* **2011**, *27*, 7620.

[192] R. R. Naik, L. L. Brott, S. J. Clarson, M. O. Stone, *J. Nanosci. Nanotechnol.* **2002**, *2*, 95.

[193] M. Nalbach, P. Raiteri, S. Klassen, S. Schäfer, J. D. Gale, R. Bechstein, A. Kühnle, *J. Phys. Chem. C* **2017**, *121*, 24144.

[194] C. Fu, H. Lin, J. M. Macleod, A. Krayev, F. Rosei, D. F. Perepichka, *Chem. Mater.* **2016**, *28*, 951.

[195] L. Liu, Q. Li, S. Zhang, X. Wang, S. V. Hoffmann, J. Li, Z. Liu, F. Besenbacher, M. Dong, *Adv. Sci.* **2016**, *3*, 1500369.

[196] A. T. Haedler, S. C. J. Meskers, R. H. Zha, M. Kivala, H.-W. Schmidt, E. W. Meijer, *J. Am. Chem. Soc.* **2016**, *138*, 10539.

[197] J. D. Hartgerink, E. Beniash, S. I. Stupp, *Science* **2001**, *294*, 1684.

[198] H. K. Murnen, A. M. Rosales, J. N. Jaworski, R. A. Segalman, R. N. Zuckermann, *J. Am. Chem. Soc.* **2010**, *132*, 16112.

[199] L. E. R. O'Leary, J. A. Fallas, E. L. Bakota, M. K. Kang, J. D. Hartgerink, *Nat. Chem.* **2011**, *3*, 821.

[200] K. S. Novoselov, A. K. Geim, S. V. Morozov, D. Jiang, Y. Zhang, S. V. Dubonos, I. V. Grigorieva, A. A. Firsov, *Science* **2004**, *306*, 666.

[201] K. F. Mak, C. Lee, J. Hone, J. Shan, T. F. Heinz, *Phys. Rev. Lett.* **2010**, *105*, 136805.

[202] S. Mouri, Y. Miyauchi, K. Matsuda, *Nano Lett.* **2013**, *13*, 5944.

[203] J. Lee, P. Dak, Y. Lee, H. Park, W. Choi, M. A. Alam, S. Kim, *Sci. Rep.* **2015**, *4*, 7352.

[204] F. Perreault, A. F. De Faria, M. Elimelech, *Chem. Soc. Rev.* **2015**, *44*, 5861.

[205] S. Zhu, L. Gong, J. Xie, Z. Gu, Y. Zhao, *Small Methods* **2017**, *1*, 1700220.

[206] Y. Lu, B. R. Goldsmith, N. J. Kybert, A. C. Johnson, *Appl. Phys. Lett.* **2010**, *97*, 083107.

[207] T. R. Walsh, M. R. Knecht, *Chem. Rev.* **2017**, *117*, 12641.

[208] D. Li, W. Zhang, X. Yu, Z. Wang, Z. Su, G. Wei, *Nanoscale* **2016**, *8*, 19491.

[209] H. Yang, S.-Y. Fung, M. Pritzker, P. Chen, *PLoS ONE* **2007**, *2*, e1325.

[210] T. Seki, C. R. So, T. R. Page, D. Starkebaum, Y. Hayamizu, M. Sarikaya, *Langmuir* **2018**, *34*, 1819.

[211] L. Zhang, Y. Sheng, A. Zehtab Yazdi, K. Sarikhani, F. Wang, Y. Jiang, J. Liu, T. Zheng, W. Wang, P. Ouyang, P. Chen, *Nanoscale* **2019**, *11*, 2999.

[212] L. Sun, T. Narimatsu, S. Tsuchiya, T. Tanaka, P. Li, Y. Hayamizu, *RSC Adv.* **2016**, *6*, 96889.

[213] P. Li, K. Sakuma, S. Tsuchiya, L. Sun, Y. Hayamizu, *ACS Appl. Mater. Interfaces* **2019**, *11*, 20670.

APPENDIX A

PUBLICATIONS

[1] S. Zhang, **J. Chen**, J. Liu, H. Pyles, D. Baker, C. Chen, J. J. De Yoreo, *Adv. Mater*. **2020** (accepted).

[2] Z. Chen, M. C. Johnson, **J. Chen**, M. J. Bick, S. E. Boyken, B. Lin, J. J. De Yoreo, J. M. Kollman, D. Baker, F. DiMaio, *J. Am. Chem. Soc.* **2019**, *141*, 8891.

[3] **J. Chen**, E. Zhu, J. Liu, S. Zhang, Z. Lin, X. Duan, H. Heinz, Y. Huang, J. J. De Yoreo, *Science* **2018**, *362*, 1135.

[4] H. Shen, J. A. Fallas, E. Lynch, W. Sheffler, B. Parry, N. Jannetty, J. Decarreau, M. Wagenbach, J. J. Vicente, **J. Chen**, L. Wang, Q. Dowling, G. Oberdorfer, L. Stewart, L. Wordeman, J. J. De Yoreo, C. Jacobs-Wagner, J. Kollman, D. Baker, *Science* **2018**, *362*, 705.

[5] M. Hong, T. Moreland, **J. Chen**, H. H. Teng, R. Thalmann, J. J. De Yoreo, *Cryst. Growth Des.* **2015**, *15*, 129.

[6] B. Wang, G. Wang, B. Zhao, **J. Chen**, X. Zhang, R. Tang, *Chem. Sci.* **2014**, *5*, 3463.

VITA

Jiajun Chen is a Ph.D. candidate in the Department of Materials Science and Engineering at the University of Washington. He received his B.S. degree in Chemistry at Zhejiang University, China. He joined Dr. Jim De Yoreo's group in September 2014 and will join Dr. Paul Ashby's group at Lawrence Berkeley National Lab for Postdoc after graduation. His research interests mainly focus on understanding the self-assembly mechanisms of biomolecules using in situ atomic force microscopy.